UNIVERSITY OF COPENHAGEN

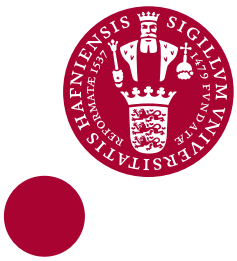

Modeling directional effects in land surface temperature derived from geostationary satellite data

Rasmussen, Mads Olander

Publication date:
2010

Document version
Early version, also known as pre-print

Citation for published version (APA):
Rasmussen, M. O. (2010). *Modeling directional effects in land surface temperature derived from geostationary satellite data*. Museum Tusculanum. http://curis.ku.dk/ws/files/32108104/Afhandling_MOR.pdf

Download date: 05. maj. 2023

DEPARTMENT OF GEOGRAPHY AND GEOLOGY
FACULTY OF SCIENCE
UNIVERSITY OF COPENHAGEN

THE PHD SCHOOL OF SCIENCE

PhD thesis

Mads Olander Rasmussen

Modeling directional effects in land surface temperature derived from from geostationary satellite data

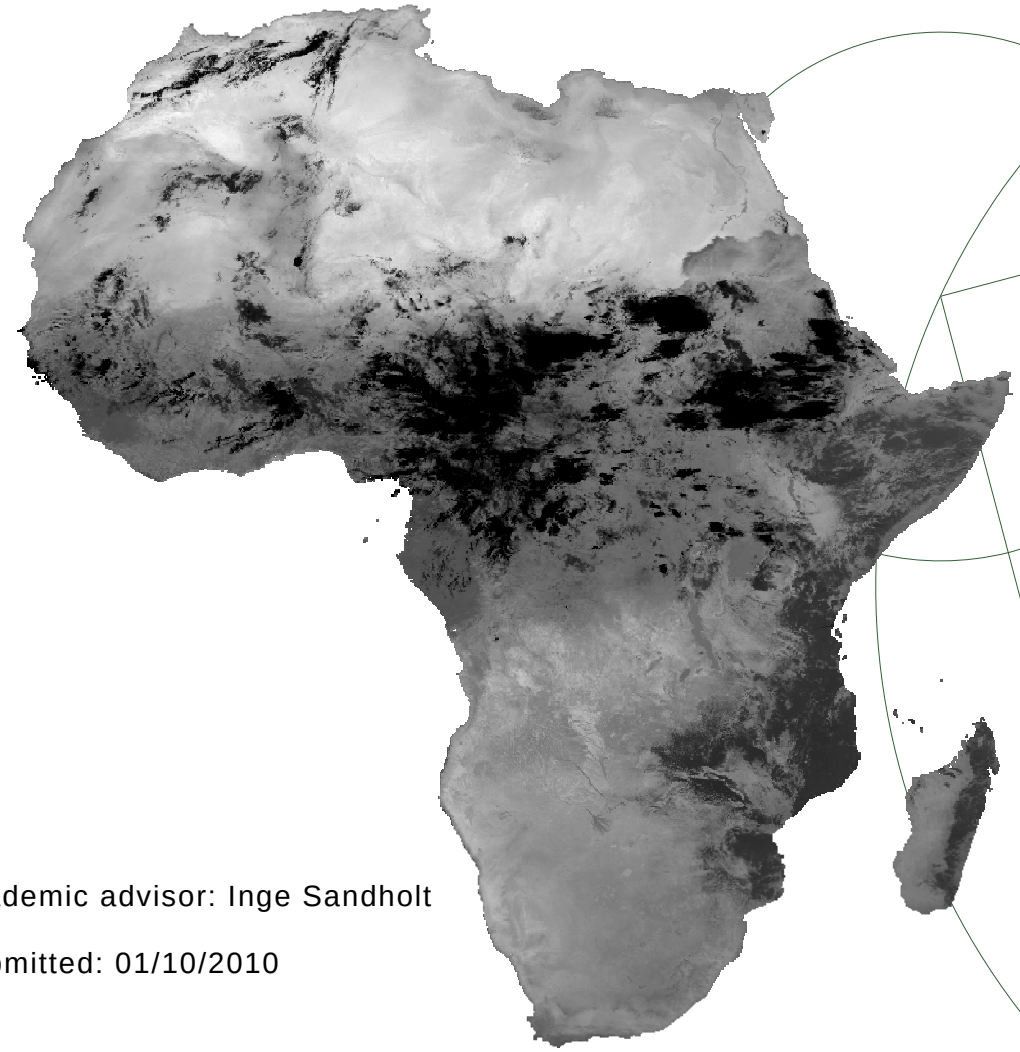

Academic advisor: Inge Sandholt

Submitted: 01/10/2010

Abstract

This PhD-thesis investigates the directional effects in land surface temperature (LST) estimates from the SEVIRI sensor onboard the Meteosat Second Generation (MSG) satellites. The directional effects are caused by the land surface structure (i.e. tree size and shape) interacting with the changing sun-target-sensor geometry. The directional effects occur because the different surface components, e.g. tree canopies and bare soil surfaces, will in many cases have significantly different temperatures. Depending on the viewing angle, different fractions of each of the components will be viewed by the sensor. This is further complicated by temperature differences between the sunlit and shaded parts of each of the components, controlled by the exposure of the components to direct sunlight. As the SEVIRI sensor is onboard a geostationary platform, the viewing geometry is fixed (for each pixel), while the illumination geometry changes both over the course of the day and with the seasons.

In the present study, the directional effects are assessed at different scales using a modeling approach. The model applied, the Modified Geometry Projection (MGP) model, represents the surface as a composite of four components; shaded and sunlit canopy and background, respectively. Given data on vegetation structure and density, the model estimates the fractions of the four components as well as the directional composite temperature in the view of a sensor, given the illumination and viewing geometry.

The modeling results show that the magnitude of the directional effects mainly depends on the tree cover, with moderate tree covers (20-40 %) causing the largest directional effects but with significant effects also at much sparser tree cover. The magnitude is also highly dependent on the temperature difference between the surface components, which is often largest in semi-arid areas that have relatively cool tree canopies and relatively hot soil/grass background. The largest amplitude in the directional effects occurs at "hot spot" geometry, which for geostationary sensors is at the equinoxes. Furthermore, the directional effects have varying magnitude and sign on both diurnal and seasonal scales, which will have implications if using LST products in downstream applications like hydrological or soil vegetation atmosphere transfer (SVAT) models. The directional effects will cause uncertainties in LST

estimates that are different in terms of timing than the uncertainties in data from polar orbiting sensors, which will cause discrepancies between measurements from the two types of sensors.

An assessment of the performance of current LST algorithms from MSG SEVIRI for semi-arid West Africa was carried out, using data from two field sites in Senegal and Mali. The agreement between the satellite and ground data for the rainy season was generally discouraging with biases exceeding 5 K, while there were indications that performance is much better during the dry season. The large discrepancies are thought to be caused by insufficient correction for the influence of the very moist atmosphere. For the period studied, the uncertainties found in the current LST products are likely to make it infeasible to identify the directional effects in the satellite data, as the uncertainties will mask the directional effects.

Resumé

Denne Ph.D.-afhandling omhandler vinkelafhængigheder i estimering af jordoverfladens temperatur fra SEVIRI-sensoren ombord på Meteosat Second Generation (MSG) satellitterne. Vinkelafhængighederne opstår som en konsekvens af en kombination af vegetationens struktur (træstørrelse og form), vinklen mellem overfladen og solen samt sensorens observationsvinkel. Desuden afhænger de af, om der er forskel i temperatur imellem de forskellige jordoverfladekomponenter, f.eks. trækroner og en græsflade. Afhængig af fra hvilken vinkel man observerer jordoverfladen, vil man se forskellige andele af hver af overfladekomponenterne. Dette bliver yderligere kompliceret af at der som regel er forskel på komponenternes temperatur, afhængig af hvorvidt de er eksponeret i forhold til solen. Da MSG-satellitterne er placeret i geostationær bane, vil observationsvinklen for SEVIRI-sensoren for hver pixel i billedet være konstant, hvorimod solvinklen vil ændre sig både i løbet af dagen og efter sæsonerne.

Denne afhandling kvantificerer vinkelafhængighederne via modellering på forskellige rumlige skala. Den anvendte model, "Modified Geometric Projection" (MGP) modellen, estimerer hvor stor del af en pixel dækket af hver af fire overflade komponenter, ud fra information om overfladens sammensætning samt solens og sensorens position. Modellen skelner imellem vegetationskroner (træer og store buske) og "baggrund" (en jordoverflade der kan være dækket af græs). Hver af disse komponenter kan enten være i skyggen eller eksponeret mod solen.

Modelleringsresultaterne viser at vinkelafhængighederne er størst i områder med moderat trædække (20-40%), men at disse også kan være betydelige i områder med sparsomt vegetationsdække. Vinkelafhængighedernes størrelse afhænger også i høj grad af temperaturforskellen mellem de enkelte komponenter, hvilke i mange tilfælde kan være store i semi-aride områder. Trækroner er relativt kølige på grund af fordampning, hvorimod jordoverfladen kan blive meget varm især hvis der ikke er nogen vegetation. Tidsligt opstår de største vinkelafhængigheder i tilfælde, hvor geometrien er tæt på det såkaldte "hot spot". "Hot spot" refererer til situationen hvor sensoren er placeret direkte imellem solen og jorden. Dette vil for geostationære satellitter ske omkring jævndøgn hvor solens bane følger ækvator. Denne "hot spot" i kombination med temperaturforskellene mellem komponenterne, gør at vinkelafhængighederne vil

variere både i løbet af døgnet og i løbet af året. Disse tidslige variationer kan have stor betydning for anvendelser af overfladetemperaturdata, f.eks. som input til hydrologiske og "soil-vegetation-atmosphere transfer" modeller, der udnytter SEVIRI's høje tidslige opløsning (der giver mulighed for estimering af overfladetemperaturen hvert kvarter, døgnet rundt). Vinkelafhængigheder i data fra geostationære satellitter vil desuden være forskellige fra vinkelafhængighederne i data fra polar-orbiterende sensorer, hvilket komplicerer sammenligning af data fra de to typer satellitter.

Afhandlingen omfatter også et studie af kvaliteten af eksisterende metoder til estimering af landoverfladens temperatur over et område i Vestafrika, ved hjælp af data fra to målestationer i Senegal og Mali. Overensstemmelsen imellem satellitdata og feltobservationer var generelt dårlig, med systematiske forskelle på mere end 5 K i løbet af regntiden, mens forskellene generelt var noget mindre i tørtiden. Årsagen til de store forskelle formodes at være problemer med korrektionen for atmosfærens relativt høje indhold af blandt andet vanddamp i regntiden. De store temperaturforskelle mellem satellit-baserede estimater af overfladetemperaturer og feltmålingerne umuliggør en direkte identifikation af vinkelafhængighederne i satellitdataene.

Preface

The work presented in this thesis is the result of my collaboration with many other researchers throughout the last four years. I have been fortunate to be able to work with a long list of inspiring and talented people both at the Department of Geography and Geology, University of Copenhagen and internationally. First and foremost I want to thank my supervisor Inge Sandholt for her long time support, the scientific guidance and for sharing numerous cups of coffee and thoughts. I am also grateful to Simon R. Proud, Simon Stisen, Anette Nørgaard, Rasmus Fensholt, Hector Nieto, Marc Ridler and Silvia Huber for the scientific collaboration and for making it enjoyable to come to work. I would also like to thank my other PhD-colleagues at the department, the research group members and other members of staff that I have worked with along the way.

During my PhD, I spent five months as a Visiting Researcher at the NOAA National Climatic Data Center in Asheville, North Carolina. I am indebted to Ana Pinheiro and Jeff Privette for hosting my stay and for the warm welcome. Without your help and inspiration the work enclosed within this thesis would not have been possible. John Bates, Thomas C. Peterson and NOAA NCDC are also thanked for their support and hospitality.

I am also deeply grateful for the collaboration I have had with Frank Göttsche, Folke Olesen and colleagues from the Karlsruhe Institute of Technology. They have contributed with invaluable knowledge, experience and support - both in the field and during the writing process. Without your help and guidance, I would undoubtedly still be working on this thesis.

I have also received invaluable help from Cheikh Mbow, Doudou Diop and colleagues at Universite Cheikh Anta Diop, Senegal, during my field trips Dahra. I have also benefited greatly from the support from the FIVA PhD-school and the AMMA project, both in terms funding, knowledge and access to data. I would like to thank Eric Mougin and Franck Timouk for sharing their field data from their site in Mali.

Last, I would like to thank my family and friends for their indulgence and never ending willingness to help. Finally, I would like to dedicate this thesis to my mother, whom we lost too early.

Contents

Contents vii

1 Introduction and research objectives 1

2 TIR remote sensing of structured canopies from geostationary orbit 5
- 2.1 Introduction . . . 5
- 2.2 Directional effects . . . 7
- 2.3 The potential of the MSG SEVIRI sensor . . . 9
- 2.4 Introduction to the MGP model . . . 11

3 Introduction to thesis papers 15
- 3.1 Paper I . . . 17
- 3.2 Paper II . . . 17
- 3.3 Paper III . . . 18
- 3.4 Paper IV . . . 18

4 Conclusion and perspectives on future research 19
- 4.1 Conclusions . . . 19
- 4.2 Perspectives on how to operationally correct for directional effects 22

Bibliography 25

Paper I 29

Paper II 43

Paper III 57

Paper IV 73

Chapter 1

Introduction and research objectives

Surface temperature is a key diagnostic parameter of land surface conditions. It is used in many modeling applications including hydrological models, soil vegetation atmosphere transfer (SVAT) models as well as regional and global climate models. Furthermore, it can be used in conjunction with other information for the estimation of soil moisture, evapotranspiration and detection of crop stress at a wide range of scales.

Remote sensing provides a unique method for retrieving spatially distributed estimates of surface temperature over large areas almost instantaneously. This has been possible from satellite borne instruments since the late seventies at different scales. In general, a choice has to be made between high spatial resolution and high temporal resolution. High resolution thermal data (60 meter from LANDSAT-7 and 90 meter from ASTER) is available, but only with a minimum time between observations of 16 days. Coarser data with a spatial resolution of approximately 1 kilometer is available twice a day (from the MODIS and AVHRR instruments) for most locations on Earth, while the geostationary meteorological satellites provide even coarser data with a spatial resolution of 3-4 kilometers every 15 or 30 minutes.

The Meteosat Second Generation (MSG) series of satellites that has been operational since January 2004 carry an improved series of sensors compared to the first generation Meteosat sensors, that provide new opportunities for the estimation of surface temperature from geostationary satellites. The Spinning Enhanced Visible and Infrared Imager (SEVIRI) instrument onboard the MSG-satellites provides data in 11 spectral bands at a spatial resolution of 3 kilometers every 15 minutes (the actual resolution of the sensor is 4.8 km, but the data is sampled into a 3 km grid). This, combined with the presence of two thermal infrared bands located within at-

mospheric windows (typically referred to as split-window bands), is unprecedented for geostationary sensors covering Europe and Africa. Although designed for meteorological purposes, the presence of split-window bands allows for relatively easy and precise estimation of land surface temperature on a continental scale every 15 minutes, a total 96 observations a day. Previously, split-window bands were only available from polar-orbiting moderate spatial resolution sensors with a limited number of daily overpasses (maximum 4 for MODIS Terra and Aqua combined, and a similar number from the NOAA AVHRR sensors). As the data availability for a given point on the ground is further limited by the presence of clouds, the increase in potential number daily observation from a maximum of 4 to 96, opens up new applications of temperature data. In particular it allows reconstruction of the diurnal variation in surface temperatures, which is important for many modeling applications.

All satellite products contain errors stemming from a wide range of sources including sensors noise, calibration inaccuracies, atmospheric attenuation and scattering of thermal radiation by the atmospheric constituents, errors in the applied algorithms for converting the measurements into values of physical parameters and in the ancillary data required for these. Some of these errors are constant in time or vary only slowly, while others vary from image to image, due to the diurnal variation in radiation input. When applying a satellite derived product in models, the errors in the product will propagate through to the model results, limiting the accuracy and applicability of the model results. Therefore it is important to investigate, document and, if possible, reduce the different sources of errors in the satellite products.

This thesis investigate one of the sources or error in land surface temperature products from the MSG SEVIRI instrument, namely the errors introduced by the vegetation structure and properties in combination with the illumination and viewing geometry. This is not necessarily the largest source of error present, but only limited research has previously been carried on the subject. The spatial focus is on Africa, with emphasis on the semi-arid West Africa region where savanna landscapes dominate. This is a data-sparse region where other sources of data is hard to come by, and is at the same time the land area where MSG SEVIRI has the most advantageous conditions in terms of viewing geometry.

The specific research objectives are:

- To investigate the influence of vegetation density and structure and illumination/viewing geometry on the land surface temperature estimated from the MSG SEVIRI sensors.

- To quantify these "directional effects", in order to assess under what circumstances they constitute a significant problem for the use of LST-data derived from geostationary satellite sensors.

This is investigated mainly through modeling of the directional effects using a model developed specifically for this purpose. Attempts are made to quantify the

effects on both the local scale, through comparison with *in situ* measurements at a savanna site, and on the continental scale.

Thermal infrared remote sensing of structured canopies from geostationary orbit

2.1 Introduction

Satellite measurements of surface temperature from geostationary orbit have been available since the seventies for Europe and North America, and later for the entire globe. Today, a large number of sensors onboard meteorological satellites provide at least hourly data on temperature for most of the globe (data coverage for the polar regions is limited as the geostationary orbit requires the satellites to be located over the Equator). The sensors have been developed mainly for meteorological purposes which generally means that the temporal resolution has been prioritized over the spatial resolution. This means that the normal pixel size vary between three kilometers (for the European Meteosat Second Generation satellites (Schmetz et al., 2002)), to 4, 5 and even 8 kilometers for the Indian Insat 3A system. On the other hand, most systems provide data every half hour with three spectral bands usually located in the visible, mid-infrared and thermal infrared to provide information on cloud cover, atmospheric water vapour content and temperature. Some of the sensors provide data in more spectral bands, and of special interest with regard to the estimation of land surface temperature (LST) is the availability of at least two thermal infrared bands in the 10 to 13 μm region allowing for the use of so-called split-window algorithms (Price, 1984). The split-window algorithms perform corrections for atmospheric effects based on the difference in absorption between adjacent thermal infrared bands. Estimation of LST from single band temperature measurements is also possible, but requires more detailed information on the vertical distribution of water vapour and temperature in the atmosphere. This data is hard to obtain for large areas, thus limiting the applicability of single thermal-band sensor for accurate LST estimation (Dash et al., 2002). Currently, the European MSG SEVIRI systems, the Chinese

Fengyun IVISSR and the Japanese MTSAT-2 systems all feature two bands suitable for LST estimation, while the current generation of the Indian Insat, the Eumetsat Indian Ocean Data Coverage mission and the American GOES-satellites do not. Of these satellites, the MSG SEVIRI provides both the highest spatial resolution of 3 kilometers and the highest temporal resolution with scans of the Earth disk every 15 minutes in a total of 11 spectral bands. This makes the MSG SEVIRI system the best current operational satellite for monitoring land surface temperature from geostationary orbit.

Despite the relatively good quality of LST estimates from split-window algorithms, as compared to the single band algorithms, errors are still present in the data. These can come from many different sources including: (1) sensor noise, (2) insufficient sensor calibration, (3) inaccuracies in the atmospheric correction, and (4) errors stemming from the input data on surface emissivity and atmospheric water vapor content required by split-window algorithms.

The Land Surface Analysis Satellite Applications Facility (LSA SAF) produces a freely available LST-product at full spatial and temporal resolution based on the MSG SEVIRI data (EUMETSAT et al., 2009). It is a traditional split-window algorithm, based on the method originally proposed by Becker and Li (1990) and later simplified for use with the polar-orbiting MODIS instruments by Wan and Dozier (1996). The coefficients of the algorithm were calculated based on radiative transfer model simulations using an extensive database of atmospheric temperature and water vapour profiles (EUMETSAT et al., 2009). Along with the estimates of LST, the product also contains two data layers containing information on the uncertainties for each pixel in the product (Freitas et al., 2010). These are computed through a scheme classifying the pixels into three levels of confidence depending on the expected uncertainty. This information for each pixel is passed to the user both as a layer containing flag values and as a layer containing a numerical value describing the uncertainty.

In addition, the geometric configuration of the illumination and viewing conditions and the structure surface cover also influences the LST-estimates. These "directional effects" stem both from the anisotropy of the individual surface components, and from a "composite" surface anisotropy caused by shading effects between the different components. These possible sources of error will be described in more detail below in section 2.2. The quality assessment (QA) layers of the LSA SAF LST-product consider most of the sources of error mentioned above, including errors stemming from uncertain estimates of emissivity and water vapor data, but they do not explicitly address "directional effects". This means that the uncertainty estimate given by the QA-layers is to be considered as a "best case"-scenario, as the effects of surface anisotropy are not included. Previous studies for the polar-orbiting NOAA AVHRR sensors showed directional effects of up to $\pm$ 5 K, with the largest effects occurring in areas with moderate tree cover (Pinheiro et al., 2004). To our knowledge, a similar assessment has, to date, not been made for geostationary sensors with the exception

of the study on the differences between LST from three GOES systems across the overlap region in the United States by Minnis and Khaiyer (2000)

This thesis attempts to bridge this gap in knowledge by investigating the magnitude, timing and location of the directional effects.

2.2 Directional effects

The geometric effects that are the subject of this thesis, are actually a combination of several individual effects of the interaction between incoming radiation (both shortwave and longwave), the atmosphere, the land surface and the viewing geometry of the sensor in question. In addition, some of the effects are due to the specific properties of the land surface components, while others arise as a consequence of the interaction between the different surface components and the radiation. The latter is particularly important when considering medium and coarse resolution satellite sensors, as these will inevitably mainly be measuring pixels containing a mix of different surface covers. This means that the signal measured by the sensor for a given pixel contains a signal from each of the surface components present within the pixel, which might also be affected by interaction between the signals from the different components.

If considering the directional effects on the scale of the individual surface components, e.g. a soil surface or a vegetation canopy, the main source of directional effects is the anisotropy of the emissivity. The emissivity of most materials vary with the view zenith angle, with the highest emissivities occurring at nadir and decreasing as the view zenith angle increases. This has been shown both through field measurements and through modelling (Cuenca and Sobrino, 2004; Labed and Stoll, 1991; Snyder et al., 1997; Sobrino and Cuenca, 1999; Sobrino et al., 2005). These effects are significant, and can reach more than 5% depending on the surface material at high view zenith angles. This will especially introduce errors in the LST-estimates in cases where the emissivity is not derived from measurements with the same geometry as the measurements used for the LST estimation. This could e.g. be when using laboratory estimates of emissivity (usually at nadir) of a given material, for LST-estimation using a sensor at off-nadir angles, which is most often the case. Furthermore, the emissivity of materials tends to vary slightly, but not uniformly, with wavelength (da Luz and Crowley, 2007; Labed and Stoll, 1991; Snyder et al., 1997). This means that the directional effect can differ depending on the wavelength.

The other type of directional effects occur due to the structure and location of the surface components in relation to each other and the specific illumination and viewing geometry. An example of this is shown in figure 2.1 for a case with a landscape consisting of patches with forest and patches with bare soil in between. Depending on the view angle (nadir or off-nadir), the fractions of the soil and forest components of the surface as seen by the sensors vary considerably. For the nadir case, the

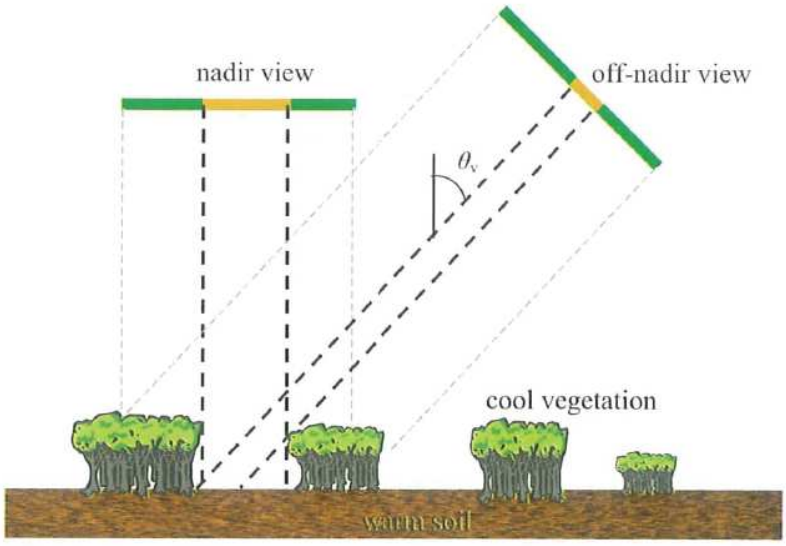

Figure 2.1: A schematic example of the difference between nadir and off-nadir view for areas with mixed land cover. Source: Jia (2004); Menenti et al. (2008)

signal from the soil fraction that reaches the sensor is about a third of the total, while the off-nadir sensor almost exclusively measures the signal from the forest. The forest and the soil surface will in many cases have different temperatures, which will lead to differences in the measured temperatures solely caused by the difference in the viewing angle. The difference in temperature between the two surface covers depends on the specific properties of the cover and on the availability of water for transpiration (for the vegetation) or evaporation. The abundance of water will generally limit the temperature differences. Furthermore, the temperature measured by a satellite sensor will also depend on whether the sunlit part or the shaded parts of the components are in view of the sensor, as the sunlit parts will in many cases be warmer than the shaded part. This is especially true for soil surfaces that might get very warm if no water is available, while vegetation show less differences in temperature between the sunlit and shaded parts. Cases where the sun and the sensor are aligned will therefore appear warmer than cases where the illumination and viewing angles are very different, everything else being equal.

Many modeling studies have been performed to investigate either the angular dependency of the emissivity, the effects of the canopy geometry or the combined effects (Coret et al., 2004; Jia, 2004; Jia et al., 2002; Li et al., 1999; Pinheiro et al., 2006, 2004; Pinheiro, 2003; Smith et al., 1997; Sobrino et al., 2005; Yan et al., 2001; Yu et al., 2006). Many of them simulate the directional effects for specific (polar orbiting) sensors and for one or more specific land covers, but none of them treat the case of a geostationary sensor explicitly. These effects have also been measured both in the laboratory and in the field (Caselles et al., 1992; Cuenca and Sobrino,

2004; Kimes et al., 1980; Kimes, 1981; Lagouarde et al., 1995; Snyder et al., 1997; Sobrino and Cuenca, 1999) and identified in analysis of satellite data (Minnis and Khaiyer, 2000; Trigo et al., 2008). Some of the most severe effects were found by Lagouarde et al. (1995) which found differences between nadir view and other view angles ranging between -4 K and +3.5 K, and argued that these effects should be larger from satellite sensors that generally have narrower field of views compared to instruments used for *in situ* measurements.

2.3 The potential of the MSG SEVIRI sensor

The MSG SEVIRI sensor provide novel opportunities for monitoring diurnal changes in the land surface temperature through the combination of 15 minute temporal resolution and the presence of two appropriate thermal channels as described above. However, along with these new opportunities comes additional potential sources of error that are not well understood for the case of geostationary satellites. As the above section shows, some work has been done on the directional effects, but these mainly treat the case of *in situ* measurements or data from polar-orbiting satellites sensors. These are usually positioned in sun-synchronous orbits, meaning that they always follow the sun, resulting in overpass times over the equator at approximately the same (local sun-) time at each overpass. This means that the illumination geometry will be more or less the same for each overpass, while the viewing geometry for a specific place on the ground will change according to the exact orbit (in a pattern which depending on the orbit, usually repeats within approximately two weeks). Although there will still be seasonal changes in the illumination geometry, the almost constant local overpass times will limit the difference between the directional effects between two subsequent overpasses.
The case is different for geostationary satellites with high temporal resolution, as the illumination geometry will change from one image to the next throughout the day as the suns footprint moves west. The viewing geometry on the other hand is fixed, which will limit the directional effects in the LST estimation between two subsequent estimates, but still might influence the absolute values. The magnitude of the directional effects can also be expected to change, as the difference between the component temperatures changes as the sun heats up some components more than others. This should lead to a diurnal pattern in the temperature differences between the components and therefore also a diurnal pattern in the directional effects. Polar-orbiting sensors do not have this problem, as the overpass time is more or less the same everyday, leaving only the seasonal changes (and the effects of changing viewing geometry).

A previous study (Pinheiro et al., 2004) indicates that the directional effects are largest at moderate tree cover. Considering the case shown in figure 2.1, this makes sense. If no or very few trees were present, the effects of monitoring the areas at

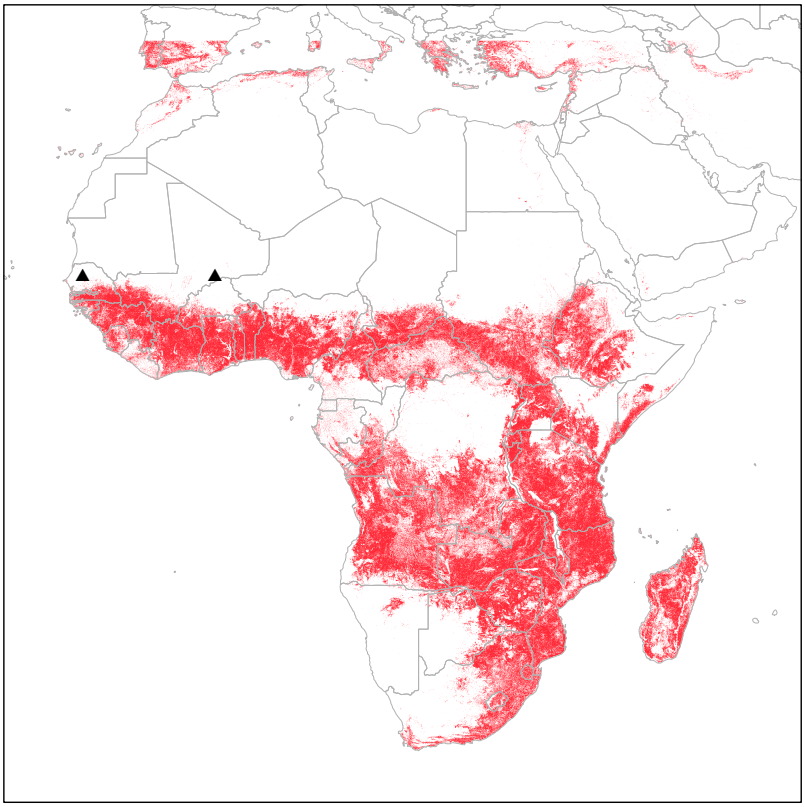

Figure 2.2: A map showing areas with between 10% and 40% tree cover according to the MODIS Vegetation Continuous Fields product (collection 3, continental version for the year 2001) (Hansen et al., 2003). The black triangles indicate the position of the two *in situ* sites used for comparison and validation.

an off-nadir angle would not change much as there are no (or almost no) trees to shadow for the soil surface. At the other end of the scale, very densely vegetated areas show small directional effects as all the energy will be emitted from a dense and more or less homogeneous layer of the canopy. Furthermore, densely vegetated areas will show little difference in component temperatures and uniform emissivity values, effectively limiting the directional effects.

This leaves areas with moderate tree cover, which are expected to show the most severe directional effects. Figure 2.2 show the areas in Africa and Southern Europe with between 10 and 40 % tree cover according to the MODIS vegetation continuous fields product (Hansen et al., 2003). Although areas with slightly more tree cover will also show significant directional effects, the areas with sparser cover are generally drier areas, and thus can be expected to have larger differences between the component temperatures. The areas shown in the figure cover large parts of sub-Saharan Africa including parts of the Sahel-Sudan zone and the semi-arid parts of Eastern and Southern Africa. In total, approximately 20 % of the land surface of

Africa falls within this range of tree cover.

The Sahel-Sudan region that will be the main geographical area of interest in this thesis, is dominated by savanna and agricultural landscapes. Parts of it falls within the areas highlighted in figure 2.2 while other parts have less tree cover. The vegetation within the region is limited by the precipitation, which is highly variable in both space and time. This makes the population vulnerable to drought which causes problems for both agriculture and transhumance. Monitoring of the land surface temperature and biophysical properties of the land surface from Earth Observation data provides important input data to early warning systems and climate models that can aid in the early discovery of droughts as well as evaluate the severity and spatial extent when they occur. This naturally requires timely and accurate data to drive the models, such as that provided by the SEVIRI sensor.

2.4 Introduction to the MGP model

One of the main tools for investigating the directional effects in this thesis is the Modified Geometric Projection (MGP) model developed by Ana Pinheiro and co-workers (Pinheiro et al., 2006, 2004; Pinheiro, 2003). It was developed especially for investigating the directional effects for the NOAA AVHRR sensors over the African continent. Below, a general introduction will be given to the underlying principles, to the different model approaches and to the MGP-model in particular. A full physical representation of the problem and the different modeling approaches is beyond the scope of this work.

Modeling of directional effects is a subject than has been explored extensively, but mainly in the visible domain. The surface anisotropy is often described in terms of the "bidirectional reflectance distribution function" (BRDF). The BRDF describes how much incoming light is reflected depending on illumination and viewing geometry and the surface properties. In the thermal domain, the reflectance is of less importance compared to the thermal emittance (disregarding reflected solar radiation present during daytime in the MSG channel centered around 3.9 μm), but the underlying principles are the same.

There are several possible approaches on how to model the directional emittance of a discontinuous canopies:

- Geometric models that consider the size and location of the individual trees or shrubs as well as the emissivity temperatures of each of the components. The vegetation canopies are treated as opaque solids, with no within-crown gaps. The composite temperature is assumed to be a linear combination of the emittance of each of the components weighted by their relative abundance according to the specific viewing geometry. Each of the components is assumed to be isotropic. This approach treats the canopy as one homogeneous layer, ignoring the difference in canopy density and structure at different levels in the

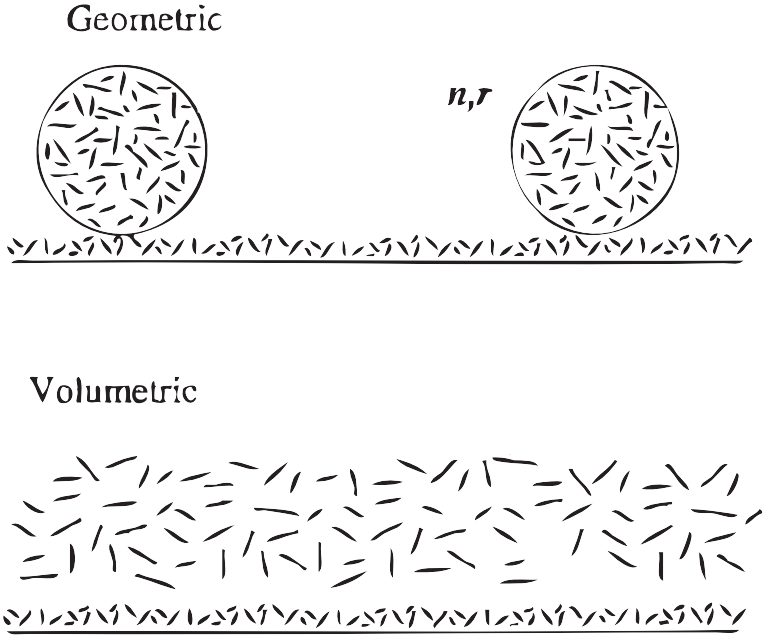

Figure 2.3: Edited after Snyder and Wan (1998)

canopy. These models are deterministic and some apply ray-tracing methods to model the interaction between the incoming radiation and the surface.

- Radiative Transfer (RT) models. These include a much more rigorous treatment of the interactions between the incoming radiation and leaves, branches and trunks at different layers in the canopy (volumetric representation). For this purpose, detailed information on vegetation structure such as crown density, leaf area index (LAI) and leaf angle distribution is required. This limits the applicability of these models to small scale studies as the required input data is hard to obtain on larger scale.

The approaches are exemplified in figure 2.3 which schematically shows how the surface is described in the two cases. In the geometric models, the crowns are described as opaque solids with a well defined shape (which is also depicted in figure 2.1), while the RT-models describe crowns as one or more layers of statistically distributed objects (leafs, branches and stems), also called a volumetric approach. The interaction between the incoming radiation and the canopy is treated through probabilities of the radiation being intercepted in a given layer. The ground is considered an opaque surface and controls the interaction with the land surface.

The approach applied in this thesis belongs to the geometric type of model, but accounts for some of the shortcomings of this type of model. It uses the geometric approach for describing the composition of the pixel, e.g. using spheroids

to represent trees. In the case of the Modified Geometric Projection (MGP)-model applied within this thesis (Pinheiro et al., 2006, 2004; Pinheiro, 2003), this is done using the Geometric Optics part of the Geometric Optic - Radiative Transfer model (Li and Strahler, 1992; Ni et al., 1999). This allows for estimating the fractional cover of four surface components within a given area. The four components used within the model are sunlit and shaded canopy, and sunlit and shaded background. The canopy components refer to tree and tall shrub canopies while the background consists of bare soil and low vegetation. For the canopy components, the within-crown gaps are accounted for by first estimating the gap probability (the probability of a beam passing through the canopy layer). Then the crown radius is adjusted, effectively removing the gaps from the canopy, so that the rest of the canopy can be described as one homogeneous layer of vegetation.

The above described MGP-model was chosen to provide the optimal trade off between simplicity, not requiring extensive information on vegetation properties and being relatively computationally efficient to allow large scale application, while taking the most important factors into account. Other models like the DART model (Gastellu-Etchegorry et al., 1996; Guillevic et al., 2003), a 3D radiative transfer model, provides a more realistic representation of the canopy, but require more detailed input data, and is much more computationally demanding, effectively making it impossible to apply on a continental scale.

Chapter 3

Introduction to thesis papers

The four papers constituting the main part of this thesis all contribute to answering the research questions stated in Chapter 1. Their contributions may be illustrated by placing them in a coordinate system with three axes, one representing the spatial scale, from plot to continental, one representing the level of detail in the description of the land surface, and one representing the spectrum from a purely empirical to a purely theoretical analysis.

As outlined in figure 3.1, Paper I is mainly theoretical in orientation, focusing on modelling of the directional effects. It addresses the continental scale, and is based on a relatively crude description of the land surface - and the tree cover specifically. Building on this, Paper II applies the model at the finer scale of the West African Sahelian-Sudanian savanna landscape, and validates the model outputs against field observation at micro-scale in Dahra, Senegal. Thus it is far more empirical in scope, and uses a more detailed parameterization of the tree cover. Paper III focuses on the key input data for the MGP model, the tree cover. As shown in Paper I and II, the size of the directional effects depends critically on tree cover, and may amount to as much as 3 K in cases with mid-range tree cover (20-40 % crown cover). Therefore, methods for estimating tree cover percentage and tree height at a scale relevant to the use of MSG SEVIRI data are required, and Paper III addresses this by presenting a method for local to meso-scale tree cover estimation in savanna and woodland environments on the basis of high resolution satellite images. The parameterization of the tree cover is, however, relatively simplistic. Finally, Paper IV seeks to place the directional effects in perspective by comparing the standard LST estimates from MSG SEVIRI, with estimates from MODIS, and from *in situ* measurements in Dahra as well as from the Agoufou site in Mali. Thus the fourth paper addresses the sub-continental scale, it is empirically based and does not involve any particular parameterization of the tree cover (and therefore it can not be placed on the second axis).

The continental modeling paper (Paper I) allows an assessment of the order of

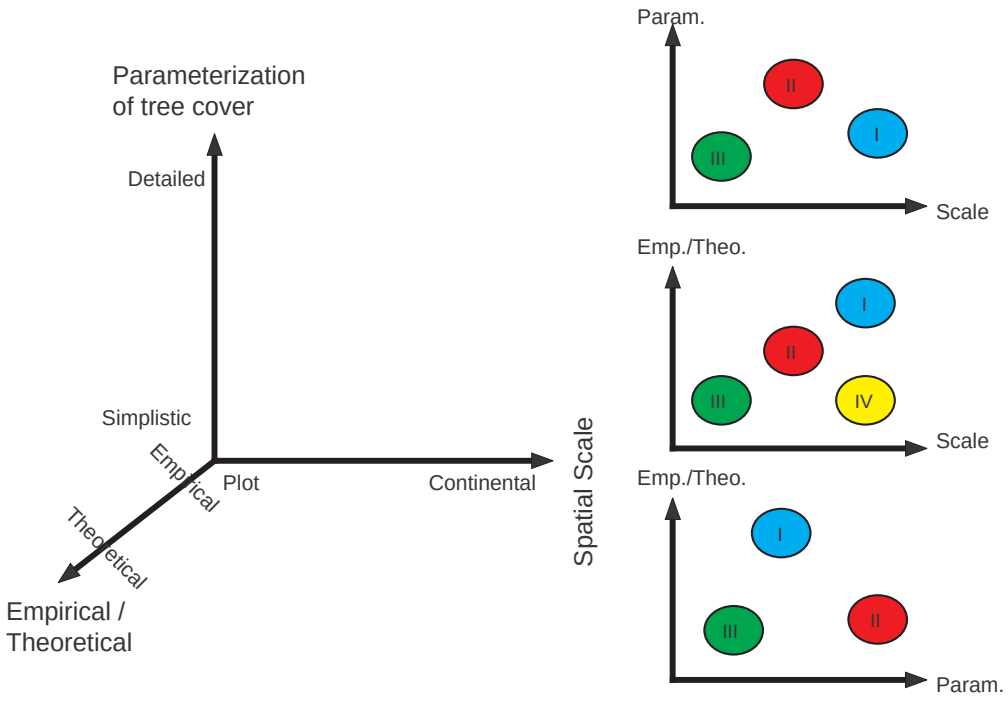

Figure 3.1: Illustration of the contribution of each of the four papers contained within this thesis on three axes. To the right, the position of each paper projected onto three 2D plots.

magnitude of the directional effects, and provides information on under which circumstances, in regards tree cover, time of day and year, and in what parts of Africa these effects may cause substantial errors in LST-estimates from MSG SEVIRI. Paper II applies the model to examine, for the savanna landscapes of the West African Sahel-Sudan zone, the likely errors in LST-estimation, which may be caused by directional effects. Since the MGP-model and its practical uses imply that information on tree cover (tree height, crown cover percentage, crown dimensions and density) is required, Paper III studies the possibilities of deriving this information from high spatial resolution satellite images. Finally, paper IV assesses the uncertainty associated with the LST-data presently available from SEVIRI, which do not take directional effects into account, by comparison to MODIS-based estimates and field measurements. This serves to show that directional effects are, under most circumstances, smaller than the uncertainties caused by other factors, yet in cases of medium-level crown cover, e.g. in savanna woodlands, and under specific illumination and observation geometries, bidirectional effects may dominate and need to be compensated for.

3.1 Paper I

Modeling Angular Dependences in Land Surface Temperatures From the SEVIRI Instrument Onboard the Geostationary Meteosat Second Generation Satellites

The paper investigates the directional effects on the continental scale using a modeling approach considering three cases that represent the annual angular variation. This is done using the MGP-model which requires the emissivities and temperatures of the four surface components to be known. As this is not possible on a continental scale, it was chosen to prescribe a fixed set of component emissivities and temperatures and to keep these constant over time. Although this is not representative of the real conditions, it reduces the number of parameters that can influence the results. Thus, it allows for an *all-other-factors-being-equal* estimation of the magnitude and timing of the directional effects on the continental scale.

The analysis is carried out for three days: spring equinox, summer solstice and fall equinox. The results show that the difference between the LST observed and that which would have been observed at nadir amounts to less than 1 K under most conditions, which is within the expected uncertainty of LST-products. The greatest differences observed are at tree cover percentages between 30 and 40 % and at "hot spot situations" where the sun is just behind the sensor. In the worst case, autumn equinox, 7 % of the pixels have differences greater than 1 K. The highest values amount to more than 3 K, yet such differences are rare. The difference varies significantly though the day, which might be critical in applications relying on an accurate representation of the diurnal cycle in LST-temperatures.

3.2 Paper II

Directional effects on land surface temperature estimation from Meteosat Second Generation for savanna landscapes

For a savanna site at Dahra in northern Senegal, directional effects in LST-estimates from MSG SEVIRI are modeled using the Modified Geometric Project (MGP) model. The required input data on scene component temperatures are derived from *in situ* measurements. While the "errors" caused by directional effects, the difference between observed LST and what would have been observed at nadir, are generally small, the main problem is associated with the diurnal cycle of LST: The amplitude of LST-variation might be significantly affected. In order to represent other parts of the Sahel-Sudan zone, the MGP model has been used to assess directional effects for crown cover percentages of 4 %, corresponding to the Dahra region, 8, 12, 18, 25 and 35 % and for four different tree cover structures. Maximum differences generally increase with crown cover up to 25 %. Further the paper compares the modeled

LST-values with the LST-estimates from the LSA-SAF LST product, and the results show that overall, the match between the modeled and measured LST is discouraging. Toward the end of the study period (and rainy season) the match is much better, reaching r^2 of more than 0.9.

3.3 Paper III

Tree survey and allometric models for Tiger Bush in Northern Senegal and comparison with tree parameters derived from high resolution satellite data

The paper describes and validates an Earth Observation-based method for estimating tree cover and woody biomass for a 10 by 10 km area close to Dahra in northern Senegal. The purpose is (1) to provide input to the work on modeling the directional effects in MSG SEVIRI, (2) to demonstrate the feasibility of estimating woody biomass (and with that also the carbon storage) by use of high resolution satellite images, and (3) to develop and test methods for upscaling results to the scales relevant in relation to MODIS and MSG, by relying on a correlation between NDVI (greenness) and tree cover. The results showed very good agreement between field observations of the tree cover, tree height and crown diameter, which provided the necessary inputs both to modeling directional effects in MSG SEVIRI-data and to estimating biomass. Attempts to upscale to larger areas/scales were unsuccessful, since the NDVI-signal from the tree crowns was masked by variations in background NDVI.

3.4 Paper IV

Intercomparison of LST products from MSG SEVIRI and comparison with MODIS data and in situ measurements in West Africa

This paper examines the accuracy of current available MSG SEVIRI and MODIS LST products by comparison with *in situ* observations in Dahra in northern Senegal and from Gouma, Mali. The contribution to the thesis lies in the information provided on the accuracy obtained in LST-products and possible alternative LST-algorithms without correction for directional effects. The results show significant inaccuracies in LST-estimates from all MSG SEVIRI derived products in the rainy season, while estimates are more reliable in the dry season. MODIS-estimates display greater uncertainties compared to the MSG-SEVIRI estimates. The implications of the study are that other problems in SEVIRI-based LST-estimates dominate in the rainy season, while directional effects may well play a significant role in the dry season.

Chapter 4

Conclusion and perspectives on future research

4.1 Conclusions

The directional effects in LST estimates from MSG SEVIRI were explored, mainly through modeling with the MGP-model. The analysis was carried out at different scales ranging from local scale at the Dahra test site through to the continental scale presented in Paper I. The continental scale study showed that the three main factors controlling the magnitude of the directional effects are the difference between the surface component temperatures, the tree crown cover and the sun-target-sensor geometry. Furthermore, tree and crown size, shape and density also affect the magnitude of the directional effects.

- *Difference between component temperatures.* Without a significant temperature difference between the different surface components, the surface will not show any directional effects. Furthermore, the larger the difference, the larger the directional effects can potentially be, but the magnitude will then be determined by the other factors described below.
- *Tree crown cover.* The continental study (Paper I) found that the largest directional effects were found in areas with between 30 and 40 % tree crown cover. This neglects any dependence the tree crown cover might have on the temperature difference between the different surface components, as these were assigned uniformly across the continent in Paper I. Assuming that the tree crown cover depends on the availability of water, which also to some extent controls the temperature difference between the surface components, it could be assumed that the difference between surface components would be higher for areas with less tree crown cover. This would mean that the largest

directional effects would occur at slightly lower values of tree crown cover than otherwise expected. Paper II generally confirms the findings from Paper I, but also highlights that even in areas with considerably lower tree crown cover (e.g. 8%), significant directional effects occur.

- *Sun Zenith angle*. The potential directional effect increase as the sun zenith angles gets closer to nadir view (0 degrees sun zenith). This is mainly caused by the fact that nadir view is used as a reference. In cases with sun zenith angles close to nadir, nadir view will be at hot spot geometry, meaning that only the sunlit components will be in view of the sensor causing high composite temperature for nadir view. So rather than being a true dependence on sun zenith angle, this is more a dependence on the nadir-view having hot spot geometry.

- *Relative azimuth angle (RAA)*. As above, the main influence of the relative azimuth (the angle between the sun and the sensor as seen from the point on the ground) stems from the occurrence of hot spot or close-to hot spot geometries. This means that the largest (in this case negative) temperature differences between nadir and MSG SEVIRI view occur at RAA values close to 0 and 360. These are the cases with principal plane conditions AND where the sun and the sensor are located at the same side of the target. This excludes the cases with principal plane conditions where the sun and sensor are located on opposite sites of the sensor. It will still mean that in general, the largest directional effects are found in the principal plane compared to cross principal plane conditions, but this is only caused by the high differences for the same-side cases.

In summary for the two angular dependencies discussed above, the magnitude of the directional effects depend largely on whether one of the two views are close to hot spot geometry. In these cases, the potential directional effects will be largest compared to cases where none of the two views are close to hot spot geometry. Furthermore, the sign of the directional effect will depend, at least partly, on which of the views is close to hot spot geometry.

In addition to the above mentioned factors influencing the magnitude of the directional effects, the tree size, shape and crown density are also important. But the exact influence of these parameters is not independent of the above mentioned factors, making it impossible to make general rules about their influence. For example, the crown density (expressed through the Leaf Area Index (LAI)) will increase the magnitude of the directional effects in areas with sparse tree cover, while it will decrease the magnitude in areas with more dense tree cover.

A finding that will be important for many applications of LST data, is that the directional effects can be expected to change both in terms of magnitude and sign over the course of the day, as well as with season. This is illustrated in figure 4.1 taken

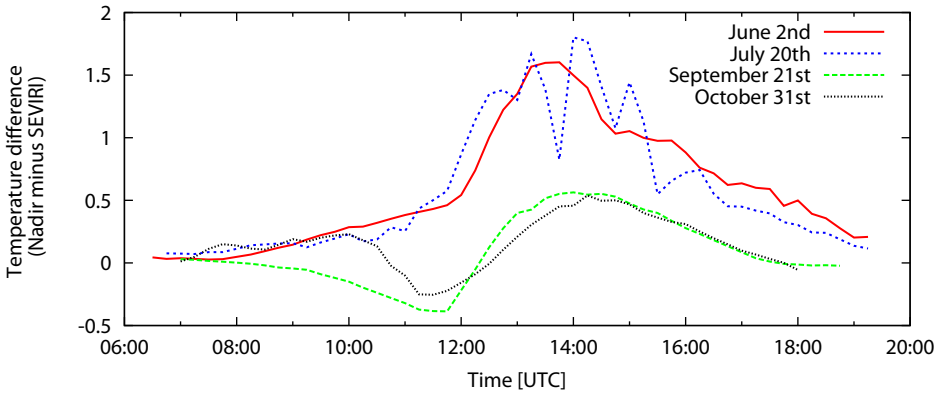

Figure 4.1: Examples of the diurnal changes in the temperature difference between nadir and MSG-view as modeled with the MGP-model for an area with 35% tree crown cover. Figure from Paper II.

from Paper II. It shows the diurnal and seasonal change in the modeled temperature difference between nadir and SERIVI-view for a case with 35% tree cover at the Dahra site (the true tree crown cover is 4%). On the daily scale, both the sign and the amplitude of the directional effects change significantly. The amplitude is more than one degree in three out of four cases, and in two cases the sign of the directional effect change during the day. On the seasonal scale, it is not uncommon to observe a difference of more than one degree if comparing the directional effects in summer to the effects in the fall. If this is not considered in applications of the LST data, it equals introducing a (for the user) "random error" of at least 1 K. In many cases, the directional effects will then be at the same order of magnitude as the quoted overall uncertainty estimate of the LST product itself.

Considering the magnitude of the (modeled) geometric effects found in Papers I and II, it should be possible to identify these effects in LST data, at least in the most affected areas. The assessment of whether it is feasible to identify the directional effects in SEVIRI-based estimates of LST is based on the assumption, that the performance of the LST products follows the estimates of uncertainty given by the data provider. A test of LST-estimation performance was carried out in Paper IV, by intercomparing different SEVIRI-based LST products as well as comparing the satellite data to *in situ* measurements from two field sites in semi-arid West Africa. Performance of all the satellite based LST-estimates were found to be discouraging when comparing with the ground data, with discrepancies exceeding 5 degrees in the majority of cases. The inadequate performance was found especially during the rainy season, while the results for the dry season were better. The large discrepancies, which by far exceeds the expected uncertainties in the LSA-SAF LST product, makes it infeasible to identify directional effects in the satellite data, as other sources of uncertainty will mask out the directional effects. At least this is true during the rainy

season, while it might be possible in the dry season, although ground data from more densely vegetated areas than the Dahra site will be required. As mentioned above, the directional effects depend on the temperature difference between the surface components, which can be expected to be larger during the dry season. This should make the identification of the directional effects easier during the dry season, further enhancing the possibilities of identifying these effects in the satellite data.

4.2 Perspectives on how to operationally correct for directional effects

The directional effects identified in this study are in many cases significant and should ideally be accounted for. This is especially the case if using long time series of data for applications benefiting from the capabilities of the SEVIRI sensor for monitoring the diurnal cycle. But setting up a correction scheme is not a simple task. Two spectral measurements are available (one from each of the two thermal SEVIRI channels) at each time step, and ideally the influence of the atmosphere, the emissivity and temperatures of the four components, a total of 7 unknowns should be solved for (not counting the vegetation structure parameters). This is obviously an ill-posed problem which can not be solved numerically. Alternatives therefore have to be sought, in order to reduce the number of unknowns to be solved for, or increase the number of independent measurements available.

Several attempts have previously been made to invert radiative transfer models using bi- or multi-angular thermal infrared data to estimate component temperatures (Francois et al., 1997; Menenti et al., 2008; Timmermans et al., 2009; Verhoef et al., 2007). Common for these studies is that none of the studies succeed in developing a inversion-algorithm capable of producing stable results from satellite data on a broad scale, although the forward simulations show evidence of significant directional effects. Some limit themselves to try to invert for two component temperatures (ignoring the difference between sunlit and shaded sub-components), while acknowledging that this might very well be too crude an assumption when the temperature difference between these components are large (Menenti et al., 2008; Verhoef et al., 2007). In all studies, information on the vegetation structure (with varying degrees of detail) is required in order to carry out the inversion. This could be in the form of information on the Leaf Area Index alone, while other approaches require extensive information on leaf inclination distribution and the structural arrangement of the leaves. The requirement of detailed input data on vegetation properties limits the applicability of these methods on the broader scale, as it is unlikely that this information would be available. For the simpler methods, this could be dealt with, which is also suggested by the authors (Menenti et al., 2008; Timmermans et al., 2009; Verhoef et al., 2007), by combining the thermal measurements with data from the visible part of the spectrum from which information on e.g. the canopy structure can

be derived. Using BRDF-models for inferring vegetation structure has already been a subject of some research (e.g. Diner et al. (2005); Gao et al. (2003)), and results look promising. The main issue with this is, that the best estimates of these structural parameters, require multi-angular input data from sensors like the MISR-sensor, that monitor the surface quasi-instantaneously at 9 different angles (VIS only). This further stresses the point, which is also evident from the inversion-studies discussed above: Multi-angular data is almost a requirement if a correction scheme is to be set up successfully, but is not necessarily enough on its own. This has previously been attempted for data from the ATSR and AATSR-sensors that measured the surface at two angles - nadir and 53 degrees forward (Francois et al., 1997; Menenti et al., 2008) with some success. A sensor setup like the (A)ATSR is obviously not possible from a geostationary orbit as it requires the sensor to move across the land surface, and would thus require more sensors in orbit at the same time with appropriate angular spacing (more than the current 9.5 degrees between MSG-1 and MSG-2). The question is if the fixed viewing geometry from two geostationary satellites would provide sufficient angular variation to allow for inversion across large areas (e.g. the Africa continent), which have proved to be a challenge in the case of BRDF-modeling (Proud, 2010). But even with measurements in two bands at two different angles from two SEVIRI sensors, inversion will not be straight forward as the system of equations will still be underdetermined.

Bibliography

Becker, F., Li, Z.-L., 1990. Towards a local split window method over land surfaces. International Journal of Remote Sensing 11, 369 – 393.

Caselles, V., Sobrino, J. A., Coll, C., 1992. A physical model for interpreting the land surface temperature obtained by remote sensors over incomplete canopies. Remote Sensing of Environment 39 (3), 203 – 211.

Coret, L., Briottet, X., Kerr, Y. H., Chehbouni, A., 2004. Simulation Study of View Angle Effects on Thermal Infrared Measurements Over Heterogeneous Surfaces. IEEE Transactions on Geoscience and Remote Sensing 42 (3), 664–672.

Cuenca, J., Sobrino, J. A., 2004. Experimental measurements for studying angular and spectral variation of thermal infrared emissivity. Applied Optics 43, 4598–4602.

da Luz, B. R., Crowley, J. K., 2007. Spectral reflectance and emissivity features of broad leaf plants: Prospects for remote sensing in the thermal infrared (8.0-14.0μm). Remote Sensing of Environment 109 (4), 393 – 405.

Dash, P., Göttsche, F.-M., Olesen, F.-S., Fischer, H., 2002. Land surface temperature and emissivity estimation from passive sensor data: theory and practice-current trends. International Journal of Remote Sensing 23, 2563–2594.

Diner, D. J., Braswell, B. H., Davies, R., Gobron, N., Hu, J., Jin, Y., Kahn, R. A., Knyazikhin, Y., Loeb, N., Muller, J.-P., Nolin, A. W., Pinty, B., Schaaf, C. B., Seiz, G., Stroeve, J., 2005. The value of multiangle measurements for retrieving structurally and radiatively consistent properties of clouds, aerosols, and surfaces. Remote Sensing of Environment 97 (4), 495 – 518.

EUMETSAT, Trigo, I., Freitas, S., Bioucas-Dias, J., Barroso, C., Monteiro, I., Viterbo, P., 2009. Algorithm Theoretical Basis Document for Land Surface Temperature (LST) (SAF/LAND/IM/ATBD_LST/1.0). Tech. rep., Eumetsat.

Francois, C., Ottle, C., Prevot, L., 1997. Analytical parameterization of canopy directional emissivity and directional radiance in the thermal infrared. application on the retrieval of soil and foliage temperatures using two directional measurements. International Journal of Remote Sensing 18, 2587–2621.

Freitas, S. C., Trigo, I. F., Bioucas-Dias, J. M., Göttsche, F.-M., 2010. Quantifying the Uncertainty of Land Surface Temperature Retrievals From SEVIRI/Meteosat. IEEE Transactions on Geoscience and Remote Sensing 48 (1), 523–534.

Gao, F., Schaaf, C. B., Strahler, A. H., Jin, Y., Li, X., 2003. Detecting vegetation structure using a kernel-based BRDF model. Remote Sensing of Environment 86, 198 – 205.

Gastellu-Etchegorry, J. P., Demarez, V., Pinel, V., Zagolski, F., 1996. Modeling radiative transfer in heterogeneous 3-d vegetation canopies. Remote Sensing of Environment 58 (2), 131 – 156.

Guillevic, P., Gastellu-Etchegorry, J. P., Demarty, J., Prvot, L., 2003. Thermal infrared radiative transfer within three-dimensional vegetation covers. Journal of Geophysical Research 108, 4248–4260.

Hansen, M., DeFries, R., Townshend, J., Carroll, M., Dimiceli, C., Sohlberg, R., 2003. Vegetation Continuous Fields MOD44B, 2001 Percent Tree Cover, Collection 3, University of Maryland, College Park, Maryland.
URL http://glcf.umiacs.umd.edu/data/vcf/

Jia, L., 2004. Modeling heat exchanges at the land-atmoshpere interface using multi-angular thermal infrared measurements. Ph.D. thesis, Wagening University, The Netherlands.

Jia, L., Li, Z.-L., Menenti, M., 2002. Modeling of tir radiative transfer in the soil-vegetation-atmosphere system: sensitivity to soil water content and lai and simulation of complex scenes. In: Geoscience and Remote Sensing Symposium. pp. 39–41, iSBN: 0-7803-7536-X.

Kimes, D., Idso, S., Jr., P. P., Reginato, R., Jackson, R., 1980. View angle effects in the radiometric measurement of plant canopy temperatures. Remote Sensing of Environment 10 (4), 273 – 284.

Kimes, D. S., 1981. Azimuthal radiometric temperature measurements of wheat canopies. Applied Optics 20 (7), 1119–1121.

Labed, J., Stoll, M. P., 1991. Angular variation of land surface spectral emissivity in the thermal infrared: laboratory investigations on bare soils. International Journal of Remote Sensing 12, 2299–2310.

Lagouarde, J. P., Kerr, Y. H., Brunet, Y., 1995. An experimental study of angular effects on surface temperature for various plant canopies and bare soils. Agricultural and Forest Meteorology 77 (3-4), 167 – 190.

Li, X., Strahler, A., 1992. Geometric-optical bidirectional reflectance modeling of the discrete crown vegetation canopy: effect of crown shape and mutual shadowing. IEEE Transactions on Geoscience and Remote Sensing 30 (2), 276–292.

Li, X., Strahler, A. H., Friedl, M. A., 1999. A Conceptual Model for Effective Directional Emissivity from Nonisothermal Surfaces. IEEE Transactions on Geoscience and Remote Sensing 37 (5), 2508–2517.

Menenti, M., Jia, L., Li, Z.-L., 2008. Multi-angular Thermal Infrared Observations of Terrestrial Vegetation, in: Advances in Land Remote Sensing, Shunlin Liang (editor). Springer Netherlands, pp. 51–93.

Minnis, P., Khaiyer, M. M., 2000. Anisotropy of Land Surface Skin Temperature Derived from Satellite Data. Journal of Applied Meteorology 39, 1117–1129.

Ni, W., Li, X., Woodcock, C. E., Caetano, M. R., Strahler, A. H., 1999. An analytical hybrid gort model for bidirectional reflectance over discontinuous plant canopies. IEEE Transactions on Geoscience and Remote Sensing 37, 987–999.

Pinheiro, A. C., Privette, J. L., Guillevic, P., 2006. Modeling the observed angular anisotropy of land surface temperature in a Savanna. IEEE Transactions on Geoscience and Remote Sensing 44 (4), 1036–1047.

Pinheiro, A. C., Privette, J. L., Mahoney, R., Tucker, C. J., 2004. Directional effects in a daily AVHRR land surface temperature dataset over Africa. IEEE Transactions on Geoscience and Remote Sensing 42 (9), 1941–1954.

Pinheiro, A. C. D. T., 2003. Directional effects in observations of AVHRR land surface temperature over Africa. Ph.D. thesis, Universidade Nova de Lisboa.

Price, J. C., 1984. Land Surface Temperature Measurements From the Split Window Channels of the NOAA 7 Advanced Very High Resolution Radiometer. Journal of Geophysical Research 89, 7231–7237.

Proud, S. R., 2010. The Development of Angularly and Atmospherically Corrected Meteosat Second Generation Imagery. Ph.D. thesis, University of Copenhagen.

Schmetz, J., Pili, P., Tjemkes, S., Just, D., Kerkmann, J., Rota, S., Ratier, A., 2002. An Introduction to Meteosat Second Generation (MSG). Bulletin of the American Meteorological Society 83, 977–992.

Smith, J. A., Chauhan, N. S., Schmugge, T. J., Jr., J. R. B., 1997. Remote Sensing of Land Surface Temperature: The Directional Viewing Effect. IEEE Transactions on Geoscience and Remote Sensing 35, 4.

Snyder, W. C., Wan, Z., 1998. Brdf models to predict spectral reflectance and emissivity in the thermal infrared. IEEE Transactions on Geoscience and Remote Sensing 36, 214 – 225.

Snyder, W. C., Wan, Z., Zhang, Y., Feng, Y.-Z., 1997. Thermal infrared (3-14 [mu]m) bidirectional reflectance measurements of sands and soils. Remote Sensing of Environment 60 (1), 101 – 109.

Sobrino, J. A., Cuenca, J., 1999. Angular variation of thermal infrared emissivity for some natural surfaces from experimental measurements. Applied Optics 38, 3931–3936.

Sobrino, J. A., Jimnez-Muoz, J. C., Verhoef, W., 2005. Canopy directional emissivity: Comparison between models. Remote Sensing of Environment 99 (3), 304 – 314.

Timmermans, J., Verhoef, W., van der Tol, C., Su, Z., 2009. Retrieval of canopy component temperatures through bayesian inversion of directional thermal measurements. Hydrology and Earth System Sciences 13, 1249 – 1260.

Trigo, I. F., Monteiro, I. T., Olesen, F., Kabsch, E., 2008. An assessment of remotely sensed land surface temperature. Journal of Geophysical Research 113, 1–12.

Verhoef, W., Jia, L., Xiao, Q., Su, Z., 2007. Unified optical-thermal four-stream radiative transfer theory for homogeneous vegetation canopies. IEEE Transactions on Geoscience and Remote Sensing 45, 1808–1822.

Wan, Z., Dozier, J., 1996. A generalized split-window algorithm for retrieving land-surface temperature from space. IEEE Transactions on Geoscience and Remote Sensing 34, 892–905.

Yan, G., Friedl, M., Li, X., Wang, J., Zhu, C., Strahler, A. H., 2001. Modeling directional effects from nonisothermal land surfaces in wideband thermal infrared measurements. IEEE Transactions on Geoscience and Remote Sensing 39, 1095–1099.

Yu, Y., Pinheiro, A. C., Privette, J., August 2006. Correcting Land Surface Temperature Measurements for Directional Emissivity Over 3-D Structured Vegetation. In: Gao, W., Ustin, S. L. (Eds.), Proceedings of the SPIE Remote Sensing and Modeling of Ecosystems for Sustainability III. Vol. 6298.

Paper I

Modeling Angular Dependences in Land Surface Temperatures From the SEVIRI Instrument Onboard the Geostationary Meteosat Second Generation Satellites

Authors:

Mads Olander Rasmussen, Ana C. Pinheiro, Simon R. Proud and Inge Sandholt

Status:

Published in IEEE Transactions on Geoscience and Remote Sensing, vol. 48, no. 8, August, pp. 3123 - 3133.

Modeling Angular Dependences in Land Surface Temperatures From the SEVIRI Instrument Onboard the Geostationary Meteosat Second Generation Satellites

Mads Olander Rasmussen, Ana C. Pinheiro, Simon R. Proud, and Inge Sandholt, *Member, IEEE*

***Abstract*—Satellite-based estimates of land surface temperature (LST) are widely applied as an input to models. A model output is often very sensitive to error in the input data, and high-quality inputs are therefore essential. One of the main sources of errors in LST estimates is the dependence on vegetation structure and viewing and illumination geometry. Despite this, these effects are not considered in current operational LST products from neither polar-orbiting nor geostationary satellites. In this paper, we simulate the angular dependence that can be expected when estimating LST with the viewing geometry of the geostationary Meteosat Second Generation Spinning Enhanced Visible and Infrared Imager sensor across the African continent and compare it to a normalized view geometry. We use the modified geometric projection model that estimates the scene thermal infrared radiance from a surface covered by different land covers. The results show that the sun–target-sensor geometry plays a significant role in the estimated temperature, with variations strictly due to the angular configuration of more than ± 3 °C in some cases. On the continental scale, the average error is small except in hot-spot conditions, but large variations occur both geographically and temporally. The sun zenith angle, the amount of vegetation, and the vegetation structure are all shown to affect the magnitude of the errors. The findings highlight the need for taking the angular effects into account when applying LST estimates in models and when comparing LST estimates from different sensors or from different times, both on the daily and seasonal scale.**

***Index Terms*—Angular effects, anisotropy, land surface temperature (LST), Meteosat Second Generation (MSG) Spinning Enhanced Visible and Infrared Imager (SEVIRI).**

I. Introduction

LAND surface temperature (LST) is a key parameter in the land surface energy budget, and it is directly dependent on the local-scale conditions at the surface, as well as on larger scale atmospheric conditions. Therefore, it is also an important input parameter to many models, including soil-vegetation–atmosphere transfer (SVAT) models, hydrological models, and climate models. Geostationary satellites like the Meteosat Second Generation (MSG) series provide a way of obtaining LST on a regional or even continental scale at a temporal resolution of 15 min with a pixel spacing of 3 km. Observations of LST from space are restricted to cloud-free conditions, so the high temporal resolution makes geostationary satellite data the best option for monitoring LST. The capability of, e.g., SVAT models to simulate the energy partitioning at the surface depends to a large degree on the quality of the input data. Relative errors of 1 °C have been shown to severely affect model performance on a regional scale, and local fluxes can be influenced even more severely with 1 °C–3 °C, giving an uncertainty in flux estimation of up to 150 $W \cdot m^{-1}$ [1], [2].

LST as measured from medium- and coarse-resolution satellite sensors is generally not observed over a homogenous and horizontal surface consisting of just one material. It is rather a mixture of different land covers or pixel components, each with their own separate temperature and emissivity contributing to the measured signal depending on how much of the pixel each component covers. Furthermore, the angular configuration of the sun, the sensor, and the areas being measured plays an important role, as sunlit and shaded areas of the same land cover will have different temperatures. The sunlit portions of a certain land cover will, in general, be warmer than the shaded portion, but the difference between the two temperatures depends on the specific land cover and the availability of moisture.

Current algorithms for LST estimation from the MSG Spinning Enhanced Visible and Infrared Imager (SEVIRI), e.g., [3]–[6] do not take this angular dependence into account. The only angular component in, for example, [5] is a simple dependence on the view zenith angle, not taking the structure of the surface or the scene geometry into account. This problem has previously been investigated for polar-orbiting satellites [7], [8] but has not been investigated systematically for geostationary satellites, although Minnis and Khaiyer [9] found large differences between LST estimates from three Geostationary Operational Environmental Satellite (GOES) satellites for a number of test areas. Polar-orbiting satellites monitor the surface at the same local sun time on consecutive orbits, except for effects caused by sensor drift and time differences across the swath, but with large variation in the viewing geometry across the scene. Geostationary satellites, on the other hand, have a fixed

Manuscript received October 2, 2009; revised January 2, 2010. Date of publication April 5, 2010; date of current version July 21, 2010. This work was supported in part by the International Research School of Water Resources (FIVA) at the University of Copenhagen, Copenhagen, Denmark.

M. O. Rasmussen, S. R. Proud, and I. Sandholt are with the Department of Geography and Geology, University of Copenhagen, 1350 Copenhagen, Denmark (e-mail: mora@gras.ku.dk; is@geo.ku.dk).

A. C. Pinheiro is with the National Climatic Data Center, National Oceanic and Atmospheric Administration, Asheville, NC 28801-5001 USA (e-mail: Ana.Pinheiro@noaa.gov).

Color versions of one or more of the figures in this paper are available online at http://ieeexplore.ieee.org.

Digital Object Identifier 10.1109/TGRS.2010.2044509

0196-2892/$26.00 © 2010 IEEE

viewing geometry, while the illumination geometry changes for each recorded image. Both sensor types will be influenced by seasonal variations in the illumination geometry.

This study simulates the angular dependence of LST as seen by the MSG SEVIRI sensor, by using the modified geometric projection (MGP) model [7]. The model enables studies of the influence of vegetation cover and structure on the LST as measured from a satellite sensor given the illumination and viewing geometry. Two cases are modeled: one for the actual MSG SEVIRI viewing geometry (with the sensor located at 0° E over the equator) and one at nadir. This enables one to examine the magnitude of the angular dependence and its spatial and temporal distribution. Nadir geometry is used as a reference geometry, even though it will never be possible to monitor all pixels at nadir from a geostationary platform. The study is limited to only modeling continental Africa and Madagascar, although the angular dependence can be expected to be even more severe in Europe due to the high view and sun zenith angles (SZAs).

II. Background

The angular dependence of LST, particularly for structured canopies, has been known for a long time. Balick and Hutchinson [10] found up to 5 °C change in measured temperature per 10° change in view angle over a leafless deciduous forest. In their review paper, they [11] also stressed the need for taking the temperature of the different scene components into account when considering the directional infrared temperature measured by a sensor. They only considered two components, namely, soil and vegetation, and thus did not treat the shadowing effects occurring when considering structured canopies.

Coret *et al.* [12] did a simulation study of the view angle effects of surface heterogeneity on measured LST. They modeled a surface composed by two homogenous scene components, namely, bare soil and vegetation, and did therefore not consider structured canopies and the related shadowing effects. On the other hand, their model did take the angular dependence of the emissivity into account. They showed that the sensor configuration makes a strong impact in the retrieved scene composite temperatures. They make a distinction between sensors that measure a constant solid angle and sensors that are designed to measure the same area independently of the view angle. The latter ones show a much more distinct angular dependence, which can potentially be applied to describe the scene structure from remotely sensed data. They also find that the anisotropy of the land surface in terms of emissivity has a significant influence on measured brightness temperatures and that these effects should ideally be taken into account, particularly for data measured at high view zenith angles.

As mentioned previously, the problem of angular dependences of structured canopies has been addressed for the National Oceanic and Atmospheric Administration Advanced Very High Resolution Radiometer polar-orbiting satellites by Pinheiro *et al.* [7]. They investigated the directional dependence of LST induced by the changing geometry due to both the sensor drift and the changing season. They accomplished this by modeling how much of each pixel is covered by four (isothermal) endmembers (or pixel components) for a given sun-target-sensor geometry, using a geometric optics model called the MGP model [8]. They then assume that the composite pixel radiance is a linear combination of the emitted radiances of the four endmembers, weighted by the abundances. For an area with moderate tree cover, they found the LST to be closely related to the fraction of the sunlit background component, which is to be expected as this component has, in general, the highest temperature. They also identified the occurrence of a thermal hot-spot effect for situations where the sun is right behind the sensor. The geographical pattern of the occurrence of these hot-spot effects depends largely on the seasonal variation in the position of the sun. Overall, they found differences in simulated LSTs of ± 5 K and up to 9 K strictly due to the sun-target-sensor geometry variation. Their results showed that the change in scene component fractions and, thus, temperature dependence is largest in the principal plane. The MGP model applied in the study was evaluated against the discrete anisotropic radiative transfer (DART) model. A more complex layer-based radiative transfer model [13] also used DART for simulating scenes of open tree orchards as would be seen from the Advanced Spaceborne Thermal Emission and Reflection Radiometer sensor, considering the effects of different leaf area index (LAI), tree cover fractions, and temperature differences between tree canopy and soil background, as well as shadows. They successfully used this to distinguish between irrigated and rain-fed olive orchards monitored over a six-year period. They also used DART for estimating the difference between crown and composite pixel temperatures and found differences of up to 20 K depending on the vegetation cover percentage.

Li *et al.* [14] developed a conceptual model for estimating the directional emissivity of nonisothermal heterogeneous surfaces. They also examined the 3-D effects of structured canopies through geometric optics considerations. This is a similar approach to the one adopted in [8], but it treats the emissivity and not LST, although the two problems are closely related.

Trigo *et al.* [15] investigated differences between MSG-SEVIRI- and Moderate Resolution Imaging Spectroradiometer (MODIS)-derived LSTs over three areas across the Earth disk. They also compared these to *in situ* measurements from a site in Portugal. They attributed the large differences between the MSG SEVIRI and MODIS LST values during the day to a number of factors, including the MODIS view zenith angle, time of day, sun scene view geometry, terrain orography, and surface type. They found that the MODIS view zenith angle played a significant role for the morning overpass, with temperature differences between MODIS and MSG SEVIRI reaching more than 6 °C in some cases. They attributed this to the fact that, when MODIS is observing a surface from the west, it views more shaded areas than does MSG SEVIRI, leading to the higher temperature difference at this time of the day. During nighttime, this dependence was absent, confirming that the dependence is related to the position of the sun in relation to the sensors. They also found a seasonal dependence that they attributed partly not only to changes in the fractions of sunlit and shadowed components over the year but also to changes in the vegetation. The largest differences occurred in the drier summer months, where the temperature difference between canopies and the soil/grass surfaces is largest. Trigo *et al.* [15] and Stisen *et al.* [16] found larger differences between LST estimates from

MODIS and MSG SEVIRI during daytime compared to nighttime. This indicates that solar heating causes a wider span in component temperatures and that the different viewing geometries influence the temperature differences between the two.

In a study examining LST estimates from three GOES satellites, Minnis and Khaiyer [9] also considered the angular dependencies. They examined a number of test areas mainly located in the Western and Central U.S. For these areas, estimates of LST were available from three different GOES satellites located at 75°, 105°, and 135° west. Their results show significant discrepancies in the temperature estimates from the three satellites and attribute this to the differences in SZA, view zenith angle, relative azimuth angle (RAA), vegetation cover type, and, particularly, the topography of the areas. They found temperature differences between two of the sensors of more than 10 K for some areas and found the magnitude of the differences to depend mainly on the topography of the areas and the vegetation cover.

III. Method

This study is designed to investigate the magnitude of the angular dependence of LST estimates from the MSG SEVIRI instrument in a number of *worst case* scenarios. This is done by modeling the LSTs that MSG SEVIRI would record for each pixel over the African continent in two cases: for the actual SEVIRI view geometry (located over the equator on the Greenwich Meridian) and at nadir view over each pixel. Having nadir observations for each pixel will not be possible from a geostationary sensor but is used as a common reference to allow intercomparison. Furthermore, this temperature at nadir could be used as a reference temperature when comparing observations from pixels with different viewing angles which would be similar to performing a bidirectional reflectance distribution function correction of reflectance values in the visible domain. If a normalization of the LST estimates to a common illumination and observation geometry is to be applied, nadir would likely be the geometry of reference.

Here, we address the magnitude of the angular effects over the African continent through model simulations of apparent pixel temperatures, based on the assumption that each pixel consists of a mix of only four scene components. These four components are sunlit canopy, shaded canopy, sunlit background, and shaded background. In this study, canopy refers to the tree or tall shrub canopies, and the term background refers to a surface covered by grasses or other low vegetation and/or bare soil. The model is capable of estimating the fraction that each of these components covers within a pixel, for a given illumination and viewing geometry, and the resulting pixel radiance is then a linear combination of the component-emitted radiances weighted by the fraction that each of the components covers, according to [8]

$$T_{\text{composite}} = \left[\frac{1}{\langle \varepsilon \rangle} \sum \left(\varepsilon_k T_k^4 f_k \right) \right]^{\frac{1}{4}} \tag{1}$$

where $T_{\text{composite}}$ is the composite temperature for a given pixel, $\langle \varepsilon \rangle$ is the composite emissivity, and f_k is the directional fractional cover of component k. This requires that the temperatures and emissivities of each of the pixel components are known. In this simulation study, the component temperatures and emissivities are set to constant values across the continent throughout time. Although this is a very crude assumption, it allows us for an *all-other-things-being-equal* comparison to identify in which regions these angular effects will occur and when they appear, due strictly to the sun-illumination geometry variation. To accomplish this, we ran the model for three different days during year 2007. Those days represent the extreme cases in terms of angular variation: the summer and winter solstices and the fall equinox.

A. Model Description

The MGP model is used to analyze the angular dependences of LST due to the geometrical structure of discontinuous canopies. The model was designed particularly for this purpose while still sufficiently accounting for both between- and within-tree-crown gap probabilities and being relatively computationally efficient to allow for regional-/continental-scale studies. A brief introduction to the model is given in the following. For a detailed description, interested readers should consult [7] and [8].

The MGP model is built on the geometric optics part of the Geometric Optical–Radiative Transfer (GORT) model [17] which is a radiative transfer code meant for modeling the bidirectional reflectance of discrete canopies. This model code allows for the estimation of how much of a given pixel is covered by a certain pixel component given the information on the vegetation structure and the illumination and viewing geometry. In the case of the current implementation, four pixel components are considered by the model: sunlit canopy, shaded canopy, sunlit background, and shaded background. Three of the pixel component fractions are estimated directly, whereas the fourth one, the shaded canopy, is estimated as the residual (constrained by the need for the fractions to sum to one). The canopy refers to trees and tall shrubs, and background refers to short vegetation (e.g., grasses) and/or bare soil. This distinction is made because the tree canopies have the largest influence on the measured temperature when considering illumination- and viewing-geometry-induced effects. The model effectively clumps together all tree canopies and all gaps (both between-crown and within-crown gaps), allowing the model to treat the vegetation as a homogenous layer [8]. The model assumes isotropic emissivity on the microscale, effectively ignoring the angular differences in emissivity for the single pixel components. On the other hand, it does account for the changes in the effective emissivity of the surface depending on how much of each pixel component is being seen by the sensor.

B. Input Data

The MGP model requires inputs on tree cover density and detailed information about the tree vegetation such as average crown height and crown width, as well as LAI. As an input to the model for the tree cover density on a continental scale, the MODIS Vegetation Continuous Fields product [18] for 2001 was applied (latitude/longitude, continental version). The original files with 1-km spatial resolution were aggregated to 8 km to

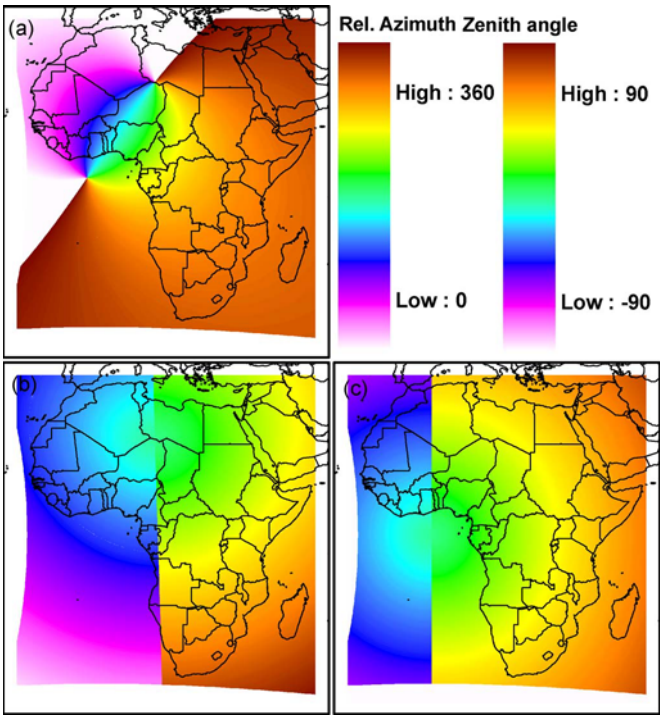

Fig. 1. (a) Relative azimuth, (b) SZA, and (c) view zenith angle for the same subset covering the African continent as shown in Figs. 3 and 4 for June 21, 2007, at 11:00 UTC.

match the scale of the vegetation structure parameters. LAI was obtained from the MOD/MYD15A2 product (collection 5) at 1-km resolution. This was reprojected and resampled to match the vegetation structure data at 8-km resolution using the MODIS Reprojection Tool [19].

Furthermore, the model needs angular information on both illumination and viewing geometries, including view zenith, view azimuth, sun zenith, and sun azimuth angles. The angular geometry for June 21, 2007, at 11:00 is shown in Fig. 1. As the SEVIRI sensor is aboard a geostationary satellite, the viewing geometry is fixed (disregarding the very rare changes in satellite positions and shifts in operational service between MSG-1 and MSG-2). The illumination geometry, on the other hand, changes both during the day and seasonally. During the day, the sun moves from east to west across the continent, but the latitude of this movement depends on the season. This is represented in the RAA. Here, the RAA is calculated as the clockwise angular distance between the sun and view azimuth angles and ranges between 0 ° and 360°. The full 360° range has been used to allow possible identification of asymmetry effects, resulting in different effects when the sun is east or west of the sensor (effective morning and afternoon asymmetry), which would not be possible to discern using a 180° range. Similarly, the sun and view zenith angles have been calculated in the −90 ° to 90° range, with negative values indicating zenith angles west of the sun and the sensor, respectively.

For the estimation of pixel temperatures, the model additionally requires temperatures and emissivities for each of the four pixel components. As the emissivity can be assumed to be independent of solar illumination, only two emissivities are required. The applied values can be found in Table I.

TABLE I
INPUT TEMPERATURE AND EMISSIVITY VALUES FOR THE FOUR PIXEL COMPONENTS

Scene component	Temperature	Emissivity
Sunlit Canopy	24°C	0.98
Shaded Canopy	23°C	0.98
Sunlit Background	33°C	0.95
Shaded Background	21°C	0.95

Vegetation structure data are based on literature values assigned to individual classes in a land cover classification map and were obtained from [7] with a spatial resolution of 8 km.

C. Experimental Setup

The study was designed to explore the extreme cases of angular variation and how these affect the LST across the African continent. Therefore, three dates during 2007 were selected which represent the extremes of the variation in viewing and illumination geometry: the solstices and the fall equinox. At summer solstice, the sun is positioned on the Tropic of Cancer located north of the MSG SEVIRI sensor and north of most of the continent. This will create high SZAs in the southern part of Africa and will also cause conditions in the afternoon in Southern Africa, where the sun, the MSG SEVIRI sensor, and the ground will be aligned. At the winter solstice, the sensor is located above the Tropic of Capricorn, causing high solar zenith angles over the northern part of the continent, and close to principal plane conditions in northwestern Africa in the mornings. At the equinoxes, the sun is located directly above the equator, where the sensor is also positioned. This will cause conditions where the sun is directly behind the sensor, where a thermal “hot-spot” effect could be expected.

As described previously, the MGP model requires the four pixel component temperatures as an input for each pixel. It is impossible to get these four temperatures for the entire continent simultaneously, as they cannot readily be derived from satellite measurements, and *in situ* measurements are naturally not possible on such a scale. In this study, the four pixel component temperatures have therefore been set to a constant value across the continent and with no diurnal variation (see Table I). These values are, of course, not representative of the actual temperatures as large variations occur depending on, among other things, time of day, season, and land cover. These temperatures have been chosen to represent the right magnitude of the temperature differences between the four pixel components for a surface with moderate vegetation cover. A typical example is a savannah with trees and a healthy grass cover. By keeping the temperatures for each component constant through space and time, we can more easily identify the effects upon temperature due to geometry variation only. Furthermore, as the composite emitted radiance is a linear combination of the pixel-component-emitted radiances, the actual temperatures applied are not that important for a modeling study like this. The conclusions drawn based on these temperatures can easily be transferred to other situations with different relative temperatures as the differences depend on the projected abundances of the four pixel components rather than the temperatures themselves.

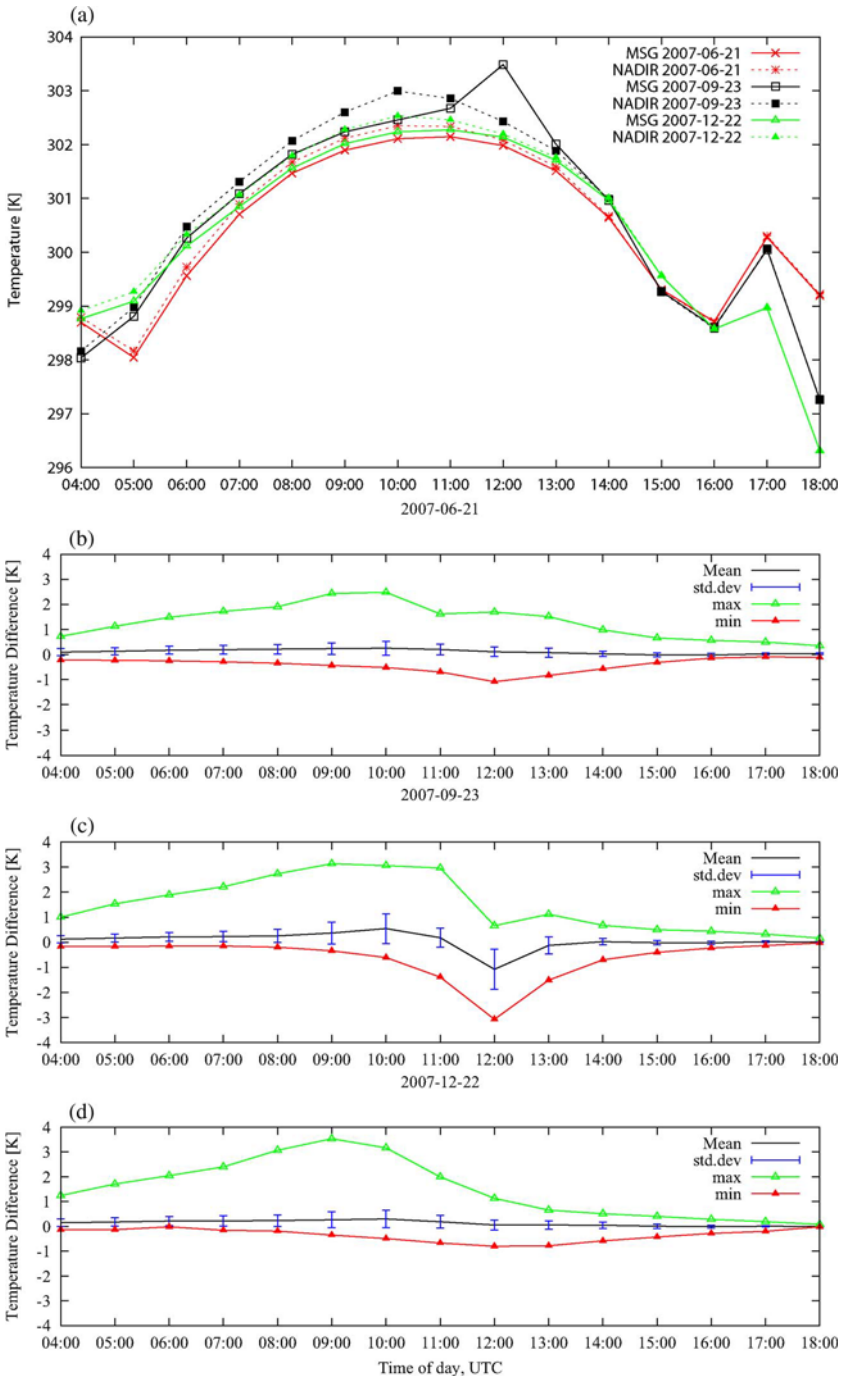

Fig. 2. (a) Average temperature from SEVIRI and nadir view, calculated as the mean of all modeled pixels as a function of the time of day, UTC time. (b)–(d) Mean, maximum, minimum, and standard deviation temperature difference, calculated as nadir minus SEVIRI for the three dates. All values are continental averages.

IV. Results and Discussion

A. Statistics

The result from the simulations includes the projected fractions of the four scene components, as well as LSTs for SEVIRI geometry and for nadir geometry. On average, the SEVIRI and nadir temperatures are very similar, both geographically and seasonally, but vary considerably over the day. The continentally averaged temperatures for the three days chosen for the study are shown in Fig. 2(a), hourly between 04:00 and 18:00 UTC. The temperature differences over the day are solely driven by the changes in angular configuration, as the scene component temperatures are held constant. The average temperatures vary between 296.3 K for the 18:00 slot for the December case and up to 303.5 K for the SEVIRI temperature at 12:00 for the September case. In most cases, the SEVIRI and nadir temperatures are very alike for each of the three dates. The only case where there is a significant difference is around noon on the equinox date. On this day (September 23, 2007), the nadir temperatures are higher from the morning up until 11:00 after which the SEVIRI temperatures are quite a lot higher for the 12:00 slot. After that, the two temperatures converge again.

In terms of the difference between the two temperatures, the average difference is just 0.11 K (averaged over all pixels for all time slots), and it only surpasses 0.3 K in the case of the equinox, where it reaches 0.5 K at 10:00 UTC and -1.1 K at 12:00 UTC (with standard deviations of 0.59 and 0.81 K, respectively). Although the mean temperature difference is generally not very large, significant temperature differences still occur at all three dates. The dips and peaks in the early morning and late afternoon in Fig. 2(a) are due to different parts of the continent being included/excluded due to the SZA cutoff at 80°.

As Fig. 2 also indicates, there is a large difference between how the three dates are affected. Only 0.48% of the pixels on June 21, 2007, have a temperature difference that is larger than ± 1 K, whereas it is 7.48% and 1.10% for September 23 and December 22, 2007, respectively. This clearly indicates that the time of year to a large degree controls how abundant the geometry-induced temperature differences are. On the other hand, significantly higher differences occur for all three dates, indicating that, locally, the errors can be larger than ± 1 K during a day.

B. Fraction of Each Scene Component and Temperature Difference

One of the main outputs from the model is the fractions of each of the four scene components. The model also outputs the directional composite temperature of each pixel, based on the provided scene component temperatures. An example of the fractions is shown for the summer solstice (June 21, 2007) at 11:00 UTC in Fig. 3, which shows the fractions as seen from the SEVIRI sensor (top) and the difference in fractions between nadir geometry and SEVIRI geometry (bottom). The temperature difference between the SEVIRI viewing geometry and the nadir viewing geometry is shown in Fig. 4. As mentioned, the composite emitted radiances are a linear combination of the scene-component-emitted radiances and, in this study, are closely related to the fraction of sunlit background, as this has the most distinct temperature (at least 9 K warmer than the other components). This can also be confirmed by comparing the difference in the sunlit background fraction in Fig. 3 with the temperature difference map for the same day and time in Fig. 4. These are very similar, although some differences are also apparent, e.g., on the east coast of Madagascar. The date and time shown in Fig. 4 are a typical midday example showing both areas where the SEVIRI geometry and the nadir geometry are warmest.

The two tree "crown" fractions summed show a spatial pattern that is close to that of the tree cover (a nadir-defined amount), but variations from this occur particularly at high view and sun angles. SEVIRI geometry generally has higher fractions of the "sunlit crown" component than nadir geometry, with the only exceptions occurring in areas that are very close to the sensor. The opposite is true for the "shaded crown" component, although more local-scale deviations are apparent.

Madagascar is a location where big differences occur over relatively short distances due to the large variations in the vegetation and the high view zenith angle of the MSG SEVIRI sensor in this area. On the east coast of Madagascar, the crown

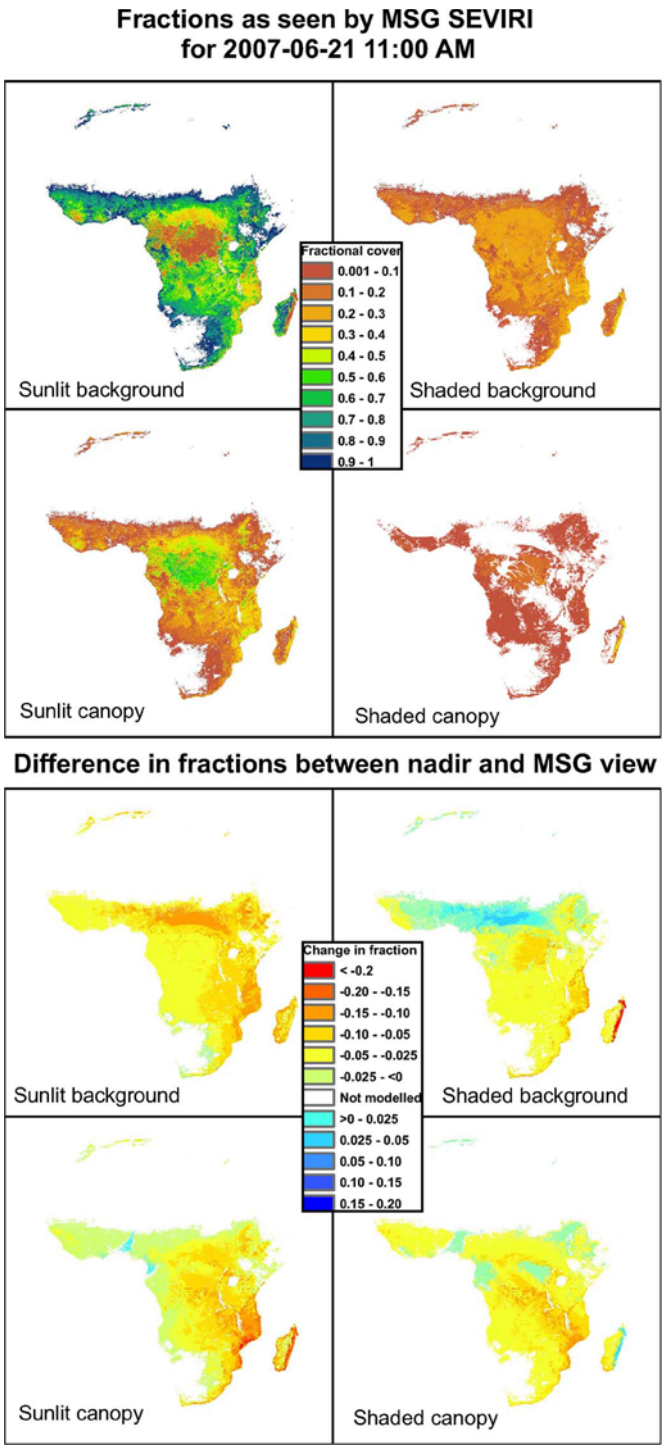

Fig. 3. (Top) Model output of the projected fractions for June 21, 2007, at 11:00 as seen from SEVIRI and (bottom) the difference between the fractions for SEVIRI view and nadir view calculated as nadir minus SEVIRI.

components dominate as tree cover is dense, not allowing SEVIRI to see much of the soil/background surface beneath the canopy. At nadir view, more of the background is seen, whereas the sunlit background is almost absent due to the dense tree cover and the position of the sun around the Tropic of Cancer ($23°26'$ N). The main difference in fractions between SEVIRI view and nadir view occurs in the "shaded background" component, which is also the coldest one of the four components. As

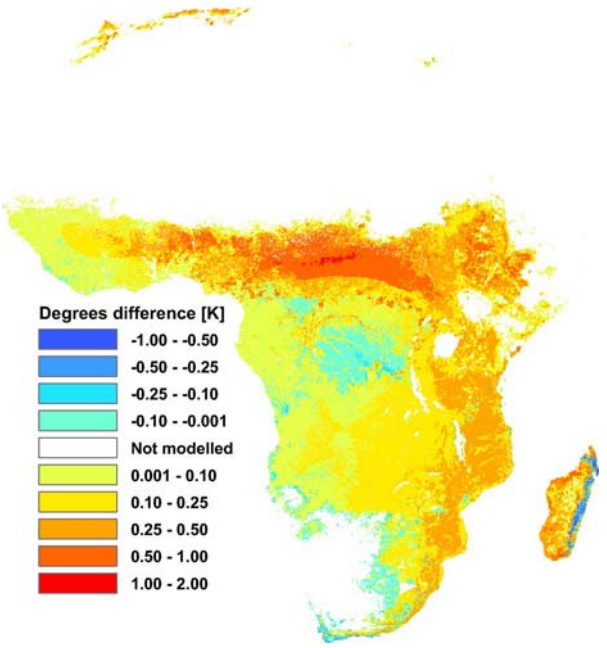

Fig. 4. LST difference for June 21, 2007, at 11:00. Yellow and red (blue) pixels show the cases where nadir view is warmest (coldest).

nadir view has the highest abundances of this component, the composite temperature is warmer as seen from SEVIRI than at nadir.

On the western side of Madagascar, conditions are rather different with much sparser vegetation. Again, SEVIRI geometry has higher fractions of the canopy components than nadir geometry, due to the higher viewing angle of the former. However, as the tree cover is much more sparse, the background components have a much larger influence on the composite temperatures. In this case where the sunlit background is more abundant, it becomes the dominant factor in the temperature difference, leading to higher composite temperatures for nadir view than SEVIRI view, mainly due to the high view zenith angle of SEVIRI.

In the densely vegetated central African region, SEVIRI geometry gives higher temperatures than nadir geometry. This is caused by the largest difference in fractions occurring for the sunlit canopy component combined with the almost absent sunlit background component. Most pixels in these areas actually have more sunlit background at nadir view compared to SEVIRI view, which should lead us to expect a higher composite temperature at nadir, but this is countered by the relatively larger fraction of sunlit canopy for SEVIRI geometry. The same explanation is generally true for the few areas in West Africa, where SEVIRI also has the highest composite temperatures in this example.

The area showing the most consistent higher composite temperatures at nadir geometry is the southern part of the Sahel zone in Sudan, the Central African Republic, and Chad. This region is located at the transition between the Sahara desert to the north and the densely vegetated areas in Central Africa to the south. This area generally has moderate tree cover, and the typical land cover is woody savannah. The relatively large temperature difference can be explained by the large difference between

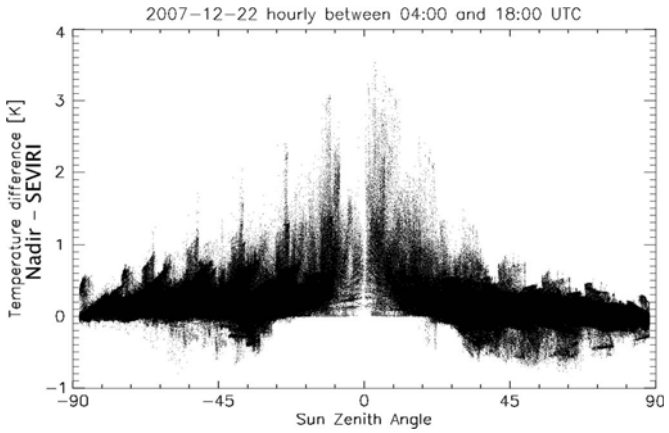

Fig. 5. LST difference as a function of SZA for December 22, 2007. All modeled pixels for all 15 model runs, hourly from 04:00 to 18:00, are included.

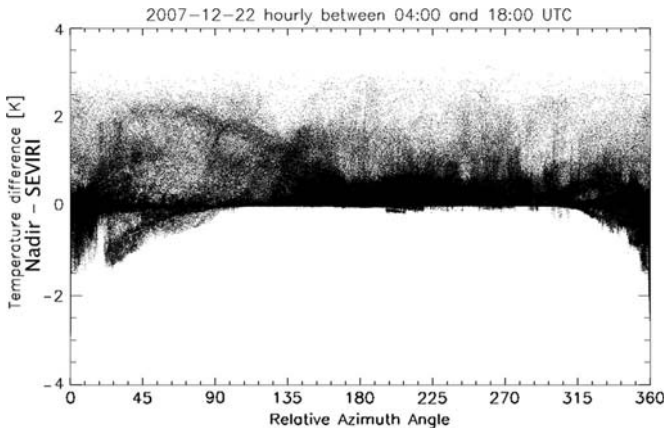

Fig. 6. LST difference as a function of RAA.

how much of the sunlit background component is seen in the two geometries. Nadir view has approximately 10% higher values of this fraction than SEVIRI view, causing the high temperature of this component to dominate the composite temperature.

C. LST Difference as a Function of SZA

The LST difference (between SEVIRI geometry and nadir geometry) shows a strong dependence on the SZA (see Fig. 5). This was also to be expected, as the temperature difference is a difference between the SEVIRI and nadir view configuration. In cases where the SZA is close to zero, the sun will effectively be placed right behind the sensor, causing the nadir view configuration to solely see the sunlit fractions. Therefore, it should be expected that there is a large positive difference in these cases. Cases where the SZA is very large (both negative and positive) occur early in the morning and late in the afternoon on the opposite side of the continent from the sun. In these cases, the SEVIRI view geometry will be closer to the sun than nadir geometry, causing the SEVIRI-geometry-derived LST estimates to be warmest. This will lead to negative differences, which is also evident in the data.

D. LST Difference as a Function of RAA

The only one of the three days showing a clear dependence of LST on RAA is the fall equinox shown in Fig. 6. The figure

contains data from 04:00 to 18:00 UTC, but the values actually contributing to the negative temperature difference values occur mainly between 11:00 and 13:00 UTC. It shows that, in the case of the thermal hot-spot effect, pixels that are close to the principal plane show not only the highest variation in surface temperature but also the most significant cases where SEVIRI geometry results in higher temperatures than nadir geometry. This can be explained by the fact that nadir and near-nadir geometries will only occur for a limited number of pixels in an image. In the case of the thermal hot-spot effect occurring at 12:00 UTC at the fall equinox, almost all pixels in the image will be warmer with SEVIRI geometry and will all have RAAs that are very close to the principal plane. The large negative values mentioned previously occur for pixels that are close to the principal plane but only in cases where the sun and the sensor are located on the same side of the pixel in question. RAAs around 180° are also in the principal plane but occur when the sun and the sensor are on the opposite sides of the pixel. These pixels do not show the same large variation in temperature differences as the pixels which are close to 0° and 360° RAA; furthermore, the sign of the differences is generally different for the two cases with the near-180° cases being positive (nadir geometry warmest) and the near-0° and near-360° cases being negative (SEVIRI geometry warmest).

E. Hot-Spot Effects

One of the most severe angular effects occurs when the sun is located right behind the sensor. In the visible domain, this is usually referred to as the hot-spot effect, as many vegetated surfaces have preferential reflectance in this direction, causing a peak in the reflectance. In the thermal domain, we also get a peak at the hot-spot geometry. This is not caused by reflectance as in the visible domain, but the term hot-spot effect will nevertheless be used in this study. The effect occurs due to an absence of shaded surface in the area observed by the sensor.

The hot-spot effect is also very apparent in the modeled temperatures in this study, exemplified by the large dip in the temperature difference curve in Fig. 2(c) for September 23, 2007, at 12:00 UTC, where the sun is located right behind the sensor. Fig. 7(b) shows the occurrence of the hot-spot effect in an area located approximately 5° north of the equator (27.6° east) just north of the border between the Democratic Republic of the Congo and Sudan. Comparing this to the summer case in Fig. 7(a), it shows absence of this effect. For the hot-spot case, the diurnal temperature difference is 4 K, compared to 1 K for the summer case. The large temperature difference dip occurring at 13:50 local sun time (12:00 UTC) is clearly caused by the large increase in the fraction of the sunlit background. The positive temperatures at 10:50 and 11:50 can, on the other hand, be explained by the hot-spot effect occurring at 11:50 at this position for the nadir geometry.

F. LST Difference as a Function of Tree Cover

One of the factors also having a clear effect on the temperature differences is the tree cover amount. This is to be expected because the effect of changing geometry must be largest for areas with moderate tree cover as the component fractions do not change with geometry for neither unvegetated surfaces nor surfaces with a dense homogenous layer of vegetation. A bell-shaped dependence of temperature difference upon tree cover has also been found earlier in other studies [7], [15].

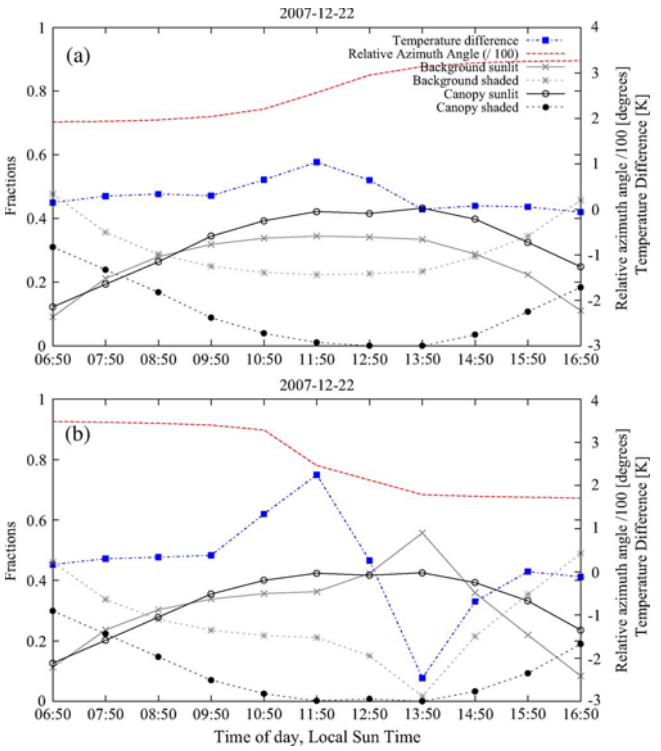

Fig. 7. Fractions as seen from SEVIRI and mean temperature difference for one 3 × 3 pixel area in Central Africa for the two dates (a) June 21 and (b) September 23, 2007. The fall equinox day clearly shows the effect of the hot-spot geometry for the canopy components and in the temperature difference.

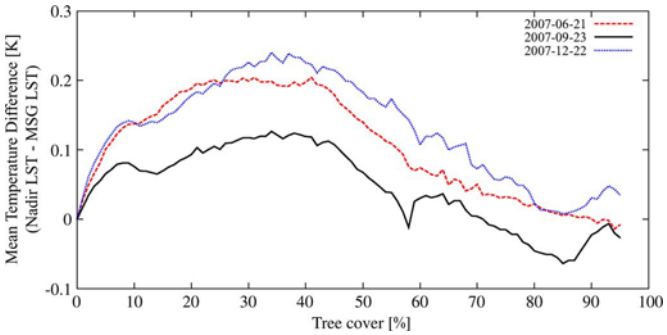

Fig. 8. Average temperature difference (calculated as nadir minus SEVIRI) as a function of tree cover percent. The values are calculated as an average for all pixels at all 15 modeled times throughout the day, within a one-percentage tree cover bin.

Fig. 8 shows the average temperature difference between nadir and SEVIRI geometry as a function of the tree cover, calculated as the average temperature difference for each pixel, including all 15 model runs per day. All three dates show the expected bell-shaped curve, with the maximum occurring at tree covers between 30% and 40%. On average, nadir geometry tends to be warmer for low and moderate tree covers, while the difference between the two is much lower at high tree covers. For one date, September 23, 2007, SEVIRI geometry is systematically warmer, where the tree cover is above 70%.

TABLE II
TOP POINT OF THE FITTED SECOND-ORDER FUNCTION AND THE CORRESPONDING TEMPERATURE DIFFERENCE VALUE FOR THE THREE DATES (SEE THE TEXT FOR FURTHER EXPLANATION)

Date	Max	LST_{diff}
2007-06-21	35.42%	0.19
2007-09-23	32.29%	0.10
2007-12-22	38.26%	0.21

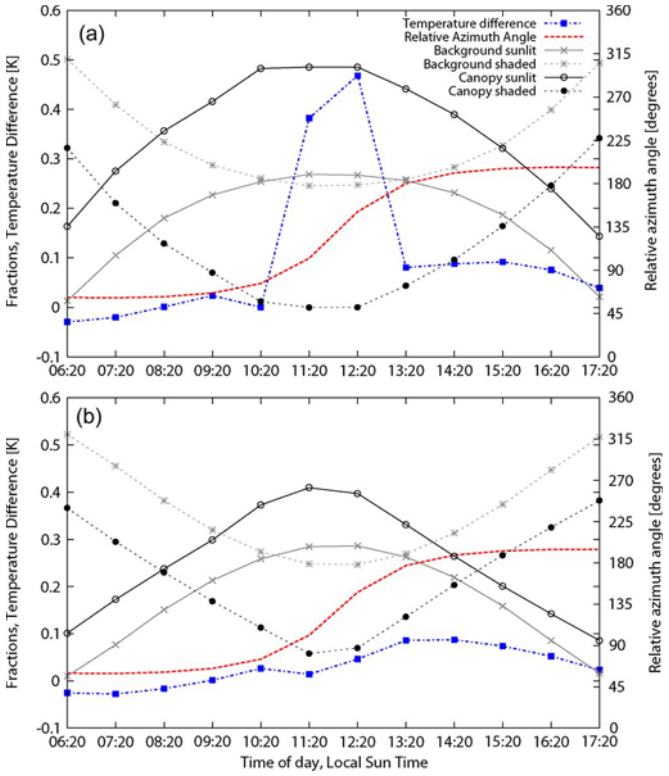

Fig. 9. Mean fractions as seen from SEVIRI, temperature difference, and RAA for two 3 × 3 pixel areas in northern Liberia for the day June 21, 2007. The tree cover and position of the two places are almost identical. Tree sizes vary considerably, with the trees being higher and with larger and denser crowns in (b) than in (a).

To investigate this dependence further, a second-order polynomial was fitted to the data for each of the three dates. The maximum of these functions is then found to identify at what value the model is most sensitive to the tree cover fraction. The results are shown in Table II, which shows both the maxima of the functions and the corresponding temperature differences. For all three dates, the function maxima occur within the 30%–40% interval. The average maximum difference is only around 0.2 K, but it must be stressed that these are average values and that differences, locally, can be more than 2 K. The significantly lower average temperature difference for September 23, 2007, is caused by the large negative temperature difference values for the 12:00 UTC slot [as also shown in Fig. 2(c)].

G. Influence of Vegetation Structural Parameters

Furthermore, we evaluated the impact of canopy size and shape on the LST difference. In some cases, not only the amount of tree cover or the angular configuration causes temperature differences between nadir and SEVIRI view geometry. For example, there is only a small difference in tree cover

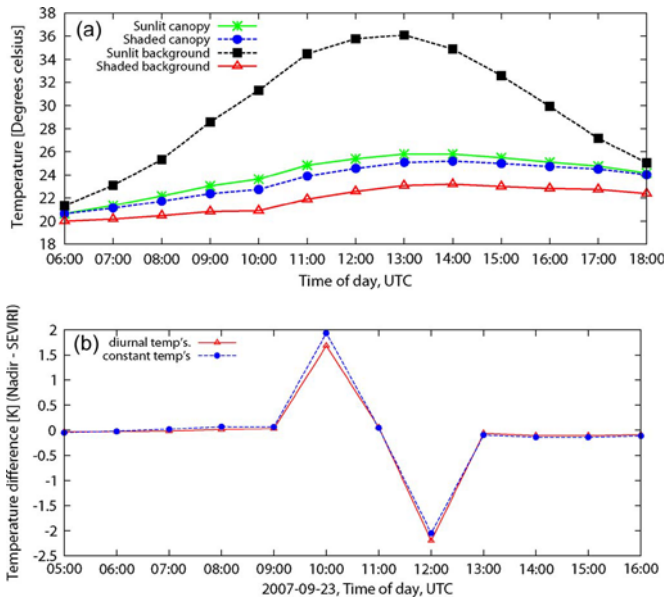

Fig. 10. (a) Diurnally varying component temperatures used for a sensitivity run and (b) typical example of the diurnal variation in the temperature difference with and without the varying component temperatures for a location in Central Africa.

percentage (approximately 5%) between the two areas shown in Fig. 9(a) and (b). The two locations are located only about 60 km apart in northern Liberia. However, the main difference is in the tree and crown structural parameters of the two sites, with the area shown in Fig. 9(b) dominated by much larger trees than the area in Fig. 9(a). They are not only larger in terms of height but also with denser and larger crowns, both horizontally and vertically.

It is obvious that the area in Fig. 9(a) has much larger fractions of shaded crown than the other area, whereas the area in Fig. 9(b) has more sunlit background. This causes the area in Fig. 9(a) to have a larger temperature difference, with an amplitude of 0.5 K, compared to an amplitude of 0.1–0.2 K for the area in Fig. 9(b).

H. Sensitivity to Diurnal Variation in Component Temperatures

To test the validity of the results obtained using component temperatures that are constant over the day, a model run was carried out with diurnally varying component temperatures. A time series of component temperatures was made partly using measured temperatures from a field site in northern Senegal and partly matching the applied component temperatures from Table I. The applied diurnally varying component temperatures are shown in Fig. 10(a).

Fig. 10(b) shows a typical example of the diurnal variation in the temperature difference between nadir and SEVIRI geometry for the fall equinox case. It shows the general trend found that the temperature difference is generally insensitive to whether the temperatures are kept constant or vary over the day. For this to be true, it requires that the temperatures of the individual components do not change order but keep their respective position in relation to the others. Moreover, the LST estimates themselves do not follow this pattern, but it applies, in most cases, to the temperature difference. This means that, except

TABLE III
INPUT COMPONENT TEMPERATURES FOR THE ORIGINAL AND ALTERNATE MODEL RUNS

Scene component	Original temps.	Alternate temps.
Sunlit Canopy	24°C	26°C
Shaded Canopy	23°C	22°C
Sunlit Background	33°C	30°C
Shaded Background	21°C	24°C

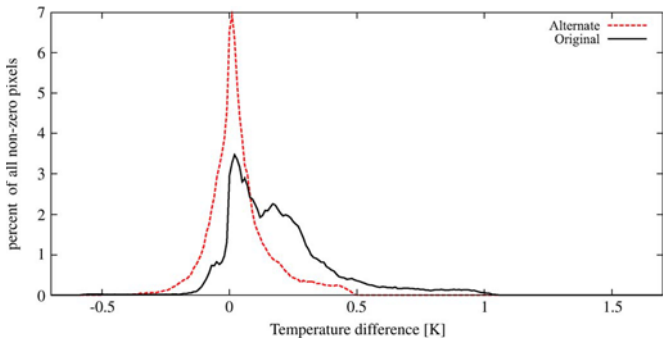

Fig. 11. Distribution of the LST differences for June 21, 2007, at 11:00 for the original and alternate sets of component temperatures.

for the temperatures shown in Fig. 2(a), the results presented in this paper are generally insensitive to whether the component temperatures are held constant or vary over the day.

I. Sensitivity to Component Temperatures

To test the sensitivity of the model to the selected component temperatures, an alternate model run was made for June 21, 2007, at 11:00 using a different set of temperatures (see Table III). The fractions are unchanged as neither tree density, the structural parameters, nor LAI was changed. Several changes were made to the component temperatures, including decreasing the difference between the coldest and warmest temperatures, as well as changing the order of the two shaded components. These temperatures were chosen to show a case that could represent either a morning situation before the surface has been heated to the maximum temperatures. Alternatively, it could represent the component temperatures that are typical for a denser vegetated area, where plenty of moisture is available for evapotranspiration. This would result in a narrower span in the component temperatures than the temperatures used for the original model run. The results in terms of the nadir–SEVIRI temperature differences are shown in Fig. 11. The effect of the lower sunlit background component temperature is clearly visible in the generally much lower temperature differences. Moreover, the entire distribution is shifted toward the left of the plot, caused by more pixels which now have the highest temperature for SEVIRI geometry. In general, the narrower the span of the component temperatures is, the less the temperature differences can be expected. Spatially, the dependence is more complex, as it depends on the fractions which, again, depend on a lot of different parameters, as described in the previous sections. As shown in the previous sections, the effects should be expected to be largest in areas with moderate tree cover, while barren and densely vegetated areas are less affected due to the relatively homogenous surface structure in such areas.

V. CONCLUDING REMARKS AND PERSPECTIVES

The model simulations show that the illumination and observation angular configuration can influence the estimated LST significantly. At the continental scale, the average error is generally insignificant, except at hot-spot geometry, but with relatively large variation in the occurrence of the temperature differences in terms of location and time. This makes it crucial to take the angular dependence into account before using the LST estimates as input to models or for trend identification in time series. Care should also be taken when combining data from geostationary satellites with data from polar-orbiting satellites, as the angular dependence will be different from the two types of sensors due to the difference in viewing geometry. The largest angular dependence occurs at hot-spot geometry when the sun is right behind the sensor, which, in this study, leads to temperature differences between SEVIRI and nadir of more than 3°. For the three days modeled: the summer and winter solstices and the fall equinox, 0.48%, 1.10%, and 7.48% of the pixels had a temperature difference of more than ± 1 °C, respectively. All days also showed a maximum temperature difference of more than 3 °C, with the fall equinox having the largest difference of more than 6 °C over the day.

Many assumptions were made in this study, including the following: uniform scene component temperatures across the continent that do not change during the day, no surface orography, and isotropic component emission. Despite this, the results still demonstrate the magnitude of the dependence of the LST estimates on the angular configuration and land surface cover. The composite temperature of a pixel is mainly controlled by how large a fraction of each scene component is viewed from a sensor at a given time but will also depend on the temperature difference between the components. Higher differences between the component temperatures will also lead to higher temperature differences. The component temperatures will vary diurnally and seasonally depending not only on the illumination geometry but also on vegetation cover and availability of water at the surface.

As mentioned, current LST products do not take the angular effects described in this study into account. The magnitude of the potential errors found therefore indicates that the error estimates of the current products are too optimistic, causing false confidence in downstream applications of the LST data. A correction/normalization scheme is required if the LST data are to be used for seasonal studies or for studies exploiting the capabilities of the SEVIRI sensor for monitoring diurnal variations. The MGP model applied in this study is not directly suited for a correction scheme, as the model is computationally demanding and requires the component temperatures to be known, which is not possible over a larger region.

ACKNOWLEDGMENT

Part of this work was carried out while M. O. Rasmussen was a Visiting Scientist at the Remote Sensing and Applications Division, National Climatic Data Center, National Oceanic and Atmospheric Administration. The authors would like to thank J. Privette and J. J. Bates for making the stay possible and

for taking care of the administrative work associated with the visit. This work contributes to the African Monsoon Multidisciplinary Analysis (AMMA) Project (http://www.amma-international.org). Based on a French initiative, AMMA was built by an international scientific group and is currently funded by a large number of agencies, particularly from France, U.K., U.S., and Africa. It has been the beneficiary of a major financial contribution from the European Community's Sixth Framework Research Program.

REFERENCES

[1] W. P. Kustas and J. M. Norman, "Use of remote sensing for evapotranspiration monitoring over land surfaces," *Hydrol. Sci.*, vol. 41, no. 4, pp. 495–516, 1996.

[2] P. J. Sellers, B. W. Meeson, F. G. Hall, G. Asrar, R. E. Murphy, R. A. Schiffer, F. P. Bretherton, R. E. Dickinson, R. G. Ellingson, C. B. Field, K. F. Huemmrich, C. O. Justice, J. M. Melack, N. T. Roulet, D. S. Schimel, and P. D. Try, "Remote sensing of the land surface for studies of global change: Models—Algorithms—Experiments," *Remote Sens. Environ.*, vol. 51, no. 1, pp. 3–26, Jan. 1995.

[3] I. Trigo, C. Madeira, I. Monteiro, S. Coelho, C. Barroso, F. S. Olesen, F. Göttsche, and L. Peres, *Product User Manual, Land Surface Temperature*. EumetSat Land SAF, 2008.

[4] J. A. Sobrino and M. Romaguera, "Land surface temperature retrieval from MSG1-SEVIRI data," *Remote Sens. Environ.*, vol. 92, no. 2, pp. 247–254, Aug. 2004.

[5] M. Atitar and J. A. Sobrino, "A split-window algorithm for estimating LST from Meteosat 9 data: Test and comparison with *in situ* data and MODIS LSTs," *IEEE Geosci. Remote Sens. Lett.*, vol. 6, no. 1, pp. 122–126, Jan. 2009.

[6] J.-C. Jiménez-Muñoz and J. A. Sobrino, "Split-window coefficients for land surface temperature retrieval from low-resolution thermal infrared sensors," *IEEE Geosci. Remote Sens. Lett.*, vol. 5, no. 4, pp. 806–809, Oct. 2008.

[7] A. C. Pinheiro, J. L. Privette, R. Mahoney, and C. J. Tucker, "Directional effects in a daily AVHRR land surface temperature dataset over Africa," *IEEE Trans. Geosci. Remote Sens.*, vol. 42, no. 9, pp. 1941–1954, Sep. 2004.

[8] A. C. Pinheiro, J. L. Privette, and P. Guillevic, "Modeling the observed angular anisotropy of land surface temperature in a savanna," *IEEE Trans. Geosci. Remote Sens.*, vol. 44, no. 4, pp. 1036–1047, Apr. 2006.

[9] P. Minnis and M. M. Khaiyer, "Anisotropy of land surface skin temperature derived from satellite data," *J. Appl. Meteorol.*, vol. 39, no. 7, pp. 1117–1129, Jul. 2000.

[10] L. Balick and B. A. Hutchinson, "Directional thermal infrared exitance distributions from a leafless deciduous forest," *IEEE Trans. Geosci. Remote Sens.*, vol. GE-24, no. 5, pp. 693–698, Sep. 1986.

[11] J. M. Norman, M. Divakarla, and N. S. Goel, "Algorithms for extracting information from remote thermal-IR observations of the Earth's surface," *Remote Sens. Environ.*, vol. 51, no. 1, pp. 157–168, Jan. 1995.

[12] L. Coret, X. Briottet, Y. H. Kerr, and A. Chehbouni, "Simulation study of view angle effects on thermal infrared measurements over heterogeneous surfaces," *IEEE Trans. Geosci. Remote Sens.*, vol. 42, no. 3, pp. 664–672, Mar. 2004.

[13] G. Sepulcre-Cantó, P. Zarco-Tejada, J. Sobrino, J. Berni, J. Jiménez-Muñoz, and J. Gastellu-Etchegorry, "Discriminating irrigated and rainfed olive orchards with thermal ASTER imagery and DART 3D simulation," *Agric. For. Meteorol.*, vol. 149, no. 6/7, pp. 962–975, Jun. 2009.

[14] X. Li, A. H. Strahler, and M. A. Friedl, "A conceptual model for effective directional emissivity from nonisothermal surfaces," *IEEE Trans. Geosci. Remote Sens.*, vol. 37, no. 5, pp. 2508–2517, Sep. 1999.

[15] I. F. Trigo, I. T. Monteiro, F. Olesen, and E. Kabsch, "An assessment of remotely sensed land surface temperature," *J. Geophys. Res.*, vol. 113, no. D17, pp. 1–12, 2008.

[16] S. Stisen, I. Sandholt, A. Noergaard, R. Fensholt, and L. Eklundh, "Estimation of diurnal air temperature using MSG SEVIRI data in West Africa," *Remote Sens. Environ.*, vol. 110, no. 2, pp. 262–274, Sep. 2007.

[17] X. Li and A. Strahler, "Geometric-optical bidirectional reflectance modeling of the discrete crown vegetation canopy: Effect of crown shape and mutual shadowing," *IEEE Trans. Geosci. Remote Sens.*, vol. 30, no. 2, pp. 276–292, Mar. 1992.

[18] M. Hansen, R. DeFries, J. Townshend, M. Carroll, C. Dimiceli, and R. Sohlberg, "Global percent tree cover at a spatial resolution of 500 meters: First results of the MODIS vegetation continuous fields algorithm," *Earth Interactions*, vol. 7, no. 10, pp. 1–15, Oct. 2003. [Online]. Available: http://glcf.umiacs.umd.edu/data/vcf/

[19] U. Land Processes DAAC, MODIS Reprojection Tool, ver 4.0, Feb. 2008. [Online]. Available: https://lpdaac.usgs.gov/lpdaac/tools/modis_reprojection_tool

Mads Olander Rasmussen received the B.S. degree in geoinformatics from the University of Copenhagen, Copenhagen, Denmark, in 2002, the M.S. degree in remote sensing from the University of London, London, U.K., in 2004, and the M.S. degree in geography from the University of Copenhagen in 2005, where he is currently working toward the Ph.D. degree in geography.

He has been a Visiting Research Scholar at the National Climatic Data Center, National Oceanic and Atmospheric Administration, Asheville, NC. He has also been working as a Remote Sensing Consultant for GRAS A/S, Copenhagen. His main research interests are medium- and coarse-resolution remote sensing of surface properties in both the visible and thermal domains, with spatial focus on Africa.

Ana C. Pinheiro received the B.S. degree in environmental engineering from the New University of Lisbon, Lisbon, Portugal, in 1995, the M.Eng. degree in civil and environmental engineering from the Massachusetts Institute of Technology, Cambridge, in 1998, and the Ph.D. degree in environmental engineering from the New University of Lisbon in 2003. She conducted her doctoral research as a Visiting Scientist in the Biospheric Sciences Branch, Goddard Space Flight Center (GSFC), National Aeronautics and Space Administration (NASA), Greenbelt, MD.

In November 2003, she joined the NASA GSFC Hydrological Sciences Branch as a National Research Council Postdoctoral Fellow, where she was a NASA Postdoctoral Program Fellow from January 2006 to January 2007. Since February 2007, she has been an STG Inc. Contractor with the National Climatic Data Center, National Oceanic and Atmospheric Administration, Asheville, NC.

Simon R. Proud received the M.Phys. degree in physics and spacecraft technology from the University of Leicester, Leicester, U.K., in 2006. He is currently working toward the Ph.D. degree at the University of Copenhagen, Copenhagen, Denmark.

In 2007, he joined Boston University, Boston, MA, for four months and also acted as a Parabolic Flight Consultant for the European Space Agency/German Aerospace Center (DLR). His areas of expertise include angular and atmospheric correction of remotely sensed data, spacecraft instrumentation design, and launch vehicle trajectory analysis.

Mr. Proud is a member of the American Institute of Aeronautics and Astronautics and the British Interplanetary Society.

Inge Sandholt (M'02) received the M.S. degree in physical geography from the University of Copenhagen, Copenhagen, Denmark, in 1990 and the Ph.D. degree in statistics from the Royal Veterinary and Agricultural University, Frederiksberg, Denmark, in 1996.

She is currently an Associate Professor with the Department of Geography and Geology, University of Copenhagen. Her research interests are primarily remote sensing of evapotranspiration, terrestrial ecosystem modeling, in particular, large-scale distributed hydrological modeling, soil-vegetation-atmosphere transfer, and vegetation modeling. She has a keen interest in multidisciplinary approaches to assessment of climate change impacts in Africa, including the human dimension.

Paper II

Directional effects on land surface temperature estimation from Meteosat Second Generation for savanna landscapes

Authors:

Mads Olander Rasmussen, Frank-M. Göttsche, Folke-S. Olesen and Inge Sandholt

Status:

Submitted to IEEE Transactions on Geoscience and Remote Sensing on 28/7 2010. In review.

Directional Effects on Land Surface Temperature Estimation from Meteosat Second Generation for Savanna Landscapes

Mads Olander Rasmussen, Frank-M. Göttsche, Folke-S. Olesen, and Inge Sandholt *Member, IEEE*

***Abstract*—Structured canopies can show pronounced directional effects which influence land surface temperature (LST) estimates from thermal infrared (TIR) satellite data. The effects depend on illumination and viewing geometry, because changes in these two geometries effectively cause the sensor to "see" different fractions of the canopy, the "background" surface (bare soil or low vegetation), and shadow, of which the latter also depends on the specific geometry of the canopy and its structure. This study investigates these directional effects for a specific savanna site in West Africa and extends the findings to areas with denser tree crown cover. This is achieved by modelling the combined effects of the structured surface with a geometric optics model. The model assumes that the surface consists of four components: shaded and sunlit tree canopy and shaded and sunlit background. The brightness temperatures of these four surface components are provided by in-situ measurements at the validation site and emissivities are taken from the LSA-SAF project. The LST modelling is performed for the geometry of the geostationary Meteosat Second Generation and for nadir geometry. Analyses of the temperature differences between the LST estimates for the two geometries show that in many cases the directional effects exceed 1°C within a day, and that the timing and the sign of the effects change with season. Directional errors due to structured canopies are currently not considered in error estimates of operationally available LST products, e.g. the LSA-SAF LST product or the MODIS Land LST / emissivity product.**

***Index Terms*—Meteosat Second Generation, SEVIRI, Land Surface Temperature, Directional effects**

I. Introduction

THERE are a number of sources of uncertainty and error associated with deriving land surface temperature (LST) from satellite data. The most prominent are sensor noise, calibration errors, and imperfect atmospheric correction, especially with relation to the effect of variable amounts of water vapour in the atmosphere. A further complication is the assignment of a representative emissivity to the pixel in question. For time series of LST, as often needed as input for many applications, errors in co-registration of images will generate additional noise. Finally, the "directional effects" addressed in this paper will cause errors. These are combined effects of the temporal and spatial variation of the illumination and viewing geometry and of the specific properties of the observed land surface, in particular its vegetation cover. These effects have earlier been shown to introduce errors of more than five degrees in LST estimates from NOAA AVHRR data [1] and slightly less for the Spinning Enhanced Visible and Infrared Imager (SEVIRI) instrument [2] onboard Meteosat Second Generation (MSG) [3] with the highest errors occurring in savanna-areas with moderate tree cover.

The SEVIRI based Land Surface Analysis Satellite Applications Facility (LSA-SAF) LST product [4], [5] deals with these errors and uncertainties by including a "Quality Flag (QF) layer" and an "error-bar layer" [6], of which the latter contains an estimate of the standard LST error that accounts for sensor noise, uncertainties in the atmospheric correction, and error associated with emissivity. However, the LSA-SAF LST error estimate does not take "directional effects" of the surface into account (no LST products account for these effects to our knowledge). The present study focuses on this additional source of error and uncertainty. While errors and uncertainties due to calibration and estimation of emissivity are likely to vary relatively slowly (with the exception of changes due to precipitation or dew events [7]), effects of illumination and viewing geometry obviously vary diurnally as well as seasonally. This is particularly important for e.g. hydrological or SVAT-model applications which rely on a correct representation of the diurnal cycle. When LST-data are used as input to hydrological models, slowly varying errors, e.g. due to problems of estimating representative values for emissivity, may be partly compensated for during model calibration, whereas this is not necessarily possible for errors associated with the diurnal cycle.

This study investigates the directional effects in LST estimates from MSG / SEVIRI caused by the structure and properties of savanna vegetation. Depending on the abundance, size, shape, and spatial distribution of the tree-vegetation, the associated LST retrieved from satellite data differ for the same illumination and viewing geometry. Here, the directional effects for MSG viewing geometry and for nadir viewing geometry are simulated with the Modified Geometric Projection (MGP) model [1], [8] as a function of illumination geometry and variables describing the vegetation cover. For a given combination of vegetation structure, illumination and viewing geometry, and emissivities and temperatures of the individual surface components, the MGP model can estimate the directional thermal infrared radiance leaving the surface. For the period from June to the end of October 2009, which represents an entire growing season and covers a wide range

Manuscript received , 2010.

M. O. Rasmussen (email: mora@gras.ku.dk) and Inge Sandholt are with Department of Geography and Geology, University of Copenhagen, Oester Voldgade 10, 1350 Copenhagen K. Denmark

F.-M. Göttsche and F. S. Olesen are with Karlsruhe Institute of Technology, Hermann-von-Helmholtz-Platz 1, 76344 Leopoldshafen, Germany

of angular configurations including summer solstice and fall equinox, the model was run with a temporal resolution of 15 minutes (corresponding to the temporal resolution of SEVIRI) for all time steps for which the sun was above the horizon (sun zenith angles below 90 degrees). An analysis of the differences between the LST obtained under the two different viewing geometries is the focus of this paper.

II. Study area

The study area is a test site located north-east of the town of Dahra in northern Senegal in West-Africa and includes two towers for validating satellite products [9], [10]. The towers are equipped with instruments for validating satellite products in the visible, near-infrared, and the thermal domain. The field site is hosted by the Centre de Recherches Zootechniques de Dahra, Institut Sénégalais de Recherches Agricoles (ISRA). Annual mean precipitation is approximately 370mm (1960-2007), but with considerable inter-annual variation. Le Houerou [11] classified the site as being in the Sudano-Sahelian ecoclimatic zone, although by definition this zone is should have mean annual rainfall between 400 mm and 600 mm. The classification is based on older rainfall data; in the mean time (since the seventies) the region has suffered from decreased rainfall as has most of West-Africa. The growing season is relatively short, lasts normally less than 100 days and occurs between July and October. The area around the towers is used as grazing land for the zoological research station, but also as farmland. Additionally, there are some "Gum Arabic" plantations in the immediate surroundings. Trees are relatively sparse and the surface cover is dominated by annual grasses, e.g. *Schoenefeldia gracilis*, *Dactyloctenium aegypticum*, *Aristida mutabilis* and *Cenchrus biflorus* [12], [13]. The soil is sandy and reddish in colour and was classified as an Arenosol by Batjes [14]. The trees are scattered in the landscape, either as isolated trees or as small clumps. In some cases the distribution of the bushes and trees follows ancient dunes, which causes stripes of high vegetation - hence the name "tiger bush". Tree age and size vary widely, and, depending on the species, some trees are actively shaped by both man and animals. During a tree survey in 2008 five different tree species were found [15] of which two were only represented by a single tree. The dominant species in the study area are two Acacia species and *Balanites aegyptiaca*. The *Acacia raddiana* is a sub-species of *Acacia tortilis*, which is typical for the silty/loamy pediplains in the Sudano-Sahelian subzone [11] as is *Acacia Senegal*. Due to the strong natural seasonality of the region, grass is usually desiccated from October to April, whereas the trees are usually green throughout year. During the rainy season the grass grows high (about 1m) and dense and the entire site is covered by vegetation.

Bush fires occur regularly and mainly affect the herbaceous cover, while trees are generally less affected. On October 28th 2008, the area around the towers burned, leaving the surface clear of vegetation and dark in colour, which was still the case during another visit of the site in June 2009: the affected area is clearly visible in fig. 1 as a dark "semi-circle".

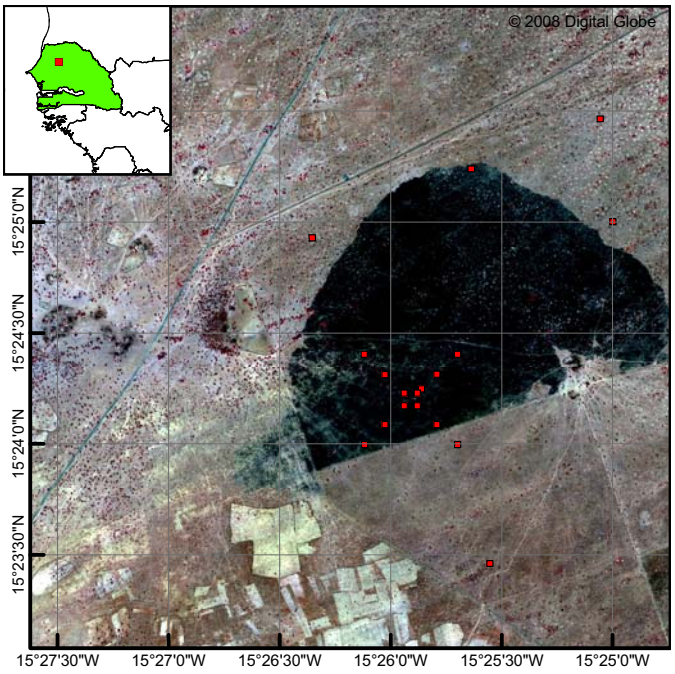

Fig. 1. The location of the study site close to Dahra, Senegal. Also shown is the location of 18 of the 26 surveyed 50x50m plots. The area shown is a subset of the full Quickbird image. The dark area is a fire scar (see the text for further details).

This might influence the comparison between the in situ point measurements and the remotely sensed values to some degree, as only parts of the SEVIRI pixels used were burned.

III. Method and data

A. Model description

The MGP-model applied in this study is based on the Geometric Optics Radiative Transfer (GORT) model [16] originally developed for use in the visible domain. It models the surface as consisting of just four surface components: sunlit and shaded canopy and sunlit and shaded background. "Canopy" refers to canopies of trees as well as tall shrubs/bushes whereas "background" refers to flat soil surfaces with or without low vegetation cover, e.g. grass. Given information on canopy size and structure as well as illumination and viewing geometry, the model estimates the relative abundances (projected fractional cover) of each of the four components of a surface. By assuming the components to be isotropic emitters and reflectors, the model can estimate the directional radiative temperature of the composite surface by [8]:

$$\langle T \rangle = \left[\frac{1}{\langle \varepsilon \rangle} \sum (\varepsilon_k T_k^4 f_k) \right]^{\frac{1}{4}} \quad (1)$$

with $\langle T \rangle$ being the directional composite radiative temperature for a given pixel, T_k the radiative temperature of component k, ε_k the emissivity of component k, f_k is the projected fractional cover of component k and $\langle \varepsilon \rangle$ is the composite emissivity given by:

$$\langle \varepsilon \rangle = \sum \varepsilon_k f_k \quad (2)$$

The ε_k used in eqs. 1 and 2 are broadband emissivities. However, in this paper spectral (narrowband) emissivities are used instead. For this to be valid, we have to assume that the surface components behave like "grey bodies", i.e. have constant (or approximately constant) emissivity in the part of the spectrum from where most of the TIR radiance originates: for vegetation this is generally a reasonable assumption. For more details on the MGP model, interested readers are referred to [1], [3], [8].

B. Component temperatures

The sensor configuration for validating LST at the Dahra site consists of four "KT-15.85 IIP" IR-radiometers (self-calibrating, chopped radiometers, Heitronics GmbH). The KT-15 measure IR radiance between 9.6μm and 11.5μm and express the results as brightness temperatures (BT) with standard deviation 0.25°C plus 0.35% of the difference between target and housing temperature. Three of the KT-15 point towards targets representing different components of the land surface, while the fourth KT-15 measures downwelling longwave radiance from the atmosphere at 53° with relation to zenith and points northwards. The targets observed by the three surface facing KT-15 are a patch of grass / soil, which is sunlit over the entire course of the day, a patch of grass / soil which is shaded during the day with the exception of early morning and late afternoon, and a canopy of a *Acacia raddiana* tree from south west (see fig 2). The 53° zenith angle of the sky-facing sensor yields measurements which are representative for the hemispherical downwelling longwave radiation [17]. Due to the small distance between the radiometers and the surface, atmospheric attenuation of the surface-leaving IR radiation is negligible. However, the measurements of the KT-15 observing the surface contain radiance emitted by the surface (i.e. the target signal) as well as reflected downwelling IR radiance from the atmosphere: this is corrected for using the measurements from the sky-facing sensor. Depending on target emissivity and on downwelling longwave radiance (e.g. a cold clear sky vs. a warm humid atmosphere), the reflected component can cause differences of several degrees Kelvin [18]. All corrections for the reflected component in the measurements are performed at KT-15's centre wavelength of 10.55μm.

In terms of atmospheric correction the situation at Dahra is difficult since the low elevation of about 90 m a.s.l. results in long atmospheric paths and the atmospheric water vapour load varies strongly between the rainy season and the dry season; especially during the warm (about 40 C) and humid (up to 90 % relative humidity) rainy season the atmospheric correction of TIR data is extremely challenging. Furthermore, occasional outbreaks of Sahara dust complicate cloud detection.

In order to provide the MGP model with appropriate input data, the three measured surface temperatures (see fig. 1) are used as follows:

- The sunlit grass / soil patch measurements represent the "sunlit background" component
- The shaded grass / soil patch measurements represent the "shaded background" component. Morning and late afternoon cases are included, even when the patch was not actually shaded: this leads to a slight overestimation of aggregated pixel temperatures at these times.
- The canopy measurements represent the "sunlit canopy" component, even if the actual canopy is not completely sunlit: this leads to a slight underestimation of aggregated pixel temperatures.
- The "shaded canopy" component is set to air temperature at 5 meters height, which is available from a nearby tower (about 100 meters): this generally is a good approximation. Furthermore, it is practically impossible to measure shaded canopy temperatures in situ over a long time period without continuously moving the sensors.

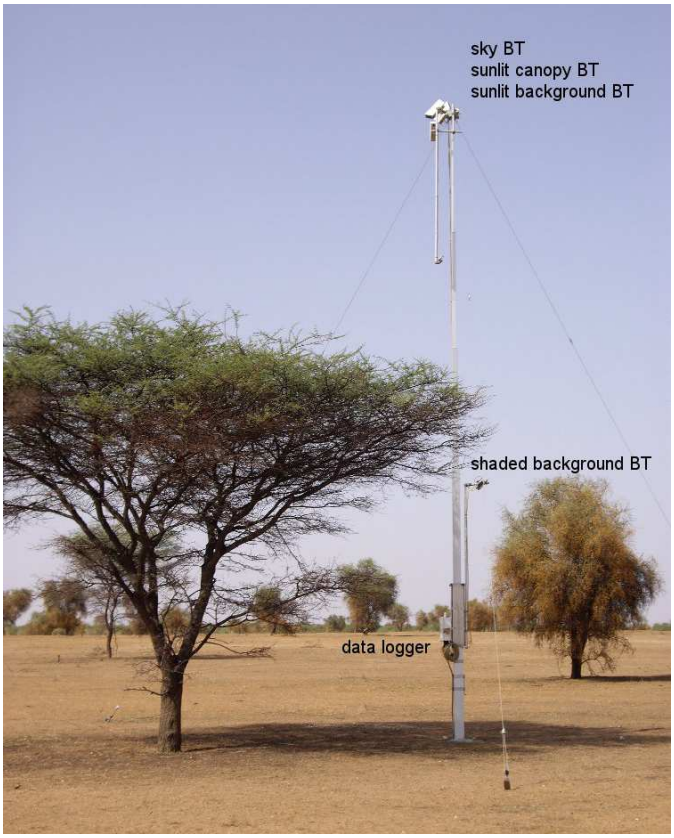

Fig. 2. The four Heitronics KT-15.85 IIP radiometers of the "tree mast" at Dahra validation site measure the brightness temperatures (BT) of the MGP model components "sunlit canopy", "sunlit background", "shaded background", as well as sky BT for correcting the other measurements for reflected longwave radiance.

Fig. 3 shows the diurnal temperature variation of these components for two 7 day periods at the beginning and end of the study period. In June, before the start of the rainy season, the diurnal range of temperatures is large, reaching almost 50°C for the sunlit background component, followed closely by the shaded background component. The canopy components show a considerably lower range of approximately 25°C. In all but a few exceptional cases, the sunlit component temperatures are larger than the corresponding shaded component temperatures. For October, the diurnal range is smaller and the shaded background temperatures are more similar to the canopy component than to the sunlit background component. In some cases the shaded canopy component

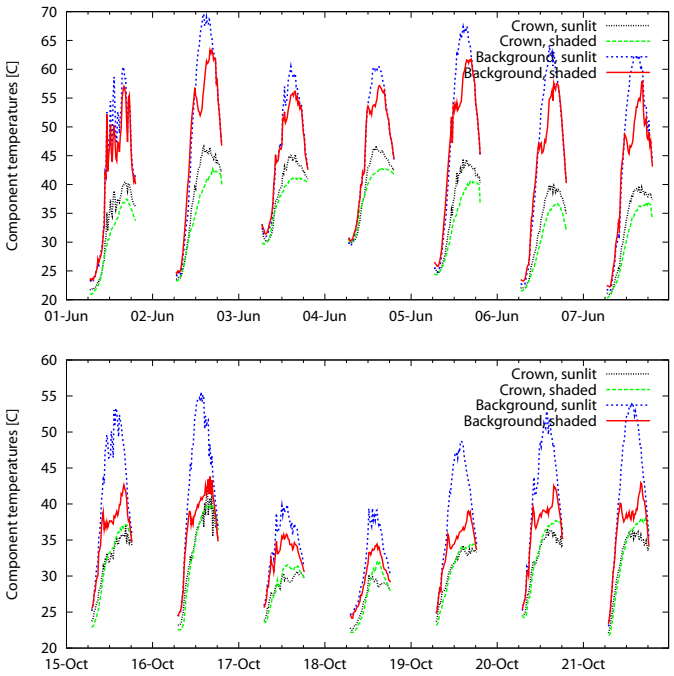

Fig. 3. Two examples of the input component temperatures as measured at Dahra validation site in 2009.

temperatures are higher than the sunlit canopy component temperatures: this indicates that air temperature is not a perfect surrogate for the shaded canopy component. For the study period it is to be expected that the sunlit and shaded canopy component temperatures are almost equal as plenty of moisture is available for the trees to transpire, effectively cooling the canopy to a uniform temperature.

C. Emissivity

The MGP model requires emissivity values for the background and tree components as input. In the case of the field site studied here, the trees (Acacia and Balanites species) stay green throughout the year, but they display some temporal variation in greenness; this is mainly caused by changes in crown density, but also by some species which are out of phase with the rainy season. Therefore, the emissivity of the tree crowns is set to a representative value of 0.98. On the other hand, the emissivity of the background component varies significantly over the year, as the availability of moisture and grass greatly affects the effective emissivity of the land surface. In order to capture this variation, we use the emissivity estimated by the LSA-SAF team from MSG data for their operational LST-product. LSA-SAF emissivities are retrieved for the entire MSG/SEVIRI pixel covering the site and, therefore, also include the tree components. However, we have chosen this emissivity to represent the background component only, since the introduced error is negligible, e.g. for the relatively small tree crown cover (TCC) of 4% at the Dahra site and an emissivity of 0.98 for the tree crown and 0.95 for the background the error is about 0.001. The used emissivities are shown in figure 4: the seasonal change of the background component corresponds largely to the seasonal NDVI-curve for

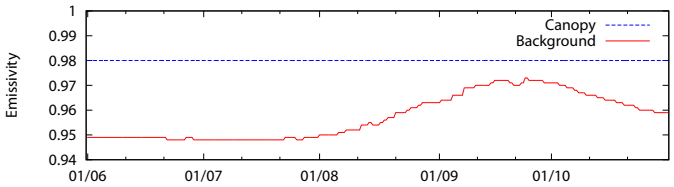

Fig. 4. Emissivity values for the two types of components over the study period, as used for input for the model runs.

the area and reflects the variation of vegetation and moisture in the top soil layer during the rainy season.

D. Emissivity and reflected downwelling longwave radiation

Remote sensing of LST is based on Planck's law, which relates the radiance emitted by a black body (emissivity=1) to its temperature. However, most natural objects are non-black bodies with $0 < \varepsilon_k < 1$, where spectral emissivity ε_k is defined as the ratio between the spectral radiance r_k emitted by surface component k at wavelength λ and the spectral radiance emitted by a black body at the same wavelength and temperature. Therefore, the spectral radiance emitted by a non-black body can be obtained by multiplying Planck's function $B(\lambda, T_k)$ with ε_k:

$$r_k = \varepsilon_k \cdot B(\lambda, T_k) = \varepsilon_k \cdot \frac{c_1 \lambda^{-5}}{\exp\left(c_2/(\lambda T_k)\right) - 1} \qquad (3)$$

where r_k is in $Wm^{-3}sr^{-1}$, constants $c_1 = 1.1910 \cdot 10^{-16} Wm^2 sr^{-1}$ and $c_2 = 1.4388 \cdot 10^{-2} mK$, T_k is the measured component temperature in Kelvin, and λ is in meters.

For a sensor located near the surface and measuring within an atmospheric TIR window, the influence of the atmosphere can be neglected. With known emissivity, the simplified radiative transfer equation [19] can be used to account for reflected downwelling TIR radiance from the atmosphere and for the non-black body behaviour of the surface. Therefore, the blackbody equivalent spectral radiance B_k emitted by component k at temperature T_k and with spectral emissivity ε_k is given by:

$$B_k = \frac{r_k}{\varepsilon_k} = \frac{R_k - (1 - \varepsilon_k) R_{sky}}{\varepsilon_k} \qquad (4)$$

where R_k is the component's *measured* spectral radiance and R_{sky} is sky radiance, which is also measured in this study. Once B_k is known, Planck's law can be solved for the temperature T_k of surface component k (see eq. 3).

E. Vegetation structure data

In order to be able to upscale the radiometric point measurements from the validation station to the size of a meteorological satellite pixel (1-5 km), the relevant land cover components, e.g. trees and bare ground, and their relative cover fractions have to be known. The tree vegetation in the study area was investigated during a field campaign in July 2008 during which 26 plots of 50x50 m^2 were surveyed. All trees within these plots were surveyed and the species, tree height,

TABLE I
RESULTS FROM THE FIELD TREE SURVEY APPLIED IN THIS STUDY

Parameter	Value	Unit
Tree crown cover (TCC)	4	%
Avg. tree height	4.3	m
Avg. crown radius	2.0	m
Avg. crown vertical radius	1.5	m
Effective tree crown LAI (eLAI)	2.0	m^2/m^2

TABLE II
INPUT PARAMETERS USED FOR THE SENSITIVITY RUNS

Parameter	*Original*	*Dense*	*Struct*	*Struct2*
Avg. tree height	4.3	4.3	7.0	5.2
Avg. crown radius	2.0	2.0	2.0	2.5
Avg. crown vertical radius	1.5	1.5	2.5	1.5
Effective tree crown LAI	2.0	5.0	5.0	5.0

diameter at breast height (DBH), crown radius, and crown base height were recorded. Tree crown cover (TCC) is an essential parameter for many remote sensing applications, as it significantly influences surface reflectance and temperature as well as surface anisotropy in the visible and thermal domain. Using the multi-spectral Quickbird scene shown in fig. 1, the field measurements were up-scaled to a larger area. The area was split into different subsets with slightly different densities and tree sizes. Interested readers are referred to [15] for more details on the tree survey. The average TCC for the study area was determined to be about 4 % and is, among others, used here to study the directional dependency of LST, e.g. as obtained from the MSG SEVIRI sensor.

For such low TCC only limited directional effects are to be expected. In order to be able to apply the MGP modelling results to a wider geographical area, we chose to also investigate the sensitivity of the directional effects to TCC and to vegetation structure. This was done by varying TCC in 6 steps up to 35% (4, 8, 12, 18, 25 and 35%) for four different canopy structures, which resulted in a total of 24 model-scenarios. This range of TCC represents a wider neighbourhood of the site, since TCC varies on the local scale, e.g. in soil characteristics and management practises, as well as on the regional scale, e.g. with the increasing precipitation to the south, although less dramatically, as illustrated in fig. 5. Especially when considering small-scale variations, the range of TCC from 4% to 35% is realistic for much of the semi-arid part of the Sahel. In terms of tree and canopy characteristics, we used typical values for the tree-species in the study area. In addition, alternative tree and canopy characteristics (compared to those from tree survey) were simulated: one case with taller trees and vertically elongated canopies, and a second case with lower trees and "flat" horizontally elongated canopies (see table II), which are typical of many savannah tree-species.

IV. RESULTS AND DISCUSSION

Outputs from the model runs consist of component fractional cover and directional aggregated pixel temperature. In this study, we primarily investigate the differences in estimated

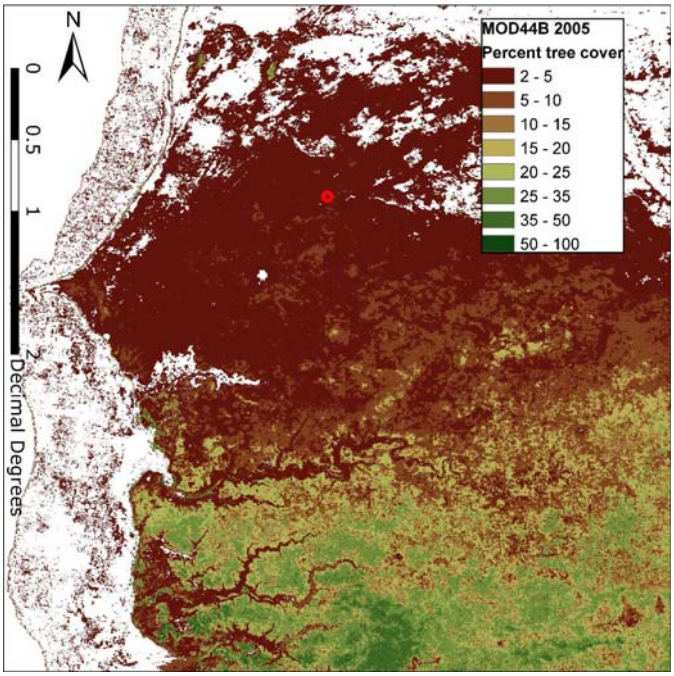

Fig. 5. MODIS Vegetation Continuous Fields product for 2005 for Senegal and surrounding countries with the study site highlighted in red [20].

temperatures, namely between the temperature simulated for the MSG SEVIRI sensor located at 0 degrees East over the Equator and the temperature simulated for nadir viewing geometry. These geometries were chosen to study the influence of illumination and viewing geometry on LST products from geostationary satellite sensors like MSG SEVIRI on a diurnal and seasonal scale.

A. Basic statistics, full time series

The basic statistics for the 24 model simulations are shown in figure 6 which shows the mean, minimum, and maximum temperature difference for all time steps. For all simulations, the average temperature difference is small, reaching just 0.34°C for the "struct"-run with 35% TCC. Introducing such a small error (compared to the "ideal"-case of having nadir measurements) might not seem significant as this is well within the target accuracy of most LST-products. However, the average values presented here, are calculated on a larger range of temperature differences as exemplified by the minimum and maximum values in figure 6. Considering these values, the most extreme range exceeds three degrees and for all but the "struct2" case the ranges exceed two degrees.

The "original" model runs representing the actual conditions at the field site (TCC = 4% and canopy structure according to the survey results) show only small temperature differences for the two viewing geometries. The mean difference is just 0.05°C and the range is about 0.35°C. Therefore, considering the uncertainties in emissivity and the sensitivity of split-window algorithms to atmospheric water vapour, it is unlikely that angular effects of this magnitude can be detected in LST estimates from MSG.

The mean, minimum, and maximum temperature differences for the "original"-model increase with increasing TCC,

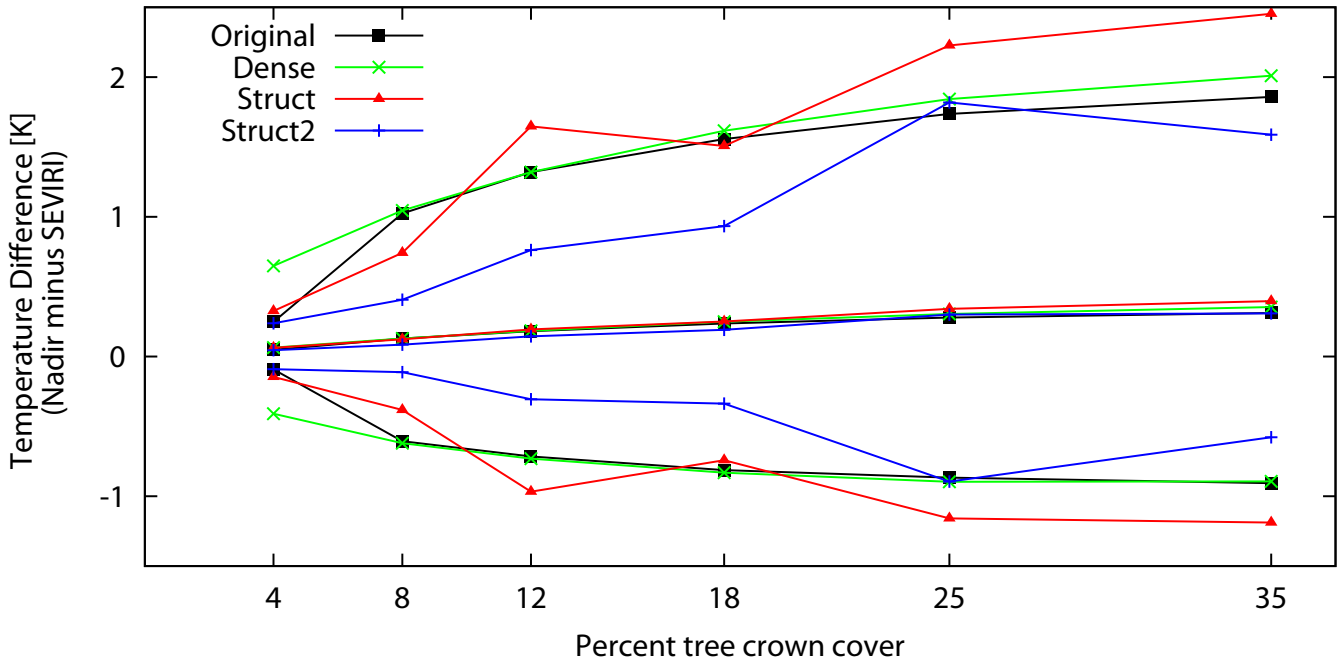

Fig. 6. Overview of mean, minimum and maximum temperature difference as a function of TCC for each of the 24 model runs.

although the rate of increase levels off. This is consistent with findings from a previous study, which showed maximum temperature differences to occur at a TCC of about 35% [3]. The largest increase in temperature range occurs between TCC values of 4% and 8% (about 1.2°C), but the range continues to increase to almost 3°C at TCC = 35%.

In the "Dense"-runs, the density of the tree crowns was increased by increasing the effective Leaf Area Index (eLAI) of the tree crowns from its original value of 2 to a value of 5. In general, the results are very similar to the results of the "original"-run, but with a major difference for the TCC = 4% run: in this case, the minimum and maximum temperature differences are considerably higher for the "Dense"-runs (see fig. 6). This is caused by the higher effective canopy component fractions, as dense tree crowns have fewer within-crown gaps, which effectively sets the canopy component fractions equal to TCC: this is not the case for sparser crowns. For the runs with higher TCC, this effect is negligible and the maximum temperature differences are actually smaller than for the "original"-run.

The "Struct" and "Struct2"-runs represent cases where the size and shape of the trees have been altered (see table II for details). In both cases, the results show a more complex pattern than for the "original" and "dense" runs and the temperature differences do not increase monotonously with TCC. The "struct2"-runs even indicate that the temperature difference starts to decrease for TCC above 25%. For the "struct2"-run, temperature differences are similar or lower than for the other runs with the same values of TCC, while the "struct"-run shows the largest overall temperature differences at 12, 25 and 35% TCC.

Overall, it is apparent that the directional dependency of the LST is sensitive to TCC, tree size and shape as well as eLAI. For eLAI, the current study indicates that the sensitivity is largest at low TCC, while tree size and shape influence the temperature differences over the entire range of TCC. For the range of TCC used in this study, the temperature differences increase with increasing TCC in most cases.

On their own, the mean, minimum, and maximum temperature differences discussed above do not say much about the implications for using a time series of LST estimates in a SVAT-model, e.g. for modelling the diurnal heat exchanges between the surface and the atmosphere. Using the four canopy models from table II and varying TCC in 6 steps resulted in 24 simulations: table III shows for how many percent of the time-steps the temperature difference exceeded 0.5°C and 1.0°C, respectively.

For all runs with TCC = 4% less than 1% exceed temperatures differences of 0.5°C; in fact, only for the "dense"-run any time steps at all show a difference of 0.5°C. When increasing TCC to 8%, up to 5% of the time steps show temperature differences of more than 0.5°C. For higher TCC, more than 20% of the time steps show more than 0.5°C temperature differences and in the case of the "struct"-run with TCC = 35% more than 10% of the time steps exceed a temperature difference of 1.0°C. This clearly demonstrates that even if the *average* temperature differences are negligible, the temperature difference at a specific time step can still be significant.

B. Diurnal analysis

The temperature differences between the two viewing geometries discussed here (nadir and SEVIRI) vary seasonally and diurnally with the position of the sun. Fig. 7 shows an example of the temperature differences for all time steps for the "struct" model with TCC = 18%. Until September the temperature differences are almost consistently positive (i.e. nadir-geometry exhibits the higher temperatures), while

TABLE III
PERCENT OF TIME STEPS WITH A TEMPERATURE DIFFERENCE OF MORE THAN 0.5 AND 1.0 K FOR EACH OF THE 24 MODEL RUNS.

	Original						*Dense*						*Struct*						*Struct2*					
	4	8	12	18	25	35	4	8	12	18	25	35	4	8	12	18	25	35	4	8	12	18	25	35
More than 0.5 K	0	5	10	15	19	22	0	5	10	17	21	26	0	2	11	17	25	29	0	0	3	9	21	22
More than 1.0 K	0	0	1	3	4	6	0	0	1	3	5	8	0	0	2	3	8	11	0	0	0	0	5	4

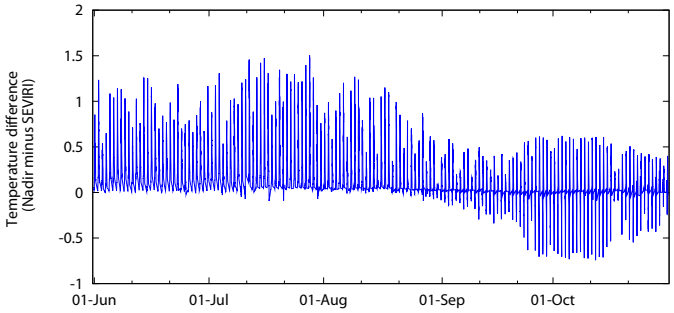

Fig. 7. The temperature difference for all time steps for the "struct", tcc = 18% run.

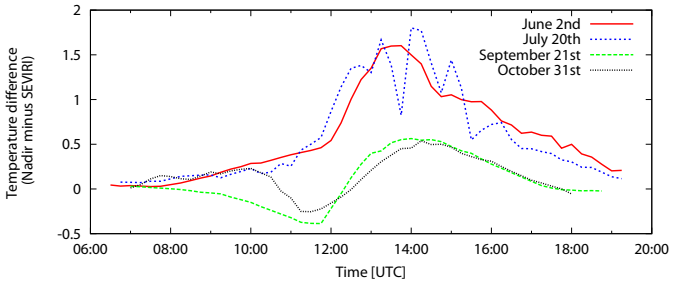

Fig. 8. Four examples of the diurnal variation in the temperature difference between nadir and SEVIRI geometry, all from the "Dense", TCC = 35%-run. Note that time is given as UTC, and that local solar noon is approximately 13:00 UTC +/- 15 min depending on season.

temperature differences are almost symmetrically distributed around 0°C from September to the end of the study period. Furthermore, it is apparent that the temperature differences vary considerably from one day to the next. As the illumination geometry changes only slowly, this is mainly attributed to variations in component temperatures caused by clouds and/or precipitation, since the radiometers also measure underneath of clouds. In addition to the seasonal variations in the sign of the temperature difference, the shape of the diurnal difference also changes (see fig. 8). The June and July curves are similar, but the September and October cases show negative temperature differences between 11:00 and 12:00 UTC. The September case shows the largest negative temperature difference just before 12:00 UTC, which indicates that for SEVIRI viewing geometry the temperatures are higher than for nadir-geometry. This is caused by a hot-spot effect which occurs when the sun is located right behind the sensor (23rd of September is fall equinox and the sun is located over the Equator): this causes the SEVIRI-sensor to observe mostly "sunlit"-parts of both components, the canopy and the background, which have higher component temperatures than the "shaded" parts. At the same time a sensor with nadir-geometry observes

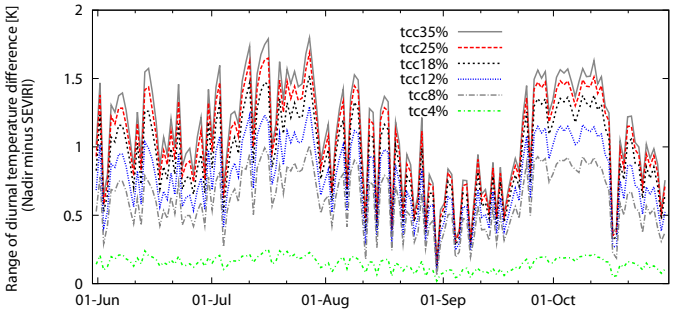

Fig. 10. The diurnal range of the temperature difference between nadir and SEVIRI geometry for all of the "original"-runs. The range is calculated as the difference between the minimum and maximum temperature difference occurring within a day.

more "shaded" parts and, thus, measures a lower aggregated temperature for the same area. In October the same effect is observed, although smaller and only near 12:00 UTC, which is not solar noon but when the sun is close to the sensor at 0 degrees longitude. For the July and October cases, which are on opposite sides of the fall Equinox, the diurnal variations are very different due to the different positions of the sun with relation to the site: during the summer months, the sun passes north of the site, whereas it passes considerably further south during the rest of the year. In the summer, the geometry of the Sun is close to nadir-geometry and, therefore, a strong hot-spot is observed; during the rest of the year the Sun geometry is closer to SEVIRI-geometry. This is the controlling factor for the level of the curve in fig 7.

Although the temperature offset varies with season, here the amplitude of the daily variations does not seem to change significantly. Fig. 9 shows examples of the diurnal range of temperature differences for three of the model runs. The curves represent the maximum difference between the minimum and maximum temperature differences occurring at any given day and can be interpreted as the "error" one would make when using SEVIRI-based LST estimates during a day compared to the reference case of nadir-observation. Note that the values in fig. 9 (and in fig. 10) are daily values, whereas full 15-min. resolution data are shown in fig. 8.

The three time series shown in fig. 9 show a high degree of correlation (r^2>0.95), indicating that the timing of the temperature differences is mainly controlled by component fractional cover (depends on sun geometry) and canopy structure. On the other hand, the amplitude of the differences is controlled by the differences between the input component temperatures.

Fig. 10 shows the diurnal range in temperature differences, for the "original"-runs with the six different TCC-densities. It is obvious that the density in this case controls the range of

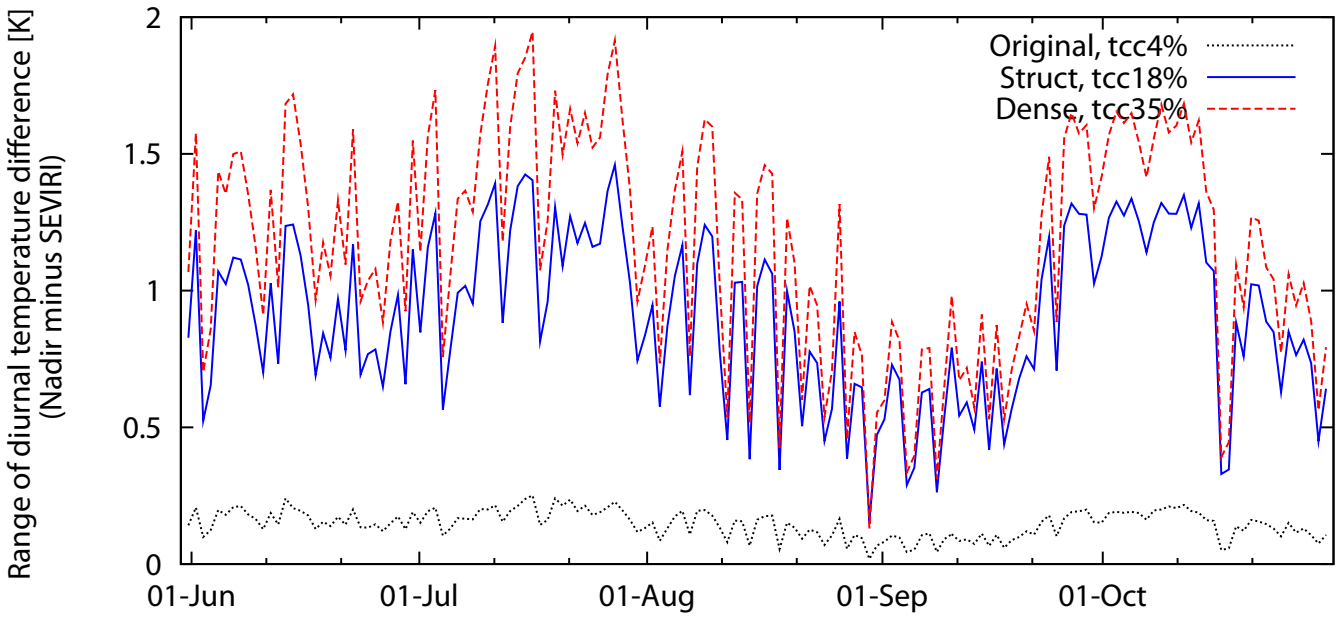

Fig. 9. Three examples of the diurnal range of the temperature difference between nadir and SEVIRI geometry. The range is calculated as the difference between the minimum and maximum temperature difference occurring within a day.

temperature difference, but the influence of TCC diminishes as it increases. Furthermore, the correlations between the different runs are almost perfect, which should be expected as neither the structural parameters nor the geometry changed.

The implications of the diurnal and seasonal variations of the temperature differences shown above can be severe when using LST estimates from a sensor like the SEVIRI-sensor at full temporal resolution. Not only does one introduce angle-dependent temperature differences of up to 2°C during a day, but also the timing of the differences changes with time of day and season. This might severely influence performance of e.g. SVAT models or Surface energy budget models which often use LST data for assimilation or calibration [21]–[23].

C. Comparison with LSA-SAF LST product

We compared the model results to the LSA-SAF LST product, which is generated at 3 kilometres spatial resolution (actual FOV of MSG / SEVIRI is 4.8 km). Instead of comparing the in situ data with data for the MSG / SEVIRI pixel containing the measurement site, we choose a pixel slightly to the north east. This was motivated by the fact that this pixel represents the surface around the site better than the actually co-located pixel, which is covered by a mixture of agriculture, an Acacia plantation, and tiger bush. We compared remote sensing based LSA-SAF LST with composite LST from the MGP model (with vegetation structure and cover from tree survey) and with LST determined from the in-situ brightness temperatures over the ”sunlit background” component. As the TCC is very low (4%), the results for the MGP and for the ”sunlit background” were nearly identical; therefore, only the MGP-results are discussed below. Due to the low TCC, it is unlikely that the directional effects can be identified in the data, as the diurnal range in the temperature difference is on the order of 0.2 K (as shown in fig. 9 and fig. 10).

Analysis showed that for most of the study period, LSA-SAF LST and MGP-LST match poorly. Correlation-analysis of all available matches for the entire period gave a coefficient of determination r^2 of just 0.67. The discrepancies between the two data sets extend over most of the study period and are thought to be mainly caused by undetected clouds in the MSG / SEVIRI data and by inaccurate atmospheric corrections. Only the last 3 weeks of the study period yield significantly better results (see fig. 11A) both in terms of the coefficient of determination (r^2 of 0.928) and in successfully matching the daily LST cycles. However, even during these 3 weeks cloud contamination is readily identified, e.g. in fig. 11C on October 13th, 14th and 15th. When additionally removing those days from fig. 11A, which are obviously contaminated by (sub-pixel) clouds, the r^2 value is improved to 0.975 (see fig. 11B).

A warm and very moist atmosphere over a semi-arid area during the rainy-season is a challenge for any LST algorithm and the LSA-SAF LST algorithm does not seem to be an exception. A smaller part of the discrepancies could also be caused by the scale mismatch between the in-situ measurements (FOV of about 5 m^2) and the MSG / SEVIRI measurements, which represent the integrated signal of about 25 km^2 each (ignoring distortions due to off-nadir geometry and georeferencing errors). However, for the 11^{th} - 31^{st} of October the LST from the MGP model (and the LST obtained directly from the in-situ measurements) match the corresponding LST from LSA-SAF well: therefore, it is unlikely that the difference in spatial scales caused the low correlation observed before. It is beyond the scope of this study to validate the LSA-SAF LST product, but a comparison with in situ data from Dahra and MODIS data will be the subject of a separate publication.

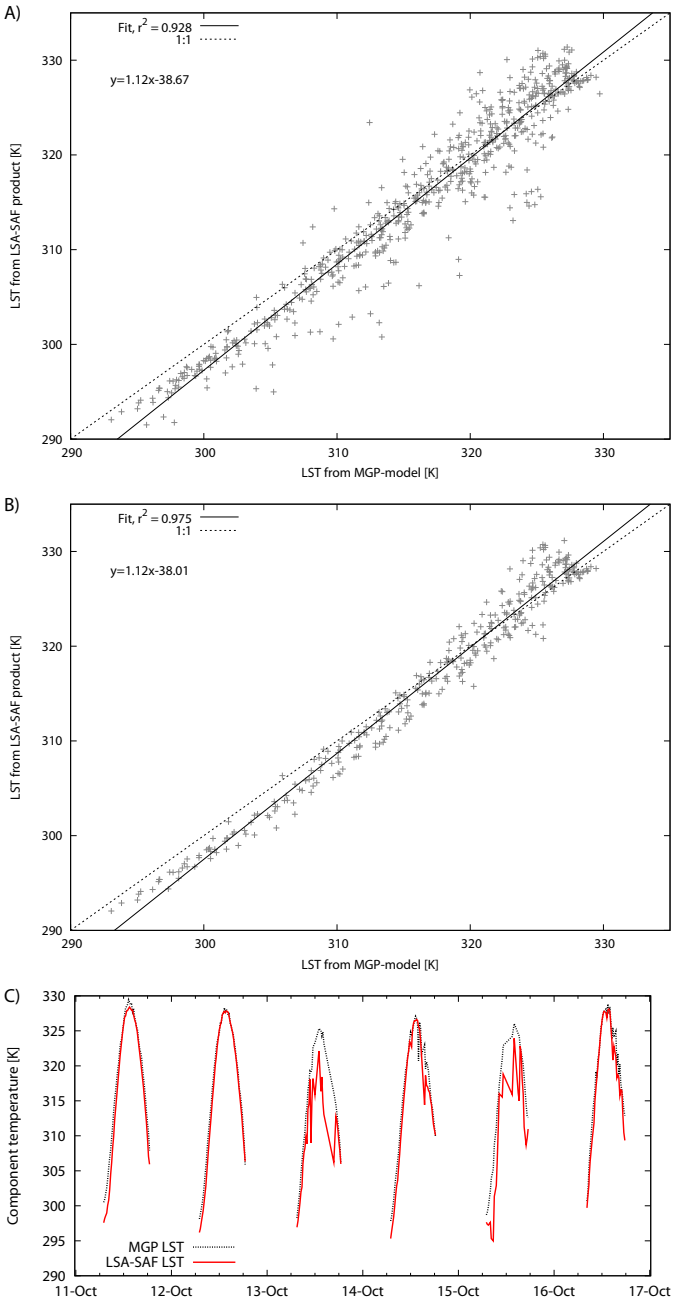

Fig. 11. A: scatterplot of LSA-SAF LST for a pixel representative of the field site against the modeled MGP LST, for the period between October 11th and October 31st. B: Same as A, but excluding days obviously affected by undetected clouds. C: An example of the diurnal variation in the LSA-SAF LST and MGP LST for six days in October.

V. Conclusions and Outlook

This study has shown that even if the mean error due to directional effects is negligible, the directional errors at individual time steps can still be significant on both the diurnal and the seasonal scale. Over the considered range of tree crown covers (TCC), the magnitude of the directional effects increases nearly uniformly with increasing TCC. Canopy shape, structure and density also influence the temperature difference, but in a lesser and more complex way than TCC.

For the angular configurations studied here, a diurnal range in temperature differences of approximately two degrees is common; furthermore, the absolute values of the temperature difference vary with the seasons. The highest composite temperatures were consistently found for the viewing geometry closest to the illumination geometry, as this viewing geometry "sees" higher fractions of the "sunlit" components (hot spot effect). For a study area in West Africa and north of the Equator, in summer this causes LST retrieved for nadir-geometry to be higher than LST retrieved for SEVIRI-geometry, and vice versa in winter. This also influences the diurnal variation of the temperature differences, which show distinctly different patterns at different times of the year.

Due to the sparse TCC in the area (about 4%) it is unlikely that it will be possible to separate directional effects on LST from other sources of uncertainty for the Dahra test site. However, the MGP model results show that already at a TCC of 8% the temperature difference due to directional effects can be up to 2°C; given LST uncertainties as specified by the LSA-SAF "errorbar_LST" product layer this would be sufficient to identify these effects in SEVIRI based LST estimates.

The comparison between the LSA-SAF LST products and the MGP-modeled LST showed large discrepancies for most of the study period, which mainly covered the - from an optical remote sensing point of view - highly challenging rainy season. The results indicate that the LSA-SAF algorithm could not fully account for the extremely moist and warm atmosphere at Dahra during this time. In contrast, during the last three weeks of October 2009 (i.e. after the rainy season) model LST and LSA-SAF LST generally agreed well with each other, but LSA-SAF LST continued to suffer from undetected (sub-pixel) clouds.

The model results presented here are thought to be representative of large areas across the Sahel region where the vegetation structure is similar and TCC is sparse to moderate. Therefore, for this type of area great care should be taken when LST products obtained from satellite sensors with high temporal resolution (usually in geostationary orbit) are used as input to hydrological or SVAT-models. In this context it should be noted that the current uncertainty estimates of operational LST products do not include this source of error.

Acknowledgment

This work contributes to the AMMA Project (http://www.amma-international.org). Based on a French initiative, AMMA was built by an international scientific group and is currently funded by a number of agencies, especially from France, UK, US and Africa. It has been the beneficiary of a major financial contribution from the European Community's Sixth Framework Research Program. The study was also partly funded by The International Research School in Water Resources (FIVA) at the University of Copenhagen, Denmark. LSA-SAF, a project of the European Organization for the Exploitation of Meteorological Satellites (EUMETSAT), partially funds the validation of LST and provided LST and emissivity products (landsaf.meteo.pt). Thanks for Ana Pinheiro and Jeffrey Privette, NOAA NCDC, Asheville, for providing the MGP-code and for invaluable

help. Thanks also to Department of Geography, University of Maryland and NASA for providing the MOD44B product. The source of this data set was the Global Land Cover Facility, www.landcover.org.

REFERENCES

[1] A. C. Pinheiro, J. L. Privette, R. Mahoney, and C. J. Tucker, "Directional effects in a daily AVHRR land surface temperature dataset over Africa," *IEEE Transactions on Geoscience and Remote Sensing*, vol. 42, no. 9, pp. 1941–1954, 2004.

[2] J. Schmetz, P. Pili, S. Tjemkes, D. Just, J. Kerkmann, S. Rota, and A. Ratier, "An Introduction to Meteosat Second Generation (MSG)," *Bulletin of the American Meteorological Society*, vol. 83, pp. 977–992, 2002.

[3] M. O. Rasmussen, A. C. Pinheiro, S. R. Proud, and I. Sandholt, "Modeling Angular Dependences in Land Surface Temperatures From the SEVIRI Instrument Onboard the Geostationary Meteosat Second Generation Satellites," *Transactions on Geoscience and Remote Sensing, IEEE*, 2010.

[4] I. Trigo, C. Madeira, I. Monteiro, S. Coelho, C. Barroso, F.-S. Olesen, F.-M. Göttsche, and L. Peres, "Product User Manual, Land Surface Temperature," EumetSat Land SAF, Tech. Rep., 2008, version 2.2.

[5] Z. Wan and J. Dozier, "A generalized split-window algorithm for retrieving land-surface temperature from space," *Geoscience and Remote Sensing, IEEE Transactions on*, vol. 34, no. 4, pp. 892–905, Jul 1996.

[6] S. C. Freitas, I. F. Trigo, J. M. Bioucas-Dias, and F.-M. Göttsche, "Quantifying the Uncertainty of Land Surface Temperature Retrievals From SEVIRI/Meteosat," *IEEE Transactions on Geoscience and Remote Sensing*, vol. 48, no. 1, pp. 523–534, 2010.

[7] G. C. Hulley and S. J. Hook, "Intercomparison of versions 4, 4.1 and 5 of the MODIS Land Surface Temperature and Emissivity products and validation with laboratory measurements of sand samples from the Namib desert, Namibia," *Remote Sensing of Environment*, vol. 113, no. 6, pp. 1313 – 1318, 2009.

[8] A. C. Pinheiro, J. L. Privette, and P. Guillevic, "Modeling the observed angular anisotropy of land surface temperature in a Savanna," *IEEE Transactions on Geoscience and Remote Sensing*, vol. 44, no. 4, pp. 1036–1047, 2006.

[9] S. Stisen, I. Sandholt, A. Noergaard, R. Fensholt, and K. H. Jensen, "Combining the triangle method with thermal inertia to estimate regional evapotranspiration – applied to msg-seviri data in the senegal river basin," *Remote Sensing of Environment*, vol. 112, no. 3, pp. 1242 – 1255, 2008.

[10] R. Fensholt and I. Sandholt, "Evaluation of MODIS and NOAA AVHRR vegetation indices with in situ measurements in a semi-arid environment," *International Journal of Remote Sensing*, vol. 26, no. 12, pp. 2561–2594, 2005.

[11] H. N. Le Houerou, *The grazing land ecosystems of the African Sahel*. Springer-Verlag, Berlin, New York, 1989.

[12] R. Fensholt, I. Sandholt, and S. Stisen, "Evaluating MODIS, MERIS, and VEGETATION vegetation indices using in situ measurements in a semiarid environment," *Geoscience and Remote Sensing, IEEE Transactions on*, vol. 44, no. 7, pp. 1774–1786, July 2006.

[13] B. Elberling, R. Fensholt, L. Larsen, A.-I. Petersen, and I. Sandholt, "Water content and land use history controlling soil CO_2 respiration and carbon stock in savanna soil and groundnut fields in semi-arid Senegal," *Geografisk Tidsskrift - Danish Journal of Geography*, vol. 103, pp. 47–56, 2003.

[14] N. H. Batjes, "Options for increasing carbon sequestration in West African soils: an exploratory study with special focus on Senegal," *Land Degradation & Development*, vol. 12, no. 2, pp. 131–142, 2001.

[15] M. O. Rasmussen, F.-M. Göttsche, D. Diop, C. Mbow, F.-S. Olesen, R. Fensholt, and I. Sandholt, "Tree survey and allometric models for tiger bush in northern Senegal and comparison with tree parameters derived from high resolution satellite data," *International Journal of Applied Earth Observation and Geoinformation*, 2010.

[16] X. Li and A. Strahler, "Geometric-optical bidirectional reflectance modeling of the discrete crown vegetation canopy: effect of crown shape and mutual shadowing," *IEEE Transactions on Geoscience and Remote Sensing*, vol. 30, no. 2, pp. 276–292, 1992.

[17] K. Y. Kondratyev, *Radiation in the atmosphere*. Academic Press, New York, 1969.

[18] S. Schädlich, F.-M. Göttsche, and F.-S. Olesen, "Influence of land surface parameters and atmosphere on meteosat brightness temperatures and generation of land surface temperature maps by temporally and spatially interpolating atmospheric correction," *Remote Sensing of Environment*, vol. 75, no. 1, pp. 39 – 46, 2001.

[19] P. Dash, F.-M. Göttsche, F.-S. Olesen, and H. Fischer, "Land surface temperature and emissivity estimation from passive sensor data: theory and practice-current trends," *International Journal of Remote Sensing*, vol. 23, pp. 2563–2594, 2002.

[20] M. Hansen, R. DeFries, J. Townshend, M. Carroll, C. Dimiceli, and R. Sohlberg, "Vegetation Continuous Fields MOD44B, 2001 Percent Tree Cover, Collection 3, University of Maryland, College Park, Maryland," 2003. [Online]. Available: http://glcf.umiacs.umd.edu/data/vcf/

[21] B. Coudert, C. Ottle, B. Boudevillain, J. Demarty, and P. Guillevic, "Contribution of thermal infrared remote sensing data in multiobjective calibration of a dual-source svat model," *Journal of Hydrometeorology*, vol. 7, no. 3, pp. 404–420, 2006.

[22] B. Coudert, C. Ottle, and X. Briottet, "Monitoring land surface processes with thermal infrared data: Calibration of svat parameters based on the optimisation of diurnal surface temperature cycling features," *Remote Sensing of Environment*, vol. 112, no. 3, pp. 872 – 887, 2008.

[23] L. Campo, F. Castelli, D. Entekhabi, and F. Caparrini, "Land-atmosphere interactions in an high resolution atmospheric simulation coupled with a surface data assimilation scheme," *Natural Hazards and Earth System Science*, vol. 9, pp. 1613–1624, 2009.

Mads Olander Rasmussen received the B.S. in Geoinformatics from University of Copenhagen, Denmark, in 2002, the M.S. degree in Remote Sensing from University of London in 2004 and the M.S. degree in Geography from University of Copenhagen, Denmark, in 2005.

He is currently pursuing the Ph.D. degree in Geography at the University of Copenhagen, Denmark. His main research interests are medium and coarse resolution remote sensing of surface properties in both the visible and thermal domain, with a regional focus on Africa. He has been a Visiting Research Scholar at the NOAA National Climatic Data Center, and has also been working as a Remote Sensing Consultant for GRAS A/S.

Frank-M. Göttsche received his M.Sc. degree in Physics (1993) and his Ph.D. degree in Geophysics (1997) from the Christian-Albrechts University, Kiel, Germany. From 1996 to 1997 he was with the Institute of Geophysics, Uppsala University, Sweden.

In 1997 he joined the Institute of Meteorology and Climate Research, Forschungszentrum Karlsruhe, Germany, where his main areas of research were the retrieval of land surface temperature from satellite data with methods from artificial intelligence and the modeling of the diurnal temperature cycle. From 2003 to 2007, he was Assistant Professor at the Physics Department of the United Arab Emirates University, UAE, and served as scientific consultant to the Satellite Application Facility on Land Surface Analysis (LSA-SAF). Since 2007 he is project scientist at Karlsruhe Institute of Technology (KIT), Germany, where he is in charge of permanent ground truth stations in Europe and Africa operated for LSA-SAF.

Folke-Sören Olesen was born the 30.06.1956 in Kiel (Germany). He received his M.Sc. degree in Meteorology in 1984 from the Christian-Albrechts University, Kiel, Germany. The topic of his masters-thesis was cloud detection with NOAA-AVHRR data; additionally, he took computer sciences for 3 years as a minor.

From 1984 to 1987 he worked as junior scientist at DFVLR (Germany, today DLR) in the operational satellite receiving branch where he was responsible for IR vertical sounding. In 1987 he became head of a research group at the Institute for Meteorology and Climate Research in the Kernforschungszentrum Karlsruhe, Germany, which in 2009 became Karlsruhe Institute of Technology (KIT). The focus of the group is the development, improvement and application of algorithms for cloud detection and classification, for determination of land surface parameters and for IR vertical sounding. Since 1999 the group is the responsible member for LST evaluation and validation in the LSA-SAF (EUMETSAT). Four permanent ground stations for satellite data validation are currently operated in Europe and Africa by him and his group.

Inge Sandholt Inge Sandholt (M'02) received the M.S degree in physical geography from the University of Copenhagen, Denmark (1990) and the Ph.D. degree in statistics from the Royal Veterinary and Agricultural University, Frederiksberg, Denmark (1996).

She is currently an Associate Professor at the Institute of Geography, University of Copenhagen. She has been a Visiting Scholar at Toronto University (1995) and at Boston University (2007-2008) Her research interests are primarily remote sensing of land surface processes in particular assessment of large scale evapotranspiration and soil moisture, large-scale distributed hydrological modeling, and vegetation modeling. She has a keen interest in multidisciplinary approaches to assessment of climate change impacts in Africa including the human dimension.

Paper III

Tree survey and allometric models for Tiger Bush in Northern Senegal and comparison with tree parameters derived from high resolution satellite data

Authors:

Mads Olander Rasmussen, Frank-M. Göttsche, Doudou Diop, Cheikh Mbow, Folke-S. Olesen, Rasmus Fensholt and Inge Sandholt

Status:

Submitted to International Journal of Applied Earth Observation and Geoinformation, March 31st 2010. Accepted with revisions.

Tree survey and allometric models for tiger bush in northern Senegal and comparison with tree parameters derived from high resolution satellite data

Mads Olander Rasmussen[a,*], Frank-M. Göttsche[b], Doudou Diop[c], Cheikh Mbow[c], Folke-S. Olesen[b], Rasmus Fensholt[a], Inge Sandholt[a]

[a]*Department of Geography and Geology, University of Copenhagen, Oester Voldgade 10, DK-1350 Copenhagen K. Denmark*
[b]*Karlsruhe Institute of Technology. Hermann-von-Helmholtz-Platz 1, 76344 Eggenstein-Leopoldshafen, Germany*
[c]*Université Cheikh Anta Diop, Faculteé des Sciences et Techniques, Institut des Sciences de l'Environnement, BP 5005 Dakar, Sénégal*

Abstract

A tree survey and an analysis of high resolution satellite data were performed to characterise the woody vegetation within a 10x10 km2 area around a site located close to the town of Dahra in the semi-arid northern part of Senegal. Among the surveyed parameters were tree type, height, tree crown radius, and diameter at breast height (DBH), for which allometric models were determined. An object-based classification method was used to determine tree crown cover (TCC) from Quickbird data. The average TCC from the tree survey and the respective TCC from remote sensing were both about 3.0%. For areas beyond the surveyed areas TCC varied between 3.0% and 4.5%. Furthermore, an empirical correction factor for tree clumping was obtained, which considerably improved the estimated number of trees and the estimated average tree crown area and radius. An allometric model linking TCC to tree stem crosssectional area (CSA) was developed, which allows to estimate tree biomass from remote sensing. The allometric models for the three main tree species found performed well and had r^2-values of about 0.7 to 0.8. When estimating tree parameters from Quickbird data alone, the allometric models for tree height and crown radius generally yielded the best results.

Keywords: tree inventory, field survey, tree clumping, image analysis, allometric models, remote sensing

1. Introduction

Estimating tree cover from high resolution remote sensing data is a well established technique and has been employed in numerous studies. However, historically most often aerial photography was used to estimate stand parameters like tree size, stand density and, ultimately, stand biomass for forestry management applications. With the launch of very high resolution commercial satellites like Ikonos and Quickbird, it is now possible to perform similar studies with spaceborne sensors. Unlike sensors typically used for aerial surveys, these sensors have multispectral capabilities and include spectral bands in the visible and the near-infrared part of the spectrum.

In this study we estimate the tree crown cover, tree count and other tree parameters for a Quickbird scene covering an area close to the town of Dahra in semi-arid northern Senegal, West Africa. At first glance tree inventory analyses in areas like the one studied here appear to be of limited use, as tree resources are limited and the potential for economic exploitation is small. However, potentially relevant applications are long term change studies and the estimation of carbon stocks contained in the woody vegetation. The feasibility for increasing carbon storage in natural vegetation for areas with slightly more rain (approximately 600mm/year) has already been demonstrated by, among others, Toure et al. (2003). The combination of field studies of tree parameters like height, trunk diameter, and biomass content (both above and below ground) with remote sensing based estimation of tree cover allows large scale inventories of both, current and future carbon stocks. However, the immediate motivation for this study is to characterise a wider area around a test site, which consists of two towers with instruments used for validating remote sensing products. Tree crown cover is an essential parameter in many applications of remote sensing data, as it significantly influences surface reflectance and temperature as well as surface anisotropy in the visible and in the thermal domain. It is planned to utilise tree crown cover and other tree parameters in a separate study of angular dependency of land surface temperature, e.g. as obtained from the Spinning Enhanced Visible and InfraRed Imager (SEVIRI) onboard Meteosat Second Generation (MSG) satellites. In order to upscale radiometric point measurements performed at the station to the size of meteorological satellite pixels (1-5 km), the relevant land cover components, e.g. trees and bare ground, and their relative cover fractions have to be known.

A wide range of methods for tree delineation and thus tree crown cover estimation exist, ranging from traditional classification methods, over texture analysis to object-based

*Corresponding author
Email address: mor@geo.ku.dk (Mads Olander Rasmussen)

image analysis, which works on pixel clusters instead of individual pixels. Despite of an abundance of available methods, only few studies have addressed areas with sparse tree cover and with trees covering a wide range of sizes and ages; in fact, most studies have been on forests and plantations.

Bai et al. (2005) used black and white, 0.5 meter resolution aerial photographs for estimating the tree encroachment on grasslands in British Columbia, Canada. They used a maximum likelihood classification to distinguish between grasslands and forests, the latter being split into tree crowns and tree shadows. This distinction was made to identify the transition zone between tree crowns and the grasslands. They compared the retrieved tree crown cover estimates with ground measurements and found a good overall agreement, with a slight tendency for underestimation of tree cover from image analysis at most densities, with dense tree cover being the exception. Also applying a classification based method, Hansen et al. (2002) used IKONOS 1 and 4 meter resolution data to estimate tree crown cover for a number of test areas in Zambia. They used texture maps, NDVI, and the raw multispectral channels to classify the images into "crown" and "not crown". They compared this to field measurements and reached r-squared values of 0.867. The results was upscaled to ETM+ and MODIS scale using a relation between NDVI and crown cover for the validation of the MODIS Vegetation Continuous Fields (VCF) product.

In order to identify individual trees or tree clusters, Leckie et al. (2003) segmented individual tree crowns using a spectral valley-tracing algorithm effectively treating the digital numbers (DN) as a height map. Subsequently they classified the individual crown/cluster objects according to species based on 0.6 meter resolution multispectral airborne CASI-sensor data. The valley-tracing method relies on the contrast between the tree crowns and the gaps between canopies appearing bright and dark respectively, in order to identify the gaps between the crowns. In cases where the trees are clumped together, the trees can not be separated using such an approach as the dark gaps are absent. Hirata et al. (2009) used a similar approach developed for the delineation of watersheds. Using an inverted panchromatic band from Quickbird scenes, crowns and crown tops appear as depressions like in a digital elevation model, allowing for the delineation of crowns as if they were watersheds. Another approach which is frequently applied, is the identification of crown centres by finding local maxima in spectral bands sensitive to vegetation (Culvenor, 2002). The crowns are then expanded from the centre points by expanding the area, either by specifying a threshold value or by a maximum allowed step pixel value. A third commonly applied technique is matching templates of trees with identified tree objects (Larsen and Rudemo, 1998). This requires a priori knowledge about tree structure and size, and also assumes that trees are not clumped.

An alternative, geo-statistically based method for tree crown estimation was proposed by Song and Woodcock (2003), who used semi-variograms of images at different spatial resolutions to identify tree crown size. They tested the method on synthetic data as well as on Ikonos data and found that the quality of the results depend largely on the ratio between image resolution and tree crown size, with the best results achieved for ratios close to unity.

The use of allometric models for forest inventories has a long history, but they are most commonly applied to mono-cultural commercial stands to estimate yields. Despite the broad application of these models, a wide range of different functions is used to model the relation between the parameters, which included trunk diameter at breast height (DBH), tree height, crown radius and crown area. Zhang (1997) discussed the use six different functions for allometric models of DBH-tree height relationships. They found that the functions perform almost equally well in terms of r^2-values, but the main differences occurred in terms of the "saturation"-point for tree height. The saturation point is defined as the maximum tree height, which in terms of the mathematical function is the asymptote of the function. They concluded that the selection of the model should be based more on the predictive capabilities and robustness of the model rather than on its performance in terms of high r^2-values or root mean square error.

The rest of the paper is structured as follows: in the next two sections descriptions of the study site and of the used methods and data are given. Then results from a field survey, a manual and an automatic tree analysis, and from allometric models are discussed. Finally, the results are briefly summarized and some conlusions are drawn.

2. Study area

The study area is a test site located north-east of the town of Dahra in northern Senegal in West-Africa and includes towers equipped with instruments for validating satellite products (Stisen et al., 2008; Fensholt and Sandholt, 2005). The field site is hosted by the Centre de Recherches Zootechniques de Dahra, Institut Sénégalais de Recherches Agricoles (ISRA).

Annual mean precipitation is approximately 370mm (1960-2007), but with considerable inter-annual variation. The site is classified by Le Houerou (1989) as being in the Sudano-Sahelian ecoclimatic zone, although this zone is defined as having mean annual rainfall between 400 mm and 600 mm. The classification is based on older rainfall data; in the mean time (since the seventies) the region has suffered from decreased rainfall as has most of West-Africa. The growing season is relatively short, lasts approximately 100 days and occurs between July and October.

The areas around the towers are used as grazing land for the zoological research station, but also as farmland. Additionally, rubber plantations are present in the immediate surroundings. Trees are relatively sparse and the surface cover is dominated by annual grasses (e.g. Schoenefel-

dia gracilis, Digitalia gayana, Dactyloctenium aegupticum, Aristida mutabilis and Cenchrus bifloures) (Fensholt et al., 2006; Elberling et al., 2003). The soil is sandy and reddish in colour and was classified as an Arenosol by Batjes (2001).

On October 28th 2008, the area around the towers was burned by a bushfire. Bush fires occur regularly and mainly affect the herbaceous cover, while trees are generally less affected. This bushfire however, also damaged the trees, leaving some of them scorched and without any green leafs. Furthermore, almost all of the herbaceous cover was burned, leaving the surface clear of vegetation and dark in colour, which was still the case during a field visit in June 2009. The area affected by the bushfire is clearly visible in the Quickbird image (fig. 1) and covers a large part of the study area, but not the plantations in the south and the south-east.

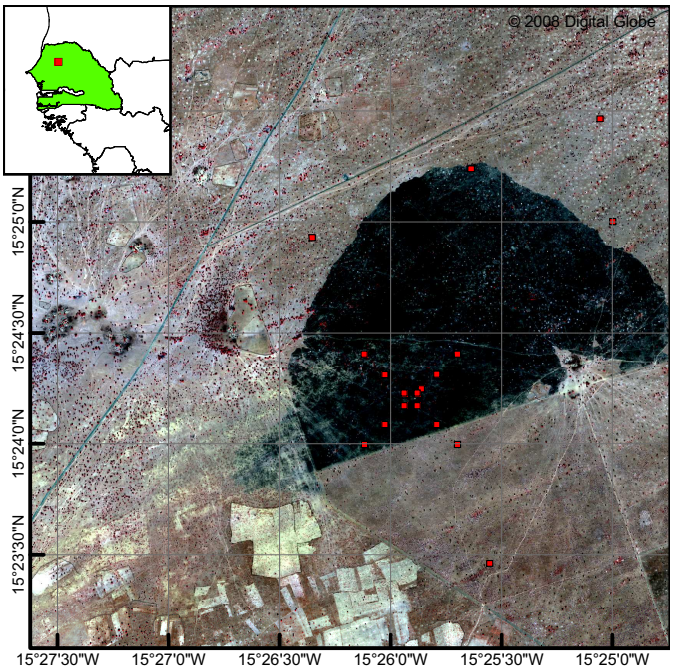

Figure 1: The location of the study site close to Dahra, Senegal. Also shown is the location of 18 of the 26 surveyed 50x50m plots. The area shown is a subset of the full Quickbird image.

3. Method and data

The tree cover at the Dahra field site is sparse and the dominating land cover is scattered agricultural fields and savannas used as grazing lands by pastoralists. Trees are scattered in the landscape, either as isolated trees or as small clumps, where in some cases their distribution is induced by old dune systems. The task of identifying trees in this part of Senegal is, thus, not a case of tree stand parameter estimation for uniform, mono-culture stands as traditionally done in forest management studies. Tree age and size vary widely, and, depending on the species, some trees are actively shaped by both people and animals. These factors also influence the development of allometric models, which relate different tree parameters to each other, since the trees are not allowed to develop undisturbed. These difficulties are accounted for by performing manual and object-based analyses of tree crown cover and tree count. The results are validated through comparisons with key tree parameters obtained from a field survey, e.g. species, DBH, stem cross-sectional area (CSA), height, crown radius and crown base height. Allometric models for the different tree species at the site are determined based on the field data.

3.1. Field survey

A field survey was carried out in July 2008 at the Dahra field site. A total of 26 square 50x50 meter plots were surveyed. In order to represent the major forms of land use in the area, the plots were selected based on a number of criteria including proximity to the towers, perceived representativeness, and their spatial distribution. The positions of 18 of the plots are shown in figure 1, while the rest is located further away to the south-west, north-west and north-east. Only two plots were located in the plantations in the southern and south-eastern direction as these areas are not representative of the surrounding tiger bush. The plots were geolocated by GPS at the centre of each plot.

Parameter	Note
Tree id	Uniquely identifies the tree
Species	
Tree height	Estimated from a distance
Crown radius	In the south to north direction
Crown base height	Distance from the ground to the bottom of the crown
Stem diameter at breast height	For trees with more stems at breast height, these were also measured

Table 1: Parameters surveyed for each tree during the field survey.

For each of the 26 plots, all trees of more than one meter height were surveyed for the parameters listed in table 1. Some inaccuracies in the delineation of the plots due to GPS-accuracy, alignment of the plots along east-west and north-south, and in the measurement of tree height and crown diameter are to be expected. In cases where it was impossible to measure stem diameter at breast height (DBH), e.g. due to small tree height, DBH was measured at the highest possible level.

3.2. Allometric models

Only a limited number of studies was carried out on the species relevant to this study, and most of these concern the browse production and biomass rather than the relation between DBH and tree/crown size. Cissé (1980) investigated the Balanites aegyptiaca species and derived a relationship between foliage biomass and crown area,

tree height and stem circumference at 40 cm above ground level. By regression, they found a good correlation between foliage biomass (including fruits) and circumference of trunk (r=0.86). The correlation between foliage and tree height was even better with a correlation coefficient of 0.95.

Deans et al. (1999) estimated the relation between stem cross-sectional area (CSA) at 30 cm height and total above-ground biomass for Acacia Senegal, and obtained a linear relationship with a very good correlation (r^2=0.97). In another study (Deans et al., 2003) did not use DBH, which is commonly measured at 1.30 or 1.40 meter above ground, but CSA measured closer to the surface. They also investigated the relation between CSA and fine-root biomass and coarse-root biomass by fitting a power function, but the relation was weaker for those parameters. In Deans et al. (2003) the previous study was extended to more species and included more details in terms of above-ground biomass. They also measured C-content in the soil layer below the trees, but did not consider the relation between tree height or crown size and DBH; instead the focus was on the accumulation of nutrients and organic-matter.

Although in a completely different setting and for species not relevant to this study, Hirata et al. (2009) compared DBH from a field survey with predicted DBH values based on crown area derived from panchromatic Quickbird data. Their model also included information on stand density, age, and other stand parameters. They obtained good results, with coefficients of determination between 0.82 and 0.86 for two different species.

We have chosen to use simple logarithmic functions for our allometric models, as these performed well in terms of correlation coefficients, and because we are not interested in the saturation point as was investigated by Zhang (1997). Therefore, and in order to ease comparisons with other studies, we chose to focus on using DBH and CSA measured at standard height, even though many of the surveyed trees had several stems at breast height. We built logarithmic models as follows:

$$y = a \cdot \ln x + b \tag{1}$$

where y is tree height or crown radius, x is either DBH or CSA, and a and b are constants determined by fittting.

3.3. Image data

A QuickBird image was acquired over the study area for the date 2008-12-03 at approximately 11:51 am (see details in Table 2). QuickBird data was chosen as it provides very high resolution, multi-spectral data as well as a panchromatic band. This allows analyses of four spectral bands, including a near-infrared band, which is most suitable for vegetation studies due to the high reflectance of vegetation in this part of the spectrum. Furthermore, the panchromatic, high spatial resolution band allows the application of pan-sharpening methods, which merge information contained in a panchromatic band with that from coarser multispectral bands. The slight off-nadir viewing geometry reduces the effective resolution of the Quickbird pan-chromatic band to approximately 0.70 meters and to 2.80 meters for the 4 narrow spectral channels. Despite the slightly reduced spatial resolution, the data are still sampled with a pixel spacing of 0.60 and 2.40 meters, respectively.

The date of image acquisition in December 2008 is after the bushfire mentioned above. As the field survey was carried out prior to the fire, the image is not showing the same surface as surveyed. This is thought to mainly influence the reflectance of the soil/grass surface. Furthermore, some trees were scorched and lost all their green leaves; however, the fire is not thought to have significantly impacted the results of the tree analysis presented below.

Date of acquisition	2009-12-03	11:51 am
UL corner coor.	15.448629 N	15.478403 W
LR corner coor.	15.358288 N	15.384906 W
Multispectral res.	$\sim$ 2.8 m	4 channels
Panchromatic res.	$\sim$ 0.7 m	
Mean off-nadir angle	23.1 degrees	
Mean Sun Azimuth	158.2 degrees	
Mean Sun Elevation	49.7 degrees	
Mean Sensor Azimuth	15.8 degrees	
Mean Sensor Elevation	65.7 degrees	

Table 2: Overview of Quickbird data specifications and scene angular configuration

3.4. Image preprocessing

Preprocessing of the Quickbird image was performed in ENVI (version 4.2) and included conversion of DN's into radiances using the embedded calibration parameters. Rectification of the image was also carried out, using 8 ground control points collected on the ground. It should be noted that the accuracy of the GPS equipment used is approximately 5 meters, which is not sufficient to do an accurate rectification considering the 0.7/2.8 meter effective resolution of the satellite data. Some inaccuracies were identified with the rectification, but based on the available ground information it was not possible to improve the original rectification.

In order to increase the spatial resolution of the 4 multispectral channels, pan-sharpening was carried out with the "*Gram-Schmidt*"-function included in ENVI. Utilising the pan-sharpened channels, Normalized Difference Vegetation Index (NDVI, see (Tucker, 1979)) was calculated from bands 3 and 4 without atmospheric correction and principal component analysis was applied to the four spectral bands (see table 3 for eigenvalues). As expected, the first principal component was very similar to the panchromatic band, while component 2 was very useful for the identification of trees and shadows in both the burned and the unburned areas. The principal components and the

NDVI-image were used for assisting the manual tree identification, the tree height estimations, and as input to the automatic analysis with eCognition, all of which are described below.

PC no.	Eigenvalue	% of total variance
1	3951956	95.47 %
2	143324	3.46 %
3	36838	0.89 %
4	7157	0.17 %

Table 3: Eigenvalues and percent variance for each of the four principal components.

3.5. Quickbird image analysis

Recent progress in image processing capabilities now allows an integrated, interactive process of combined image segmentation and object classification. Such capabilities are available in several software packages such as eCognition (by Definiens), as well as in recent versions of Idrisi (by Clark Labs) and ENVI/IDL (by ITT Visual Information Solutions). The concepts behind image segmentation and object analysis are well known, but the easy access to these methods make them available to a much larger audience. With the current software capabilities and computational power it is now possible to apply "object oriented image analysis" methods to the new very high resolution satellite or airborne data (Baatz and Schäpe, 2000).

Bunting and Lucas (2006) used eCognition and CASI-2 data (1 meter spatial resolution) over a forest Queensland, Australia. Bunting and Lucas (2006) first masked non-forest areas and classified the rest into broad forest classes. They then identified crowns or crown clusters by locating local maxima and expanding them into larger objects. The crown/crown cluster objects were then iteratively split and merged according to their relative position, shape and spectral characteristics. This approach exemplifies the iterative, multi-step delineation process also applied in this study.

Here, first individual trees were manually identified in the Quickbird image. The identification utilised the pan-sharpened data, the NDVI-image and the principal components. The results were then compared with the field survey data for 17 plots within the Quickbird image, 12 in the burned area, and 5 outside. The two plantation plots were excluded from the analysis because the tree spacing does not allow an identification of individual trees. However, since the spacing in the plantation is systematic, it would be easier to estimate the tree count by measuring the spacing between tree rows and between trees within the rows, and then calculating the total number of trees in the plantation.

The manual identification of trees relies on the identification of tree crowns (e.g. high NDVI-values), but also on the shadows cast by the trees on the ground. Satellite-images recorded at noon at nadir geometry or, more generally, in situations where the sun is right behind the sensor, do not show shadows, which complicates tree-identification. This is especially the case when the contrast (e.g. in terms of NDVI) between the crowns and the background is low. This often occur in cases where the trees do not have dense canopies or where the background below is covered by dense vegetation. An accurate estimation of tree height is also only possible from tree crown shadows. Manual identification of trees also relies to some extent on trees not being clumped, but clumping is fairly common in the study area: especially within a few areas in the north-eastern corner of the Quickbird image clumping is induced by old dune systems. Despite the present clumping, the manual tree identification is not thought to be significantly influenced by it, as it was generally possible to separate the clumps into individual trees.

3.6. Tree height estimation

Tree heights were to be directly extracted from the Quickbird image, which is possible because sun elevation during the acquisition was less than 90 degrees (the sun was not right above the scene). Therefore, the tree shadows could be exploited to estimate their height (see table 2 for details on the Quickbird image). The calculation of the tree heights is somewhat complicated by the fact the sensor viewed the scene at an off-nadir angle, effectively offsetting the tops of the trees away from the sensor in relation to the shadows cast by the crowns on the ground. Otherwise, a simple triangle-calculation would have been sufficient to estimate tree height, since the sun elevation is known and the horizontal lengths of the shadows are easily estimated from the image. However, the off-nadir observation angle of the sensor and the almost opposite positions of the sun and sensor (azimuth angles of 158.2 and 15.8 degrees, respectively), would cause an overestimation of tree heights if not taken into account, since it displaces the tree crowns in the image away from their shadows. The optimal scene geometry for a scene that are to be used for tree height estimation, would be a scene recorded at nadir, but a few hours either before of after solar noon.

Tree height estimation requires the horizontal distance from the top point of the tree crown to the shadow cast by this point on the ground to be measured (in the azimuth direction of the sun). This requires that the top points of the tree crowns can be identified; in practice, only the approximate locations of the tree tops can be extracted. However, the shape of the shadow cast on the ground combined with information about crown density (e.g. from NDVI) still allows to make a qualified guess about tree height.

3.7. Automatic estimation of tree crown cover

The Quickbird scene (parts shown in fig. 1) covers an area of 100 km^2. At spatial resolution of 0.6 m this corresponds to 16692 x 16692 pixels: this renders a manual delineation and analysis of trees impractical. Therefore, the image analysis software "eCognition" (Definiens

GmbH) was employed to separate trees from background and shadows. The classified image was then analysed and the number of trees and tree crown cover (TCC) was obtained.

3.7.1. Object-based classification

Traditional image classification methods only make use of spectral information of individual pixels. However, given a sufficiently high spatial resolution, targeted physical objects usually extent over several pixels, e.g. at Quickbird's spatial resolution of 60 cm a circular tree crown with 2 m radius covers 35 pixels (12.6 m^2). Due to local variations in illumination, shadow, etc. over such extended physical objects, the respective pixels may exhibit substantial spectral variation and may overlap significantly with other spectral classes. This spectral variability is reduced considerably when analysing the pixels belonging to an object together; at the same time, it does not diminish the relevant spectral features of the object. Furthermore, image objects can be analysed w.r.t. shape, texture, area, scale, etc. eCognition exploits this additional information by classifying image objects rather than single pixels. Its patented "Multiresolution Image Segmentation" extracts homogenous image objects at a given scale (Baatz and Schäpe, 2000). The choice of 'scale' depends on the spatial resolution of the sensor and the size of the physical structures to be extracted. Applying multiresolution segmentation on several scales creates a hierarchy of image objects in which the vertical layers represent the image information in different spatial resolutions. All objects "know" their context, their neighbourhood, their sub- and super-objects, and the relations between them, e.g. 'relative border to', can be used to define classification rules and to introduce context information. eCognition exploits this wealth of object and hierarchy related information with a number of specialised classification methods.

3.7.2. Data and parameter settings

First, the Quickbird data were converted to at-sensor radiances using the embedded calibration information. Then Gram-Schmidt pan-sharpening was applied to increase spatial resolution to 60 cm. The normalised difference vegetation index (NDVI) was obtained from the pan-sharpened data and also principal component analysis (PCA) was performed. Pan-sharpening does not yield pixels with the same spectral contents as pixels actually measured at the increased resolution. However, this lack of spectral fidelity is assumed to be negligible because classifications are based on spectral contrast rather than on spectral contents. Principal components (PC) 1 & 2 and NDVI served as input to eCognition. Unfortunately, despite sufficient system resources eCognition could not process the complete Quickbird scene. Therefore, five spatial subsets of about 5000 x 5000 pixels each were processed. These rectangular subsets do not cover the complete scene but are sufficiently large to be representative. The subsets were placed at the four corners (upper left, upper right, lower left, and lower right) and at the centre of the image. The centre subset included most of the tree survey plots.

1. Multiresolution image segmentation was performed on only one level with the weights of the three image layers (PC 1 & 2 and NDVI) set to one. A fine scale was chosen to avoid mixed image objects, e.g. tree crowns mixed with tree shadows. Parameters for multiresolution segmentation were: scale: 10, shape: 0.3, compactness: 0.5.
2. Since the Quickbird data were acquired during Senegal's dry season, the contrast between average spectral object values proved to be insufficient for a successful classification of tree objects. Therefore, the fine scale level 1 objects were first classified as "green" if the NDVI of any of their member pixels exceeded 0.1. This also classifies image objects with low mean NDVI as "green", e.g. a dry tree with only some green in the centre of the crown. All other objects are classified as "background".
3. A second object level was created with classification-based segmentation: neighbouring "green" level 1 objects were merged into larger level 2 objects and classified as "tree or bush". Neighbouring "green" objects belonging to different but neighbouring trees or bushes are also merged: this causes a certain degree of clumping and reduces the number of tree objects, but it does not affect the TCC estimate.
4. In a separate classification, the impact of clumping on average tree crown area was reduced by limiting the area of tree objects to 300 m^2 (about 10 m radius). This excludes large agglomerations of trees, e.g. long connected strips of tiger bush (compare figure 2A with figure 2B. Choosing a smaller maximum tree object area did not change results significantly. The area of 300 m^2 corresponds to a maximum of 5 clumped trees with crown radius of about 4-5 m (about the largest crown found in the field survey), which - ignoring the large strips of tiger bush - proved to be a reasonable estimate for "normal" clumping.

3.7.3. Correction for tree clumping

Quickbird's spatial resolution of 60 cm is not sufficient to resolve very small trees or trees located directly next to each other. However, the field survey included very small trees and did not record tree clumping. Therefore, a "clumping correction factor" was estimated from 153 photographs taken during the field survey. The photographs were evaluated for single trees and clearly identifiable groups of 2 to 5 trees: the aim was to obtain a representative statistic rather than to claim completeness. Figure 3A shows an example for tree clumping and the result of the analysis is shown in figure 3B.

Assuming that eCognition clumps the groups of trees identified in the photographs into single "tree" objects, a clumping correction factor c was calculated as weighted

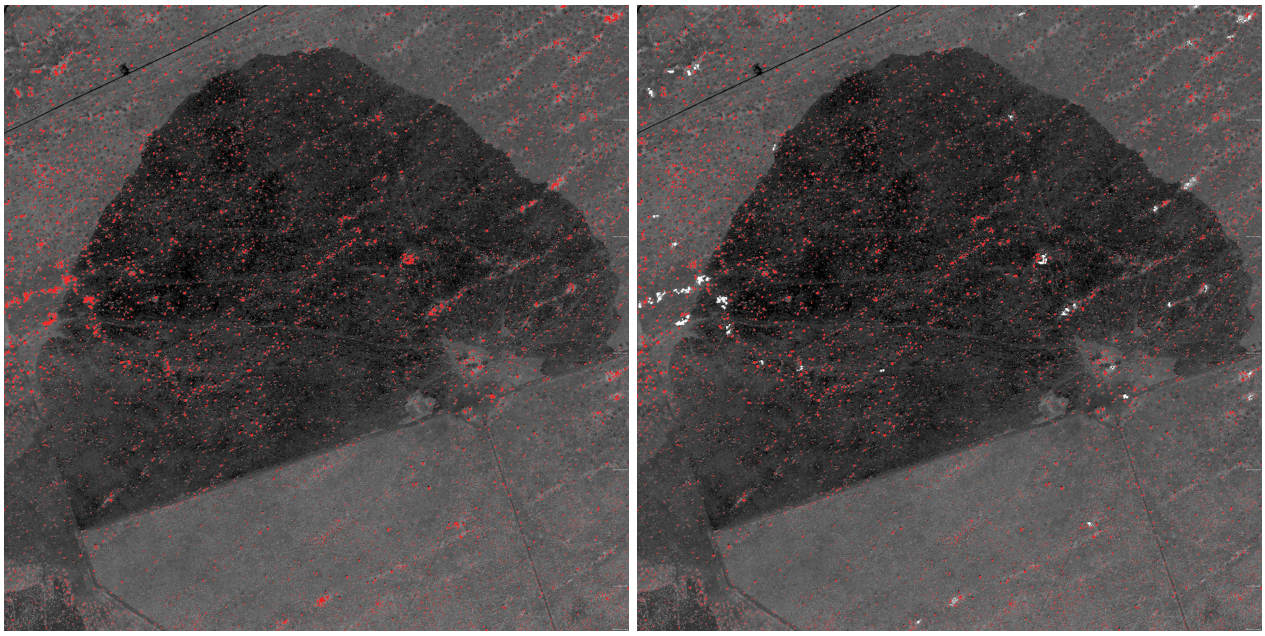

Figure 2: Left: Upper right subset, all "trees" red (UR-all). Right: Upper right subset, "trees" $\prec$ 300 m^2 red (UR-300)

Figure 3: Left: Clumped trees at Dahra field site. Right: Number of groups with 1 to 5 trees in group (obtained from photographs).

average of the number of the groups:

$$c = \frac{\sum_{i=1}^{5} N_i \cdot i}{\sum_{i=1}^{5} N_i} \quad (2)$$

where N_i is the number of groups with i trees found in the photographs.

From figure 3B, the clumping correction factor is determined as c = 672 / 409 = 1.64. This factor was used to estimate the actual number of trees within tree objects "300-co" as well as the actual area and radius of the mean tree crown. Furthermore, since the "background" objects are more homogeneous than the "tree" objects, eCognition assigns mixed pixels at tree - background boundaries to the "tree" objects; therefore, mean tree crown radius is finally estimated as: mean "300-co" radius - (Quickbird pixel size / 2).

4. Results

4.1. Field tree survey

Summary statistics of the field survey are shown in tables 4 and 5, grouped per plot and per species, respectively. In total, 189 trees were sampled in 26 plots, of which 4 did not contain any trees. 12 plots were located within the area affected by the bushfire, while 14 were outside. Out of these 14, half were located outside the Quickbird image, and are therefore excluded from most of the analysis. Two plots were within the plantation area: these are also

Point	Note	Count	Avg. Height	Min. Height	Max. Height	Avg. DBH	Avg. radius	%TCC
1	burned	2	2.90	2.50	3.30	0.34	1.09	0.3
3	burned	5	2.84	1.40	4.20	0.22	1.64	2.1
6	burned	4	4.88	4.00	5.50	0.39	2.77	4.2
9	burned	3	5.50	4.50	7.50	0.71	2.92	3.5
12	burned	6	2.68	2.10	3.20	0.21	1.44	1.7
15	burned	1	3.00	3.00	3.00	0.44	2.55	0.8
17	burned	7	4.26	1.20	7.00	0.41	2.06	5.2
19	burned	6	5.28	4.00	7.50	0.60	3.49	10.1
20	burned	1	5.50	5.50	5.50	0.70	2.50	0.8
23	burned	5	3.78	1.90	5.30	0.42	1.54	2.0
26	burned	8	4.26	2.50	7.50	0.40	1.81	4.2
28	burned	2	4.15	1.80	6.50	0.47	2.05	1.4
29	not burned	5	3.92	2.30	7.50	0.31	1.88	2.5
30	not burned	0						0.0
31	not burned	14	4.92	1.90	7.50	0.55	2.10	9.4
32	not burned	10	3.98	2.10	5.00	0.34	1.97	5.7
60	not burned	0						0.0
47	outside QB	12	4.49	2.80	6.00	0.46	2.38	9.2
48	outside QB	0						0.0
49	outside QB	12	3.23	1.60	6.50	0.29	1.60	4.8
50	outside QB	22	2.29	1.70	3.00	0.14	1.48	6.4
51	outside QB	2	1.90	1.70	2.10	0.11	0.98	0.3
52	outside QB	1	7.00	7.00	7.00	0.90	3.10	1.2
61	outside QB	0						0.0
14	plantation	20	2.30	1.20	6.50	0.23	1.23	5.7
59	plantation	41	3.00	1.80	5.50	0.16	2.15	25.6

Table 4: Statistics for all 26 plots surveyed. %TCC is the percentage of each plot covered be tree crowns calculated assuming circular crown shapes and no tree crown clumping. All measurements are in meters except count and %TCC.

mostly excluded from the analysis, because the trees are generally too small to be included in the survey, while the overall plot tree density is too high for an identification of individual trees in the Quickbird image (especially a problem for plot number 14).

Only five different tree species were found in the survey area and two of these were only represented by one tree each. The Leptadenia Hastata resembles a bush more than a tree and was often found next to trees. The area is dominated by two Acacia species and the Balanites Aegyptiaca (see table 5). The Acacia Raddiana is a sub-species of Acacia Tortilis (will be referred to as Acacia Raddiana throughout this study) and is typical for silty/loamy pediplains in the Sudano-Sahelian subzone (Le Houerou, 1989) as is Acacia Senegal. The Acacia Raddiana is generally larger than the Acacia Senegal.

4.2. Allometric models for tree height

The correlation between measured tree heights and diameter at breast height (DBH) from the field survey was analysed: it shows that DBH can be reliably estimated from tree height (see fig. 4). Furthermore, DBH and tree height can often be related to total above ground biomass and, thus, allow to estimate the total carbon content in the tree-vegetation.

Fig. 4 shows allometric models for the relation between maximum DBH and tree height for the Acacia-species, for Balanites Aegyptiaca, and for the other trees surveyed. The sizes and ages of the trees in the area vary widely, which also shows in the plots. The only exception is Acacia Senegal, which only varies over a narrow range of tree heights and DBH compared to the two other species. As distinction between the species is impossible from the Quickbird image and because of the very similar fits for the Acacia and Balanites species, we also made a correlation analysis based on all trees surveyed in the field, to evaluate the robustness of DBH-estimation based on tree height. As fig. 4D shows, the correlation is good with an r^2-value of almost 0.8, indicating that despite the presence of several different tree species, DBH can be estimated reliably across the study area solely based on tree height. The Acacia Senegal trees in the plantation plots were excluded from the analysis, as they are managed differently than the trees in the surrounding areas. Furthermore, the main focus of this study is the non-plantation areas, and other methods will be more appropriate for the plantations.

We also investigated the relation between total cross-sectional stem area (CSA) (calculated from the DBH) and tree height. The difference between the two is, that many of the surveyed trees had more than one stem at breast

Species	Count	Min. height	Max. height	Avg. height	Avg. DBH	Avg. crown radius
Acacia Raddiana	19	2.1 m	7.5 m	4.22 m	0.37 m	2.50 m
Acacia Senegal	82	1.2 m	5.5 m	2.61 m	0.15 m	1.71 m
Balanites aegyptiaca	86	1.2 m	7.5 m	4.07 m	0.43 m	1.96 m
Combretum Glutinosum	1	7.0 m	7.0 m	7.00 m	0.81 m	4.00 m
Leptadenia Hastata	1	3.0 m	3.0 m	3.00 m	0.29 m	1.50 m
Total	189	1.2 m	7.5 m	3.46 m	0.31 m	1.92 m

Table 5: Summary statistics grouped per species for the all surveyed trees within the 26 test-plots.

height. These were also measured, but in the analysis above, only the largest stem was used for the correlation analysis. Using total cross-sectional stem area include all measured stems and therefore might give a better representation of the tree size. As the CSA is calculated assuming a circular stem shape, the only difference between the two is that all stems are included in CSA and the DBH only represent the largest stem.

The results of the CSA-tree height analyses (not shown) are very similar to results presented in fig. 4. For CSA, the found correlation for Acacia Senegal was worse with a r^2-value of 0.404 compared to $r^2 = 0.697$ for DBH. The overall correlation for all trees is on the other hand slightly better with r^2-values of 0.801 and 0.791 respectively, mainly due to a better fit for Balanites Aegyptiaca. Overall, the performance of CSA and DBH is almost identical and indicate that maximum diameter is as good an estimation as total CSA. Also, Acacia Senegal show a significantly different relation than the two other main species found in the area, mainly due to a low range of values both in terms of tree height and DBH/CSA.

4.3. Allometric models for crown radius

Similarly to considering the relation between DBH and tree height, we also developed allometric models for the relation between DBH and CSA and crown radius as shown for CSA in fig. 5. As was the case for tree height, Acacia Raddiana and Balanites Aegyptiaca show good performance with r^2-values of 0.7 and 0.8 respectively, while the correlation is very bad for Acacia Senegal (when excluding the two plantation plots). The results for DBH are similar to the results with CSA, except for the case of the entire population of Acacia Senegal trees where CSA perform much better with a r^2-value of 0.65 compared to 0.26 for DBH. Despite of this, we excluded the Acacia Senegal trees from fig. 5D, as we are mainly concerned with how the method will perform outside the plantations. Because of the bad performance of DBH for Acacia Senegal, the r^2-value found for all tree species in 5D is also significantly better for CSA than for DBH.

The difference between including and excluding the plantation plot Acacia Senegal trees are shown in fig. 5B, where the model fits for both cases have been included. For both cases, the effective range is limited, but including the plantation plots still improves the correlation significantly. The lack of correlation for the non-plantation trees could be explained by the fact that Acacia Senegal is often used for browse for cows and goats, as well as for firewood. This means that trees are in some cases trimmed, resulting the in crown radius not being indicative of the stem size. This is not the case within the plantation, where trees are used for rubber production and the browsing by animals is limited.

4.4. Tree count comparison between field survey and manual Quickbird image analysis

A comparison was made between the tree count from the field survey and manual identification of trees in the Quickbird image. The results are shown in figure 6 which include data from both burned and unburned areas (17 plots in total). The correlation is acceptable with an r^2-value of 0.8057, but slope (0.76) and offset (1.10) indicate that the manual identification of trees in the Quickbird image has a tendency to underestimate the tree count for areas with relatively many trees. This could be explained by problems occurring when trees are clumped together, which makes the delineation of the individual trees difficult. This will only have an influence in areas with higher tree densities and where clumping is present. Furthermore, some problems were identified with the rectification of the Quickbird image, which influences the quality of the correlation. The correlation confirms that it is possible to manually identify trees in the Quickbird image with acceptable accuracy to use the method for larger areas.

4.5. Tree crown cover from Quickbird and eCognition

The tree crown cover was estimated in the Quickbird image using the eCognition software as described above. This was compared to the per plot tree crown cover estimated in the field. The field values were found by calculating the horizontal area of each tree based on the measured diameter assuming a circular crown. Furthermore it was assumed that crowns do not overlap.

The average tree cover fractions agree well: the average plot tree crown cover from the survey was 3.02% (values from table 4) compared to 2.97% estimated from the classification of the Quickbird image with eCognition (the average of the 12 individual plot TCC shown in figure 7). On the plot scale, the agreement is worse (see figure 7) with a r^2 of 0.51. The low correlation is mainly caused by the small number of trees per plot, which severely limits the representativeness of this result. Furthermore, errors

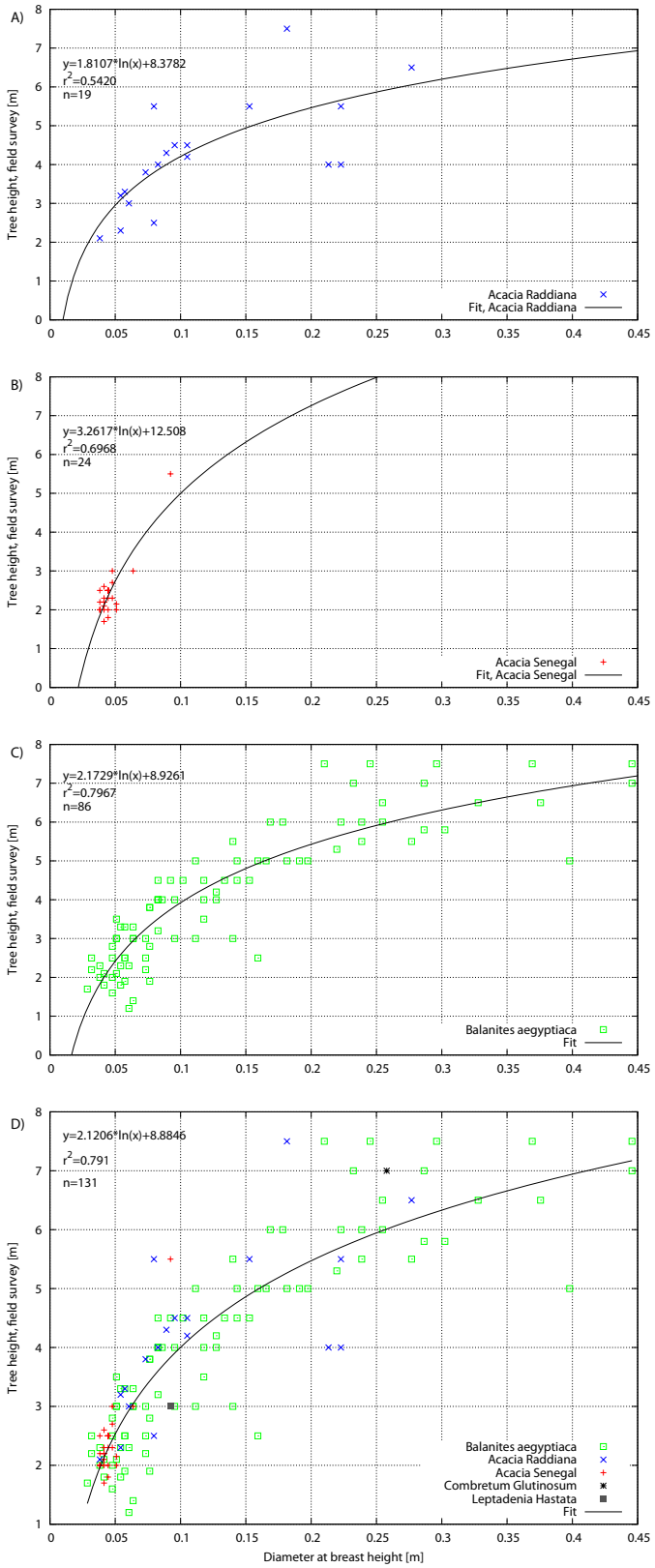

Figure 4: Allometric model of the relation between DBH and tree height derived from the field survey data. A) shows the model for Acacia Raddiana species, B) for Acacia Senegal, C) for Balanites Aegyptiaca and D) for all trees (and species) in the field survey. The plots have been made with the same x and y-range to ease comparison.

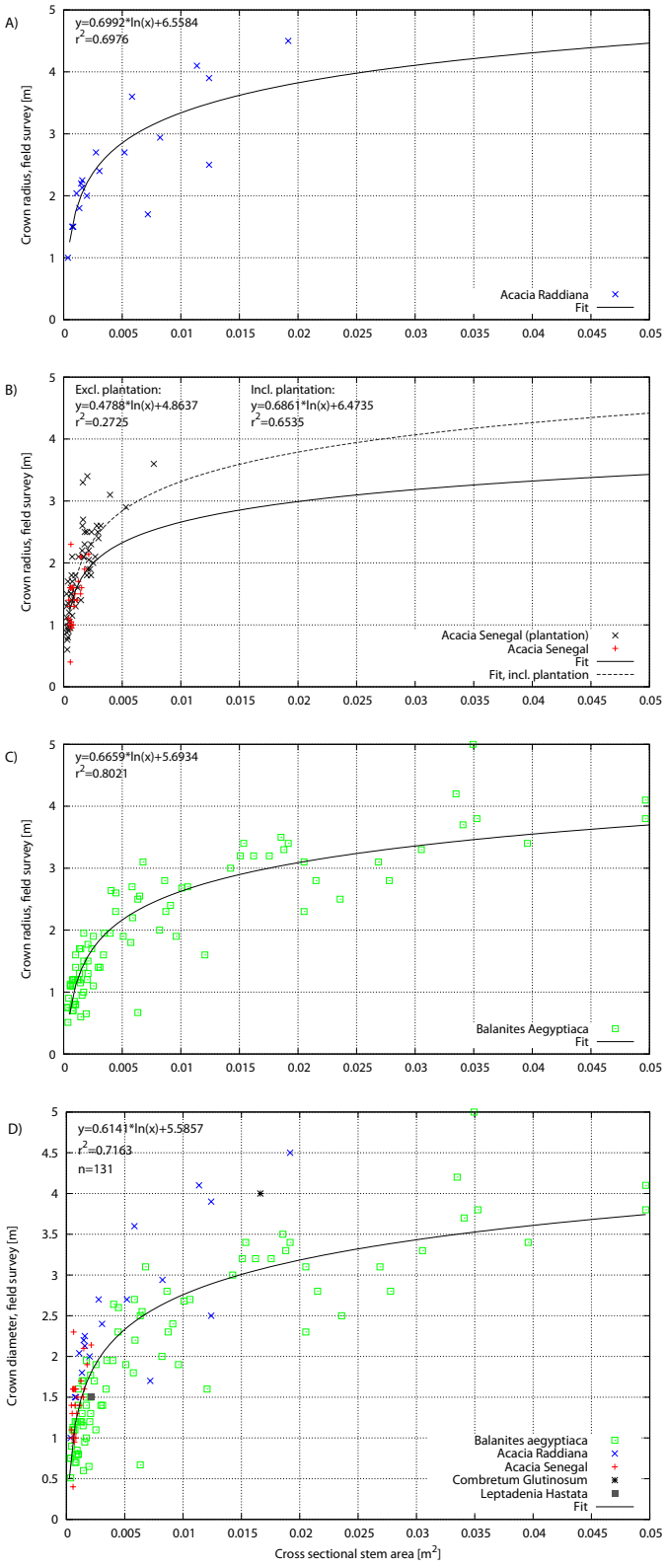

Figure 5: Allometric models for CSA and crown radius for the three main species and for all trees surveyed. As in figure 4 the axes of the plots have been scaled to the same range to ease comparison. Acacia Senegal trees from the plantation plots have been excluded except from in B, where they are shown for comparison.

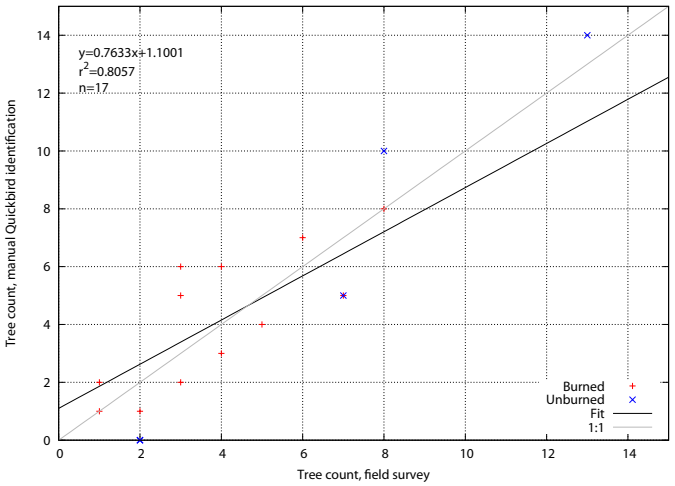

Figure 6: Correlation between tree count in the field survey, and from manual identification of trees in the QuickBird image for 17 out of the 26 plots (plantation plots excluded).

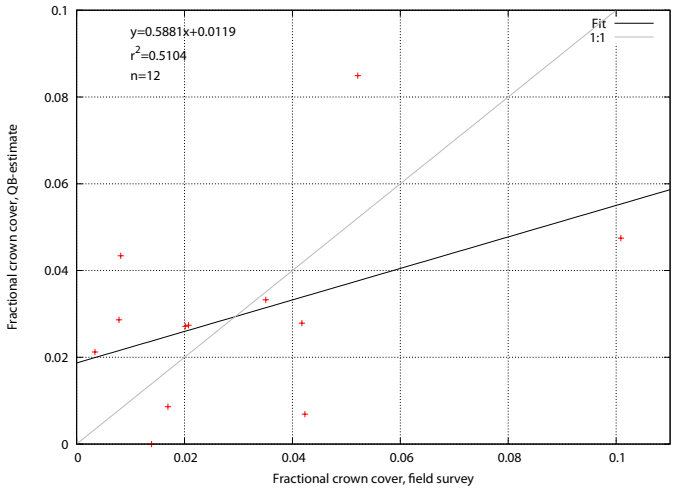

Figure 7: Scatterplot and correlation between tree crown cover derived from the field survey data and from analysis of the QuickBird image with the eCognition software.

in the rectification lead to errors in the tree count and also affect tree crown cover estimation. The fire that occurred between the field survey and the acquisition of the Quickbird image might also have affected the tree crown cover estimation as many of the lower trees were severely burned; in some cases green leaves were completely absent, which made crown delineation difficult.

Table 6 shows the results of the analysis performed with eCognition for three spatial subsets of the Quickbird scene. Only results for the three northern subsets are given, since the lower left and lower right subsets were influenced by agricultural land in the south of the Quickbird scene and, are, therefore, not representative for tiger bush. The determined TCC for the centre (CC) subset (3.0%) is practically identical with the average TCC obtained from the field survey (3.02%). The upper left (UL) and the upper right (UR) subset yield slightly higher TCC (3.7% and 4.5%, respectively) than the CC subset, but this is plausible since the CC subset includes the area affected by the bush fire. The mean radii determined for the three subsets with eCognition and then corrected for clumping are 2.3m, 2.5m, and 2.8m; when subtracting the size of half a Quickbird pixel (0.3m) from these values to account for mixed pixels at tree boundaries, the results are close to the average tree crown radius of 1.92m determined in the field survey.

4.6. Tree height comparison

The height of the trees was estimated from the Quickbird image as described in section 3.6. Figure 8 shows the correlation between the field survey data and the height estimates from Quickbird. Out of the 19 plots covered by the Quickbird image, 15 were included in the analysis. The two plots without trees were excluded as well as the two plantation plots as it was impossible to identify the individual tree shadows in the plantation area.

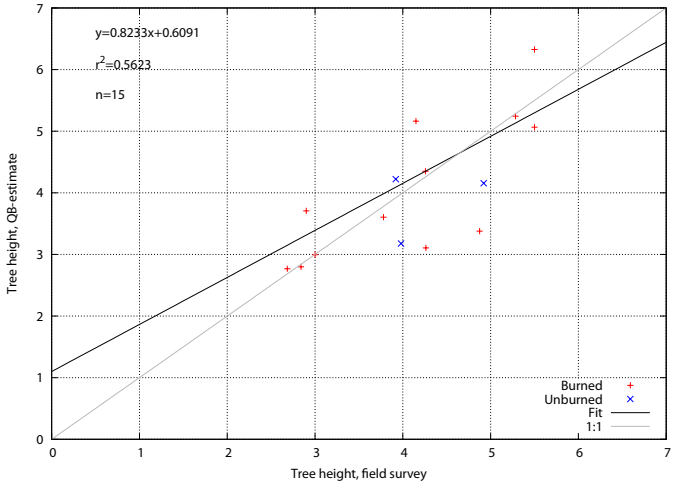

Figure 8: Comparison between tree heights measured in the field, and tree heights estimated from the QuickBird image taking advantage of the off-nadir viewing and illumination geometry. The values are calculated as average tree height values per plot and do not represent the individual trees.

The correlation between tree heights estimated from the two methods is reasonable, with a r^2 of 0.56 but with a slope of 0.83. Considering the uncertainty inherent in the tree height estimation from the Quickbird image, the results are promising although it relies on certain illumination and viewing geometries. It is an alternative and direct approach for obtaining tree heights, compared to deriving crown radius and then obtaining tree height using an allometric model relating crown radius to tree height.

4.7. Upscaling TCC using NDVI

An attempt was done at upscaling the TCC found from the Quickbird analysis using a plot scale correlation between TCC and NDVI as done by other authors (Hansen et al., 2002; Carreiras et al., 2006). The firescar present in

Subset	TCC [%]	total area [m^2]	trees	mean area [m^2]	mean radius [m]
UL-all	3.7	336165	9000	37.4	3.4
UL-300	-	299475	8943	33.5	3.3
UL-300-co	-	299475	14666	20.4	2.5 (2.2)
UR-all	4.5	403948	6668	60.6	4.4
UR-300	-	265365	6491	40.9	3.6
UR-300-co	-	265365	10645	24.9	2.8 (2.5)
CC-all	3.0	326049	10855	30.0	3.1
CC-300	-	301374	10828	27.8	3.0
CC-300-co	-	301374	17757	17.0	2.3 (2.0)

Table 6: Analyses of upper left (UL), upper right (UR), and centre (CC) spatial subsets of the Quickbird scene. "all" means all objects classified as trees, "300" means only objects with an area less than 300 m^2, and "300-co" is the number of trees with less than 300 m^2 corrected for clumping ("300" trees times 1.64). The values in brackets for mean "300-co" radii give the radius minus 30 cm (Quickbird pixel / 2) to account for the ring of mixed pixels at the perimeter of tree objects

the Quickbird image will affect this correlation, which is why only plots within the firescar was included. The results of the correlation analysis is shown in fig. 9 and show an almost absence of correlation between the two parameters. A similar test was made for a Quickbird image acquired on 2007-09-25 (during the rainy-season) and similar results were obtained. Furthermore, we also performed a correlation analysis including 25 plots using a dry-season, 15 meter resolution ASTER scene from 2007. This analysis (not shown) also showed a very weak correlation between TCC and NDVI. Based on the obtained results, we concluded that attempts at using a TCC-NDVI based upscaling method for upscaling the results to MODIS and/or MSG SEVIRI scale for the region would not be feasible.

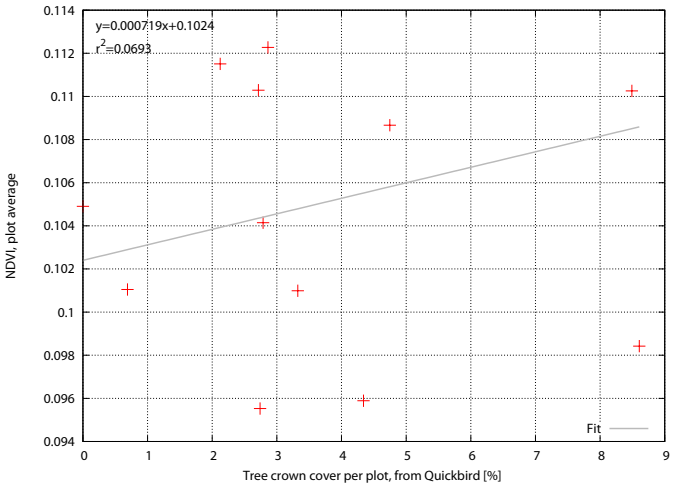

Figure 9: Scatterplot of NDVI against TCC for 12 plots (all within the burned region). The TCC is based on the Quickbird analysis and the NDVI is average values for each plot.

5. Summary and concluding remarks

A field survey was performed in order to characterise the woody vegetation at a permanent validation site for satellite products, located in the semi-arid northern Senegal. The site is mainly covered by sparse tiger bush with the woody vegetation dominated by Balanites Aegyptiaca and different Acacia species. Among the surveyed parameters were tree type, height, tree crown radius, and DBH, which were used to determine allometric models with quantities available from remote sensing (e.g. tree crown radius). Tree crown cover (TCC) was determined from satellite data with an object-based classification method. The average TCC of 12 field survey plots (3.0 %) agreed well with the corresponding TCC determined from remote sensing (3.0 %); for larger areas not covered by the field survey the TCC determined from remote sensing varied between 3.0 % and 4.5%. Based on field survey information, an empirical correction factor was determined to account for tree clumping. This correction factor was then used to obtain a better estimate of the number of trees and the average tree crown area and radius from the remote sensing data, which consisted of one panchromatic and four multi-spectral channels of Quickbird data. The average tree crown radius determined from the field survey (1.9m) matched the respective value from remote sensing (about 2.0m) well, which gives confidence in estimating these parameters for large areas from remote sensing data, e.g. on scale of a MSG pixel. The allometric model describing the relationship between TCC and CSA then also allows to estimate the tree biomass from remote sensing. The TCC and the average tree crown radius determined here can serve as input to a Geometrical Optical Radiation Transfer (GORT) model, which allows the upscaling of temperatures based on radiometric measurements in the thermal infrared to MSG pixel scale.

The allometric models developed in this study for the three main species studied, generally showed good performance with r^2-values around 0.7 to 0.8. Acacia Senegal behaved differently than the other species, partly due to a narrow range of stem circumferences and an apparent de-coupling of DBH/CSA and, especially, crown radius. In terms of estimating tree parameters from analyses of the Quickbird image, the allometric models for tree height and crown radius produce good results, although the predictive capabilities of the models for large trees is somewhat limited due to the shape of the functions used. A

small change (e.g. from estimation error) in tree height or crown radius might lead to significant changes in the DBH or CSA. Despite of this, the methods applied in this study demonstrate the potential of using high resolution remote sensing data for tree inventory analysis, which can ultimately be applied for biomass monitoring.

The attempt at upscaling the estimation of TCC using a relation between TCC and NDVI failed, due to the lack of correlation between the two parameters. On the local scale, the lack of correlation could be related to the occurrence of the bushfire, but analyses of other images including an ASTER scene all gave similar results. This is believed to be caused by the relative low TCC in the area, which means that differences in the background (soil and grasses) dominate the local changes in NDVI compared to the influence of the tree crowns on the NDVI. In areas where such a relation has been shown to work, TCC is generally higher, increasing the influence of the tree crown NDVI on the overall plot-scale NDVI.

Acknowledgement

This work contributes to the AMMA Project (http://www.amma-international.org). Based on a French initiative, AMMA was built by an international scientific group and is currently funded by a large number of agencies, especially from France, UK, US and Africa. It has been the beneficiary of a major financial contribution from the European Communitys Sixth Framework Research Program. The study was also partly funded by The International Research School in Water Resources (FIVA) at the University of Copenhagen, Denmark.

The work was partially carried out within the context of the Land-SAF project, funded by the European Organization for the Exploitation of Meteorological Satellites.

References

Baatz, M., Schäpe, A., 2000. Angewandte Geographische Informationsverarbeitung XII, Beitrge zum AGIT-Symposium Salzburg 2000. Wichmann Verlag, Heidelberg, Ch. Multiresolution segmentation an optimization approach for high quality multi-scale image segmentation, p. 1223.

Bai, Y., Walsworth, N., Roddan, B., Hill, D., Broersma, K., Thompson, D., 2005. Quantifying tree cover in the forest-grassland ecotone of British Columbia using crown delineation and pattern detection. Forest Ecology and Management 212 (1-3), 92 – 100.

Batjes, N. H., 2001. Options for increasing carbon sequestration in West African soils: an exploratory study with special focus on Senegal. Land Degradation & Development 12 (2), 131–142.

Bunting, P., Lucas, R., 2006. The delineation of tree crowns in Australian mixed species forests using hyperspectral Compact Airborne Spectrographic Imager (CASI) data. Remote Sensing of Environment 101 (2), 230 – 248.

Carreiras, J. M., Pereira, J. M., Pereira, J. S., 2006. Estimation of tree canopy cover in evergreen oak woodlands using remote sensing. Forest Ecology and Management 223 (1-3), 45 – 53.

Cissé, M. I., 1980. Browse in Africa. ILCA, Addis Ababa, Ch. The browse production of some trees of the Sahel: relationships between maximum foliage biomass and various physical parameters, pp. 205–210.

Culvenor, D. S., 2002. Tida: an algorithm for the delineation of tree crowns in high spatial resolution remotely sensed imagery. Computers & Geosciences 28 (1), 33 – 44.

Deans, J., Diagne, O., Lindley, D., Dione, M., Parkinson, J., 1999. Nutrient and organic-matter accumulation in Acacia Senegal fallows over 18 years. Forest Ecology and Management 124, 153–167.

Deans, J. D., Diagne, O., Nizinski, J., Lindley, D., Seck, M., Ingleby, K., Munro, R., 2003. Comparative growth, biomass production, nutrient use and soil amelioration by nitrogen-fixing tree species in semi-arid Senegal. Forest Ecology and Management 176, 253–264.

Elberling, B., Fensholt, R., Larsen, L., Petersen, A.-I., Sandholt, I., 2003. Water content and land use history controlling soil CO_2 respiration and carbon stock in savanna soil and groundnut fields in semi-arid Senegal. Geografisk Tidsskrift - Danish Journal of Geography 103, 47–56.

Fensholt, R., Sandholt, I., 2005. Evaluation of MODIS and NOAA AVHRR vegetation indices with in situ measurements in a semi-arid environment. International Journal of Remote Sensing 26 (12), 2561–2594.

Fensholt, R., Sandholt, I., Stisen, S., July 2006. Evaluating MODIS, MERIS, and VEGETATION vegetation indices using in situ measurements in a semiarid environment. Geoscience and Remote Sensing, IEEE Transactions on 44 (7), 1774–1786.

Hansen, M. C., DeFries, R. S., Townshend, J. R. G., Marufu, L., Sohlberg, R., 2002. Development of a MODIS tree cover validation data set for Western Province, Zambia. Remote Sensing of Environment 83 (1-2), 320 – 335.

Hirata, Y., Tsubota, Y., Sakai, A., 2009. Allometric models of DBH and crown area derived from QuickBird panchromatic data in Cryptomeria japonica and Chamaecyparis obtusa stands. International Journal of Remote Sensing 30, 5071–5088.

Larsen, M., Rudemo, M., 1998. Optimizing templates for finding trees in aerial photographs. Pattern Recognition Letters 19 (12), 1153 – 1162.

Le Houerou, H. N., 1989. The grazing land ecosystems of the African Sahel. Springer-Verlag, Berlin, New York.

Leckie, D. G., Gougeon, F. A., Walsworth, N., Paradine, D., 2003. Stand delineation and composition estimation using semi-automated individual tree crown analysis. Remote Sensing of Environment 85 (3), 355 – 369.

Song, C., Woodcock, C. E., 2003. Estimating Tree Crown Size from Multiresolution Remotely Sensed Imagery. Photogrammetric Engineering & Remote Sensing 69, 1263–1270.

Stisen, S., Sandholt, I., Nrgaard, A., Fensholt, R., Jensen, K. H., 2008. Combining the triangle method with thermal inertia to estimate regional evapotranspiration – applied to msg-seviri data in the senegal river basin. Remote Sensing of Environment 112 (3), 1242 – 1255.

Toure, A., Rasmussen, K., Diallo, O., Diouf, A., 2003. Actual and potential carbon stocks in the north sudanian zone. A case study: The forests of Delbi and Paniates in Senegal. Geografisk Tidsskrift, Danish Journal of Geography 103, 63–70.

Tucker, C. J., 1979. Red and photographic infrared linear combinations for monitoring vegetation. Remote Sensing of Environment 8 (2), 127 – 150.

Zhang, L., 1997. Cross-validation of Non-linear Growth Functions for Modelling Tree Height-Diameter Relationships. Annals of Botany 79, 251–257.

Paper IV

Intercomparison of LST products from MSG SEVIRI and comparison with MODIS data and in situ measurements in West Africa

Authors:

Mads Olander Rasmussen, Frank-M. Göttsche, Eric Mougin, Franck Timouk, Simon R. Proud and Inge Sandholt

Status:

Submitted to Remote Sensing of Environment, September 28th 2010.

Intercomparison of LST products from MSG SEVIRI and comparison with MODIS data and in situ measurements in West Africa

Mads O. Rasmussen[a,*], Frank-M. Göttsche[b], Eric Mougin[c], Franck Timouk[c], Simon R. Proud[a], Inge Sandholt[a]

[a] *Department of Geography and Geology, University of Copenhagen, Øster Voldgade 10, 1350 Copenhagen K. Denmark*
[b] *Karlsruhe Institute of Technology, Hermann-von-Helmholtz-Platz 1, 76344 Leopoldshafen, Germany*
[c] *LMTG (UMR 5563 CNRS-UPS-IRD), 14 Avenue Edouard Belin 31400 Toulouse, France*

Abstract

This paper validates several satellite-based estimates of land surface temperature (LST) for semi-arid West Africa by intercomparing them and using ground measurements from two locations in Senegal and Mali as reference. The validation focuses on LST estimates based on Meteosat Second Generation (MSG) SEVIRI data; these are obtained with variants of the "split window"-technique, which use different methods for assessing atmospheric water vapour content and surface emissivity. In addition, the effect of using different cloud masking procedures is studied. Furthermore, LST estimates obtained from MODIS data are compared with field observations from the two sites. The results show that in the monsoon season none of the MSG SEVIRI-based LST retrieval methods performs satisfactorily, while accuracy, in terms of bias, correlation and slope, improves significantly with the onset of the dry season. The large discrepancies between field observations and satellite LST estimates are thought to be caused mainly by problems with atmospheric correction during the rainy season. Furthermore, the choice of cloud mask significantly effects the performance of the chosen algorithms.

Keywords: Land Surface Temperature, MSG SEVIRI, MODIS, monsoon season

1. Introduction

As satellite-based products of bio-physical variables become easier accessible for various applications, validation and accuracy assessment become increasingly more important. LST-products are used for a variety of purposes, not at last in hydrology, both as input to or for the validation of physically-based, distributed hydrological models (Stisen et al., 2008a) and SVAT-models (Coudert et al., 2006, 2008), as well as for direct estimation of evapotranspiration, soil moisture, and plant water stress (Norman et al., 1995; Nishida et al., 2003; Sandholt et al., 2002; Verstraeten et al., 2006; Stisen et al., 2008b). For these applications it is highly important that the input LST-estimates are unbiased, the spatial LST patterns are realistic, and the diurnal patterns of LST variation are well represented.

Commonly LST is estimated by combining information from two or more bands located in atmospheric windows in the thermal infrared (TIR) part of the spectrum (the split-window technique (Price, 1984)). The accuracy of LST-estimation is influenced by a number of sources of error and noise, including (1) the ability of the algorithms to correct for atmospheric water vapour content (W) and aerosols, (2) the assignment of realistic values of emissivity to the land surface, (3) errors associated with satellite image co-registration, (4) imperfections of the cloud masks used, and (5) directional effects (i.e. anisotropy), which are associated with interactions between varying viewing and illumination geometry and e.g. a vegetation canopy. This paper focuses on the first four sources of error, while the fifths is discussed elsewhere (Smith et al., 1997; Pinheiro et al., 2004, 2006; Trigo et al., 2008c; Rasmussen et al., 2010b,c).

With the launch of the geostationary MSG satellites, it is now possible to estimate LST every 15 min over Africa and Europe using split-window algorithms. Unlike the first generation of Meteosat's with a single TIR channel, MSG provides measurements in four TIR channels. Three of these are located within the two atmospheric TIR windows and greatly improve the estimation of LST from space. Several algorithms have been proposed but, to our knowledge, none of these have to date been extensively validated over the African Continent. In this study we compare the results of several SEVIRI-based LST algorithms with each other and to in situ data from two field sites in West Africa. The sites are located in the semi-arid Sahel region at approximately 15°North. Both locations are dominated by grasslands and have only limited tree cover. Furthermore, we evaluate the quality of two MODIS LST products, the MOD11A1 1 km data set and the MOD11B1 5/6 km data set for the same sites.

A direct validation based on independent ground mea-

*Corresponding author
Email address: mora@gras.ku.dk (Mads O. Rasmussen)

surements is complicated due to scale issues. Therefore, intercomparisons between products obtained with different retrieval methods from different satellite data are often also used to assess the accuracy of the products. We compare estimates of land surface temperature (LST) based on data from the Meteosat Second Generation (MSG) Spinning Enhanced Visible and Infrared Imager (SEVIRI) sensor and the Aqua/Terra MODIS sensors. Furthermore, the satellite-based LST are validated against ground measurements from the Sahel region of West Africa. It should be noted that validation results generally apply only to a specific set of atmospheric conditions and biomes. Here, we focus on semi-arid West Africa during a short monsoon season.

2. Methods and data

2.1. Planck's law and LST retrieval from field measurements

Remote sensing of LST is based on Planck's law, which relates the radiance emitted by a black body (emissivity=1) to its temperature. However, most natural objects are non-black bodies with $0 < \varepsilon < 1$, where spectral emissivity ε is defined as the ratio between the spectral radiance r emitted by the surface at wavelength λ and the spectral radiance emitted by a black body at the same wavelength and temperature. Therefore, the spectral radiance, r, emitted by a non-black body can be obtained by multiplying Planck's function $B(\lambda, T)$ with ε:

$$r = \varepsilon \cdot B(\lambda, T) = \varepsilon \cdot \frac{c_1 \lambda^{-5}}{\exp\left(c_2/(\lambda T)\right) - 1} \tag{1}$$

where r is in $Wm^{-3}sr^{-1}$, constants $c_1 = 1.1910 \cdot 10^{-16} W m^2 sr^{-1}$ and $c_2 = 1.4388 \cdot 10^{-2} mK$, T is the measured temperature in Kelvin, and λ is in meters.

For a sensor located near the surface and measuring within an atmospheric TIR window, the influence of the atmosphere can be neglected. With known emissivity, the simplified radiative transfer equation (Dash et al., 2002) can be used to account for reflected downwelling TIR radiance from the atmosphere and for the non-black body behaviour of the surface. Therefore, the blackbody equivalent spectral radiance B emitted at temperature T and with spectral emissivity ε is given by:

$$B = \frac{r}{\varepsilon} = \frac{R - (1 - \varepsilon) R_{sky}}{\varepsilon} \tag{2}$$

where R is the *measured* spectral radiance and R_{sky} is sky radiance, which also has to be known, e.g. from measurements. Once B is known, Planck's law can be solved for the temperature T of the surface (see eq. 1).

2.2. LST algorithms for MSG

A number of LST algorithms have been proposed for use with data from the MSG SEVIRI instruments (Madeira, 2002; Sobrino and Romaguera, 2004; Sun and Pinker, 2007; Jiang and Li, 2008; Jiménez-Muñoz and Sobrino, 2008; EUMETSAT et al., 2009; Atitar and Sobrino, 2009). All of them utilise data from at least two channels, namely SEVIRI channels 9 and 10 centred at 10.8 and 12.0 μm, respectively, which are located in the atmospheric window bands where the atmosphere is relatively transparent. The algorithms proposed by Sun and Pinker (2007) further uses information from channel 4 (middle-infrared band centred at 3.9 μm) and channel 7 (thermal infrared band centred at 8.7μm). All of the above mentioned algorithms are split-window algorithms, except Sun and Pinker (2007), although their four-channel algorithm also mainly depends on the same principles as the split-window algorithms. Given information on land surface emissivity and atmospheric water vapour content (W), split-window algorithms use the top of atmosphere brightness temperatures measured in two adjacent bands to correct for the influence of the atmosphere and to derive land surface temperature. For a review of methods for estimating LST and emissivity from passive satellite sensors, readers are referred to Dash et al. (2002).

The LST product produced by the Land Surface Analysis Satellite Applications Facility (LSA-SAF) (EUMETSAT et al., 2009; Madeira, 2002) as well as the algorithm proposed by Jiang and Li (2008) is based on the method developed for the MODIS MOD11A1-product (Wan and Dozier, 1996). This is a generalized version of the algorithm originally proposed for NOAA Advanced Very High Resolution Radiometer (AVHRR) data by Becker and Li (1990). The generalized split-window algorithm used for the LSA-SAF product has different sets of coefficients depending on atmospheric water vapour content and view zenith angle (VZA), as this was found to improve performance. The overall bias was estimated to be 0.05K with a RMSE of 0.78K and with errors increasing with increasing water vapour and Sun Zenith Angle (SZA) (EUMETSAT et al., 2009). The LSA-SAF product also includes a pixel-by-pixel error-estimate and a flag-layer with quality assessment data (Freitas et al., 2010; Trigo et al., 2008a).

For further analysis, in this study a number of algorithms was chosen. These include the LSA-SAF algorithm, based on the generalized split-window algorithm, as well as the alternative algorithms Sobrino and Romaguera (2004); Atitar and Sobrino (2009); Jiménez-Muñoz and Sobrino (2008). The algorithm proposed by Jiménez-Muñoz and Sobrino (2008) was developed for multi-sensor use, and the authors provide coefficients for a number of sensors, including MSG SEVIRI, GOES, MODIS Aqua and Terra, and NOAA AVHRR. This allows to merge and compare data from the different sensors by simply replacing the respective bands and coefficients depending on the sensor used. All investigated algorithms require surface emissivity and water vapour as input data on a pixel-by-pixel ba-

sis. LSA-SAF uses an internal emissivity product based on the "vegetation cover method" (VCM) (Peres and DaCamara, 2005; Trigo et al., 2008b), which assigns emissivities to the soil and canopy fractions of each pixel and scales these according to fractional vegetation cover (FVC). The FVC used by LSA-SAF is a daily updated LSA-SAF product and water vapour is obtained from forecast data from the European Centre for Medium-range Weather Forecasts (ECMWF). All selected algorithms utilise the mean and the difference between the band emissivities, since a study for polar orbiting satellites found that this type of split-window algorithm yields the best performance (Yu et al., 2008).

2.2.1. Emissivity and total column water vapour

All three alternative non-operational SEVIRI LST- products considered in this study require emissivity and water vapour as input. Here, the focus was on methods that are as simple as possible to apply and that allow near-real-time data processing, preferably without relying on external products.

Emissivity was calculated using the VCM method mentioned above (Peres and DaCamara, 2005). The emissivity of a given pixel is calculated as a linear combination of the emissivity of the vegetation and the emissivity of the bare soil, which are both scaled by their relative abundances (as also done for the LSA-SAF product):

$$\varepsilon = \varepsilon_v FVC + \varepsilon_g (1 - FVC) \tag{3}$$

where ε_v is the emissivity of the vegetation, ε_g is the emissivity of the bare soil, and FVC is the fractional vegetation cover of the respective pixel. The emissivities are assigned according to a land cover classification scheme for each of the SEVIRI bands separately. FVC varies with season and is obtained from a relation between FVC and Normalized Difference Vegetation Index (NDVI):

$$FVC = \frac{NDVI_i - NDVI_{min}}{NDVI_{max} - NDVI_{min}} \tag{4}$$

where $NDVI_i$ is the actual NDVI (Tucker, 1979) of the given pixel and $NDVI_{min}$ and $NDVI_{max}$ are the values for bare soil and 100% vegetation cover, respectively (Nishida et al., 2003). This method is sensitive to the chosen values for $NDVI_{min}$ and $NDVI_{max}$, as discussed in detail by Stisen et al. (2007). Furthermore, some authors use a variant of the above equation, where the right hand side of the equation is squared (Carlson and Ripley, 1997; Sobrino et al., 2008) or further modified (Agam et al., 2007). In this study, NDVI was obtained from the MODIS MOD/MYD13A2 level 3, 16-day product and resampled to SEVIRI spatial resolution. In the future, an updated version of the emissivity lookup-tables might be applied (Trigo et al., 2008b) or replaced by a method proposed by Sobrino et al. (2008), which relies on data from the visible part of the spectrum; however, also with these changes the method will be sensitive to the chosen minimum and maximum NDVI values.

For the retrieval of total column water vapour, several direct methods have been suggested for use with MSG SEVIRI data. With two sets of measurements in channels 9 and 10 as input, the methods proposed by Schroedter-Homscheidt et al. (2008); Sobrino and Romaguera (2008) estimate water vapour on a daily basis. By using data from two time slots (with a minimum difference in brightness temperature of 5 and 10 degrees, respectively) the methods avoid the requirement of providing either near-surface air temperature or LST, which is otherwise common. The downside of this is that the water vapour is assumed to be constant between the two measurements, an assumption that does not necessarily hold. Furthermore, due to the required brightness temperature differences these methods only provide one (or only a few) daily estimates of water vapour.

Here, a simpler method was implemented, which only relies on the temperature difference (ΔT) between the two channels and on land surface emissivities. This allows for pixel-by-pixel estimation of water vapour at full 15-min temporal resolution. The method was originally developed for channels 4 and 5 of NOAA-9 AVHRR (Choudhury et al., 1995) and is expressed as a linear relation between ΔT and water vapour (W):

$$\Delta T = \alpha + \beta W \tag{5}$$

where:

$$\alpha = 75\Delta\varepsilon' + (1 - \varepsilon_4) - 0.15 \tag{6}$$

$$\beta = 0.05[1 - 44\Delta\varepsilon' - 5(1 - \varepsilon_4)] \tag{7}$$

$$\Delta\varepsilon' = \frac{(\varepsilon_4 - \varepsilon_5)}{\varepsilon_5} \tag{8}$$

where channels 4 and 5 of NOAA AVHRR only have to be replaced by MSG SEVIRI channels 9 and 10. The coefficients were not re-calculated for SEVIRI; however, due to the similar channel widths and central wavelengths of AVHRR and SEVIRI the error associated with this simplification is assumed to be negligible.

2.3. Tested algorithms

All applied algorithms were proposed by the Global Change Unit, Department of Earth Physics and Thermodynamics at the University of Valencia. The first set of algorithms (referred to as Romaguera) consist of two slightly different algorithms for MSG-1 and MSG-2 both in terms of algorithm and coefficients. For MSG-1, the algorithm is (Sobrino and Romaguera, 2004):

$$\begin{aligned} T_s =& T_{IR10.8} + [3.17 - 0.64\cos\theta](T_{IR10.8} - T_{IR12.0}) \\ &+ \left[-0.05 + \frac{0.157}{\cos\theta} \right](T_{IR10.8} - T^2_{IR12.0}) \\ &+ \left[65 - \frac{4}{\cos^2\theta} \right](1 - \varepsilon) \\ &+ \left[-11.8 + \frac{5.1}{\cos\theta} \right] W(1 - \varepsilon) \end{aligned}$$

$$+\left[-180+\frac{24}{\cos\theta}\right]\Delta\varepsilon$$
$$+[-4+34\cos\theta]W\Delta\varepsilon-0.6 \quad (9)$$

and Atitar and Sobrino (2009) for MSG-2:

$$\begin{aligned}T_s =& T_{IR10.8}+\left[1.34-\frac{0.11}{\cos^2\theta}\right](T_{IR10.8}-T_{IR12.0})\\ &+\left[0.29+\frac{0.08}{\cos^2\theta}\right](T_{IR10.8}-T_{IR12.0}^2)\\ &+\left[60.67-\frac{10.01}{\cos^2\theta}\right](1-\varepsilon)\\ &+\left[-6.71+\frac{2.47}{\cos^2\theta}\right]W(1-\varepsilon)\\ &+\left[-125.91+\frac{15.09}{\cos^2\theta}\right]\Delta\varepsilon\\ &+\left[19.44-\frac{4.27}{\cos^2\theta}\right]W\Delta\varepsilon\\ &+\left[-0.44+\frac{0.57}{\cos^2\theta}\right] \quad (10)\end{aligned}$$

where $T_{IR10.8}$ and $T_{IR12.0}$ are the brightness temperatures of split-window channels 9 and 10, θ is the view zenith angle, W is the total column water vapour content, ε is the mean emissivity, and $\Delta\varepsilon$ is the difference between the two channel emissivities.

The third algorithm is referred to as "Munoz" and was proposed by Jiménez-Muñoz and Sobrino (2008), who published the coefficients for a number of low-resolution thermal infrared sensors including MSG SEVIRI, MODIS, and the NOAA AVHRR:

$$\begin{aligned}T_s =& T_i+c_1(T_i-T_j)+c_2(T_i-T_j)^2+c_0\\ &+(c_3+c_4W)(1-\varepsilon)+(c_5+c_6W)\Delta\varepsilon \quad (11)\end{aligned}$$

where T_i and T_j are the brightness temperatures of the two split window channels, and c_0 - c_6 are fitted coefficients for the MSG SEVIRI sensors (see table 1).

2.4. Study period

The study period is from June 1st (doy 152) to October 31st (doy 304) 2009 and covers 153 days. During most of this period MSG-2 (located at 0.0°) was the operational satellite, but during the period from 2009-08-15 14:00 until 2009-08-21 07:45, MSG-1 (located at 9.5°East) was the operational satellite. The SEVIRI-sensor scans the earth disk every 15 minutes in 12 spectral channels, resulting in 96 daily image slots per channel. For the study period 99.62% (14632 out of 14688) of all potential slots and 96.86% (14227 out of 14688) LSA-SAF LST slots were available for analysis.

2.5. Cloud masking

Two different cloud masks were considered in this study:

- MPEF CLMK (CLMK) from the EUMETSAT Applications Ground Segment, which comprises a Meteorological Products Extraction Facility (MPEF).
- SAF-NWC from the Satellite Application Facility for supporting NoWCasting and very short range forecasting (will be referred to as SAF CLMK) (Derrien and Gleau, 2005).

The former is distributed real-time along with the HRIT-data from EUMETSAT via EumetCast, while the SAF-NWC is distributed as an integral part of the LSA-SAF LST product.

2.6. MODIS LST products

LST estimates derived from MODIS data are widely used and are some of the most extensively validated products. The following two products are considered:

- MOD11A1: 1 km (full resolution) product based on the generalized split-window algorithm described above (Wan and Dozier, 1996).
- MOD11B1: 5/6 km product based on the "day/night algorithm" and, depending on version, has a spatial resolution of 5 km (V4.1) and 6 km (V5.0) (Wan and Li, 1997).

Both products are distributed in different versions. We have considered version 4.1 and version 5 (latest version) in this study. The two MODIS EOS missions Terra and Aqua provide up to four daily estimates of LST with local overpass times at approximately 10:30 and 02:00 (both AM and PM), respectively.

The MOD11B1 product uses a different type of algorithm to the split-window algorithms discussed above. It is based on one day and one night observation in 7 of the MODIS bands from which land surface emissivity and temperature are retrieved simultaneously; for more details, interested readers are referred to the original paper by Wan and Li (1997). As the resolution of the MOD11B1 product more or less matches the nominal spatial resolution of the SEVIRI sensor (4.8 km at nadir) and because it provides an independent LST estimate based on more bands and uses a different retrieval approach, we decided to include both MODIS LST products in the analysis.

2.7. Considerations on scale

This study considers satellite data at three different spatial scales, namely the 3 km MSG SEVIRI data (the actual field of view is approximately 4.8 km (Schmetz et al., 2002)), and the 1 km and 5/6 km MODIS data. These are compared to in situ data which are measured on a much smaller spatial scale (order of 10 m). Furthermore, the satellite data are influenced by inaccuracies in geo-rectification. The quoted accuracy for MSG-1 and MSG-2 is 0.4 pixel or 1.2 km (Eumetsat, 2007). In order to mitigate potential geo-rectification issues, it was decided to

Table 1: MSG SEVIRI coefficients for the Munoz-algorithm. Source: Jiménez-Muñoz and Sobrino (2008)

	$\lambda_i;\lambda_j$ [m]	c_0 [K]	c_1 [-]	c_2 [K^{-1}]	c_3 [K]	c_4 [K cm^2 g^{-1}]	c_5 [K]	c_6 [K cm^2 g^{-1}]
MSG-1	10.79;11.94	0.006	1.736	0.297	45.3	-0.97	-147	18.3
MSG-2	10.78;11.99	-0.021	1.503	0.273	44.2	-0.58	-135	16.7

use a 3x3 window of SEVIRI data for comparisons with in situ data. Although this increases the (nominal) SEVIRI foot-print from 3 x 3 km^2 to 9 x 9 km^2, the averaged values will be more stable than the values from single pixels. For the MOD11A1 1 km product, a 9 x 9 pixel window was chosen to match the 9 x 9 km^2 window size of the SEVIRI-data. For the coarser MOD11B1 product, a 2 x 2 km^2 window was chosen, although the ground area covered is, thus, slightly larger at 10 x 10 km^2 (or 12 x 12 km^2 for V5.0 data). This requires large homogenous areas to be used as study sites for the in situ measurements, which is the case for the two sites used in this study (which will be introduced below).

Using a pixel window instead of a single pixel also allows for deriving statistics for the temperature variation within the window. In all cases, data were only considered if at least two pixel values were available within the window, and a threshold was applied on the maximum standard deviation allowed for a given time slot to be included in the analysis (depending on window size and data type).

2.8. Field sites and instrumentation

In situ data from two field sites are used in this study for comparison with satellite data. The two sites are both located within the Sahel zone in semi-arid West Africa (see fig. 1 for locations). The sites are located in large relatively homogenous areas, which is required for comparisons with data from moderate and coarse resolution satellite sensors. At the two sites, Dahra, Senegal and Agoufou, Mali, tree cover is sparse (about 3-4 %) and the ground cover is dominated by annual grasses. The land use is predominantly rangeland used as browsing areas for animals, although some agricultural areas are present at the Dahra site.

2.8.1. Dahra, Senegal

The field site is located north-east of the town of Dahra in northern Senegal in West-Africa and consists of two towers for validating satellite products Stisen et al. (2008b); Fensholt and Sandholt (2005). The towers are equipped with instruments for validating satellite products in the visible, near-infrared, and the thermal domain. The field site is hosted by the Centre de Recherches Zootechniques de Dahra, Institut Sénégalais de Recherches Agricoles (ISRA). Annual mean precipitation is approximately 370mm (1960-2007), but with considerable inter-annual variation. The growing season is relatively short, lasts normally less than 100 days and occurs between July and October. The area around the towers is used as grazing land for the zoological research station, but also as farmland. The soil is sandy and reddish in colour and has been classified as an Arenosol (Batjes, 2001). The surface cover is dominated by annual grasses and the tree crown cover (TCC) around the site was determined by (Rasmussen et al., 2010a) to be around 4%. The trees are scattered in the landscape, either as isolated trees or as small clumps. In some cases the distribution of the bushes and trees follows ancient dunes, which causes stripes of high vegetation - hence the name "tiger bush". Due to the strong natural seasonality of the region, grass is usually desiccated from October to April, whereas the trees are usually green throughout year. During the rainy season the grass grows high (about 1m) and dense and the entire site is covered by vegetation.

2.8.2. Agoufou, Mali

The Agoufou site (15.3N, 1.5W) is located in Mali in the Gourma region which stretches from the loop of the Niger River southward down to the Burkina-Faso border. It is part of the African Monsoon Multidisciplinary Analysis (AMMA) - Couplage de l'Atmosphere Tropicale et du Cycle Hydrologique (CATCH) Observatory in West-Africa. The Agoufou site, close to the small town of Hombori (373 mm long term rainfall average), is set on a homogeneous 3 x 3 km fixed dune system that is representative of the most common situation in Central Sahel.

The vegetation at Agoufou is typical of mid-Sahel sandy soil vegetation with a herbaceous layer almost exclusively composed of annual species, and scattered trees and shrubs. Tree cover is 3.1 % (Hiernaux et al., 2009). Surface energy budget, soil moisture and vegetation growth are markedly shaped by the alternation of a long dry season and a short rain season. The rapid germination and growth of the annual vegetation is a prime example of such a sharp cycle. Annuals germinate after the first rains, in June or July and unless the plants wilted before maturity by lack of rain, the senescence matches approximately with the end of the rainy season. Herbaceous yield is largely determined by the duration and soil moisture condition of that period. In turn, the rapid plant growth greatly impacts the land surface properties like the energy balance and fluxes.
More details about the Agoufou site and the AMMA- CATCH observatory in Mali can be found in Mougin et al. (2009).

2.9. Instrumentation at the field sites

The sensor configuration for validating LST at the Dahra site consists of four "KT-15.85 IIP" IR-radiometers (self-calibrating, chopped radiometers, Heitronics GmbH). The

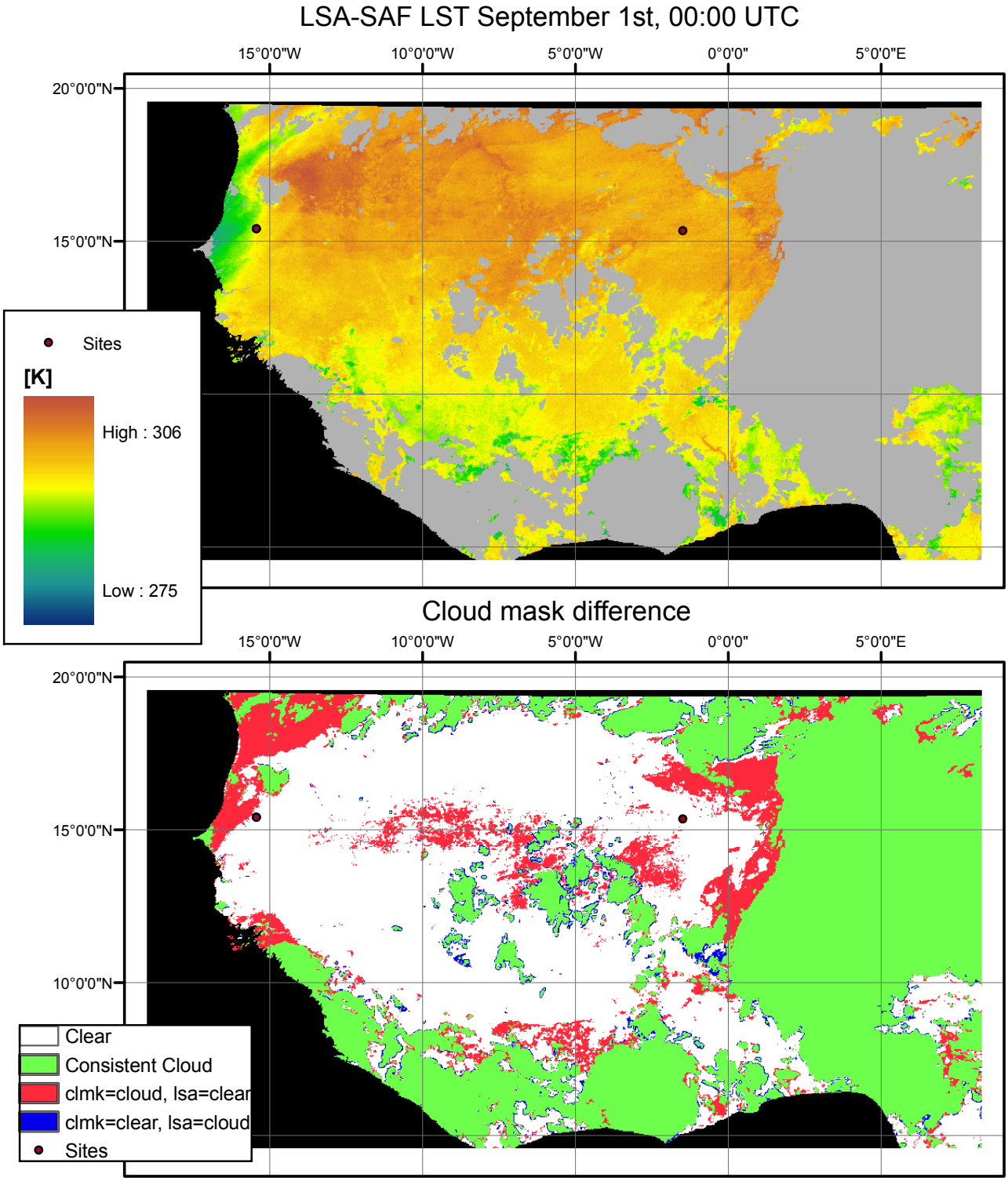

Figure 1: Top: An example of the LSA-SAF LST product for 2009/07/01 at 00:00. Bottom: The difference between the cloud masks for the same time. In the legend for the bottom part, CLMK denotes the MPEF CLMK, while LSA-SAF denotes the SAF-CLMK.

KT-15 measure IR radiance between 9.6μm and 11.5μm and express the results as brightness temperatures (BT) with standard deviation 0.25°C plus 0.35% of the difference between target and housing temperature. Three of the KT-15 point towards targets representing different components of the land surface, while the fourth KT-15 measures downwelling longwave radiance from the atmosphere at 53° with relation to zenith and points northwards. The targets observed by the three surface facing KT-15 are a patch of grass / soil, which is sunlit over the entire course of the day, a patch of grass / soil which is shaded during the day with the exception of early morning and late afternoon, and a canopy of a *Acacia raddiana* tree from south west. The 53° zenith angle of the sky-facing sensor yields measurements which are representative for the hemispherical downwelling longwave radiation (Kondratyev, 1969). Due to the small distance between the radiometers and the surface, atmospheric attenuation of the surface-leaving IR radiation is negligible. However, the measurements of the KT-15 observing the surface contain radiance emitted by the surface (i.e. the target signal) as well as reflected downwelling IR radiance from the atmosphere: this is corrected for using the measurements from the sky-facing sensor. Depending on target emissivity and on downwelling longwave radiance (e.g. a cold clear sky vs. a warm humid atmosphere), the reflected component can cause differences of several degrees Kelvin (Schädlich et al., 2001). All corrections for the reflected component in the measurements are performed at KT-15's centre wavelength of 10.55μm.

At Agoufou, the site is equipped with a IRTS-P instrument from Apogee Instruments. It is a type-K thermocouple sensor measuring in the spectral region between 6 and 14 μm region with an accuracy of $\pm$ 0.3 K. It has a relatively wide field of view; 25°half-angle for 90% of the signal equalling a 1 m FOV at the mounting height of 3 m. The sensor is measuring a patch of grass which is sunlit throughout the day. Since no measurements of the downwelling longwave radiation in a similar spectral band were available, no corrections of the reflected TIR component were performed. Considering the wide spectral region measured by this instrument, this could lead to significant errors in the measured temperatures (on the order of a couple of K) especially for cases with high concentrations of water vapour in the atmosphere.

For a derivation of LST from brightness temperature measurements the emissivities of the surface components have to be known, e.g. the emissivities of the soil background and of the grass and tree vegetation. At both sites, Dahra and Agoufou, trees stay green throughout the year and show only little temporal variation. Consequently, the seasonal change of emissivity for spatially coarse satellite pixels corresponds largely to the NDVI-curve of the grass and closely reflects the variation of moisture in the top soil layer during the rainy season. Emissivities for Dahra and Agoufou were determined once per day using the FVC approach (eq. 3 and 4) and for both sites the data were corrected for emissivity as described by equation 2. For Dahra, where also the downwelling longwave radiance R_{sky} is measured, the data were additionally corrected for the reflected R_{sky} component.

In terms of atmospheric correction of TIR satellite data both sites are challenging since they have low elevations a.s.l., which results in long atmospheric paths. The atmospheric water vapour load varies strongly between rainy and dry season and especially during the warm (about 40°C) and humid (up to 90 % relative humidity) rainy season the atmospheric correction is challenging. Furthermore, occasional outbreaks of Sahara dust complicate cloud detection.

3. Results and discussion

3.1. Regional scale comparison between LST products

The LSA-SAF, the Munoz, and the Romaguera-products were investigated by comparing them over the entire time series. This was done by pair-wise correlating all those LST products for each time slot within a subset, for which all products were classified as cloud-free land surface pixels. The chosen subset covers sub-Saharan West-Africa at a size of 1000 x 550 pixels with 3 kilometres spatial resolution of the data grid; 79% of the pixels in this subset are land pixels, see fig. 1 top. Taking into account the two different cloud masks and that the LSA-SAF product is only delivered with cloud mask applied, this means that the LSA-SAF product can not be compared to the CLMK-masked data. Therefore, four different pairs of data to can be investigated:

1. LSA-SAF LST vs Munoz (LSA-SAF cloud mask).
2. LSA-SAF LST vs Romaguera/Atitar (LSA-SAF cloud mask).
3. Munoz vs Romaguera/Atitar (LSA-SAF cloud mask).
4. Munoz vs Romaguera/Atitar (CLMK cloud mask).

The results are highly consistent during the study period and, therefore, only a limited number of days are shown in fig. 2 (top panel). The two alternative products Munoz and Romaguera are very similar and, with almost no exceptions, show r^2-values above 0.95. A slight diurnal pattern is present with highest correlation during daytime. The correlation between the two products and the LSA-SAF product is also practically indifferent to the cloud mask applied. In contrast, the correlation between the Munoz and Romaguera products and the LSA-SAF-product is weaker and shows a distinct diurnal variation. The strongest correlation is observed around noon, when the r^2-values are generally above 0.8 and in most cases exceed 0.9 for both products. During nighttime, correlation is much weaker with typical r^2-values between 0.6 and 0.7. Compared to the Romaguera-product, the Munoz-product is consistently stronger correlated to the LSA-SAF-product during daytime. The opposite is true during night-time. A diurnal pattern is also present in the difference between the number of available land pixels for

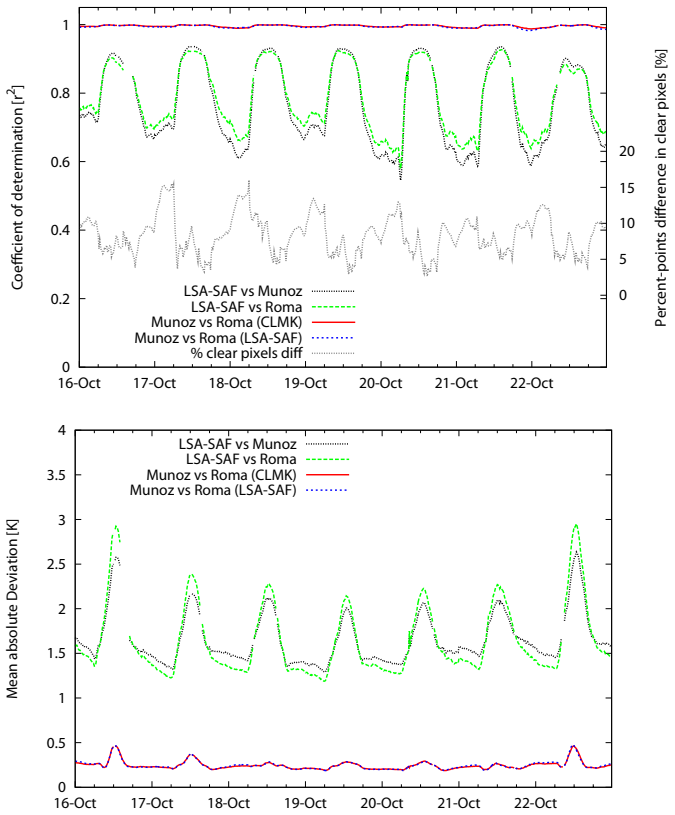

Figure 2: Top: A time series of r^2 values for a week in October for a pair-wise comparison between the LST-products. Also shown (in grey, right hand scale) the difference in cloud-free land pixels between the two cloud masks in percent (computed as SAF CLMK minus MPEF CLMK). Bottom: the Mean Absolute Deviation (MAE) for the four time series shown above calculated pairwise.

the two cloud masks (calculated as % clear land pixels in the LSA-SAF mask minus the corresponding % of clear land pixels in the CLMK-product), although it is not a relatively smooth diurnal curve like for the coefficient of determination. The maximum in the difference between the two cloud masks generally occurs around 6 am, after which the difference reduces rapidly and starts to increase slowly with a dip in the late afternoon in many cases. The LSA-SAF mask consistently has more clear pixels than the CLMK mask. Fig. 2, bottom shows the mean absolute error between the four pairs, and diurnal variations matching the patterns in the correlation. Typical differences between the two alternative products are between 0.2 and 0.5 K, while typical values for the comparison with the LSA-SAF is 1.5 K during nighttime and 2-3 K during daytime.

3.2. Point validation of LST products

3.2.1. MSG-based LST products

The LSA-SAF LST and the two alternative LST products were compared to in situ measurements from the Dahra, Senegal, and Agoufou, Mali, sites. For the two alternative products, the version masked with the SAF CLMK cloud mask and the version masked with the MPEF CLMK cloud mask were investigated separately. The statistics of the comparisons for the five products are summarised by month in table 2 for the entire study period for the two sites.

A general observation in these comparisons is that there are large biases in most cases, with the exception of October. Looking at the data month by month reveals that in terms of coefficient of determination the performance is generally worst in August and September, while June and July have the largest biases. Despite the quite different locations of the two sites, and the differences in instruments and corrections carried out, the overall patterns for the two sites are very alike for all five LST products.

For the Dahra site, the LSA-SAF product has biases between -1.90 and -6.86 degrees, with a mean bias for the entire study period of -5.30 degrees. The corresponding r^2-values vary between 0.60 (for September) and 0.96 (for October) and, thus, follow the general pattern well. For all months except October, the bias exceeds 5 degrees and the r^2-values do not exceed 0.82. The poor performance especially for August and September is also reflected by slopes around 0.6 and offsets exceeding 100 K. At Agoufou, the performance is generally slightly better both in terms of bias and r^2-values. The results for both locations are discouraging in terms of biases and correlation, as they by far exceed the expected uncertainties of the LSA-SAF product, which is given by the accompanying "errorbar" product. Scatter plots between in situ LST and LSA-SAF LST for the entire study period and per month for Dahra are shown in fig. 3 and for Agoufou in fig. 4.

In order to check the indication that the performance of the products improves towards the end of the study period, we analysed data until November 12th for Dahra. The time series for October was also investigated and an apparent change in performance around October 11th 2009 was found. For the period from October 11th to November 12th a comparison with the in situ data yielded more encouraging results (see fig. 5): the r^2-value increased to 0.98, the bias reduced to less than one K and the slope was close to 1. This clearly indicates that after the end of the rainy season the LSA-SAF performs excellently at Dahra.

Comparing the LSA-SAF product to the two alternative sets of products investigated here yields mixed results (see table 2). In terms of biases and r^2-values the MPEF CLMK-versions of the algorithms out-perform the LSA-SAF algorithm. On the other hand, the slopes obtained for the LSA-SAF LST are generally closer to unity, i.e. the relationship is closer to the 1:1 line than for the other products. When comparing the LSA-SAF LST to the alternative products with the SAF CLMK cloud mask (which is a fairer comparison), only the biases are consistently lower for the alternative products while the other measures are better for the LSA-SAF product.

The performance of the Munoz and the Romaguera products (table 2) is very similar, both, in terms of coefficient of determination and in terms of biases. For Agoufou, the Munoz-algorithm performs slightly better, but the dif-

Table 2: Statistics on the comparison between the in situ data and the different LST-algorithms and cloud masks for the two sites.

Dahra							**Agoufou**						
LSA-SAF	**overall**	**jun**	**jul**	**aug**	**sep**	**oct**	**LSA-SAF**	**overall**	**jun**	**jul**	**aug**	**sep**	**oct**
bias	-5.30	-6.74	-6.83	-6.86	-5.06	-1.90	bias	-4.98	-7.62	-6.21	-3.85	-4.17	-2.79
slope	0.80	0.78	0.80	0.59	0.63	1.06	slope	0.83	0.82	0.94	0.84	0.80	0.90
offset	56.32	61.42	56.77	117.94	106.48	-19.89	offset	47.78	48.25	13.58	43.85	57.32	28.84
r^2	0.78	0.78	0.82	0.73	0.60	0.96	r^2	0.83	0.84	0.82	0.74	0.82	0.96
munoz (MPEF)	**overall**	**jun**	**jul**	**aug**	**sep**	**oct**	**munoz (MPEF)**	**overall**	**jun**	**jul**	**aug**	**sep**	**oct**
bias	-4.14	-5.88	-5.52	-4.94	-3.26	-1.73	bias	-4.30	-6.76	-5.16	-2.77	-3.51	-2.79
slope	0.73	0.74	0.68	0.55	0.65	1.01	slope	0.80	0.77	0.82	0.82	0.73	0.91
offset	78.12	76.02	92.68	131.56	102.60	-5.72	offset	57.67	63.52	48.62	51.67	78.46	24.84
r^2	0.79	0.79	0.79	0.76	0.80	0.95	r^2	0.85	0.86	0.84	0.79	0.83	0.96
munoz (SAF)	**overall**	**jun**	**jul**	**aug**	**sep**	**oct**	**munoz (SAF)**	**overall**	**jun**	**jul**	**aug**	**sep**	**oct**
bias	-4.72	-6.57	-5.98	-5.62	-4.37	-1.87	bias	-4.81	-7.35	-5.87	-3.36	-3.75	-2.82
slope	0.71	0.72	0.66	0.56	0.55	1.01	slope	0.77	0.72	0.82	0.84	0.72	0.91
offset	85.32	78.91	98.08	129.19	132.70	-4.54	offset	64.88	79.16	50.42	45.73	83.03	24.07
r^2	0.73	0.75	0.76	0.65	0.53	0.94	r^2	0.80	0.82	0.77	0.76	0.76	0.96
roma (MPEF)	**overall**	**jun**	**jul**	**aug**	**sep**	**oct**	**roma (MPEF)**	**overall**	**jun**	**jul**	**aug**	**sep**	**oct**
bias	-4.11	-5.95	-5.41	-4.81	-3.33	-1.77	bias	-4.49	-6.81	-5.28	-3.23	-3.71	-2.88
slope	0.72	0.72	0.66	0.52	0.66	1.00	slope	0.79	0.75	0.80	0.82	0.73	0.90
offset	80.49	81.43	98.28	140.57	101.24	-2.74	offset	61.21	69.79	54.93	50.23	80.06	29.00
r^2	0.78	0.78	0.76	0.68	0.81	0.95	r^2	0.85	0.87	0.83	0.80	0.83	0.96
roma (SAF)	**overall**	**jun**	**jul**	**aug**	**sep**	**oct**	**roma (SAF)**	**overall**	**jun**	**jul**	**aug**	**sep**	**oct**
bias	-4.73	-6.64	-5.96	-5.67	-4.39	-1.90	bias	-5.01	-7.41	-5.98	-3.78	-3.93	-2.97
slope	0.70	0.71	0.65	0.46	0.55	1.00	slope	0.76	0.70	0.79	0.83	0.71	0.90
offset	88.28	84.54	101.88	160.49	131.71	-3.31	offset	69.12	84.74	56.99	49.13	85.13	28.24
r^2	0.71	0.74	0.72	0.54	0.53	0.94	r^2	0.80	0.82	0.76	0.77	0.76	0.95

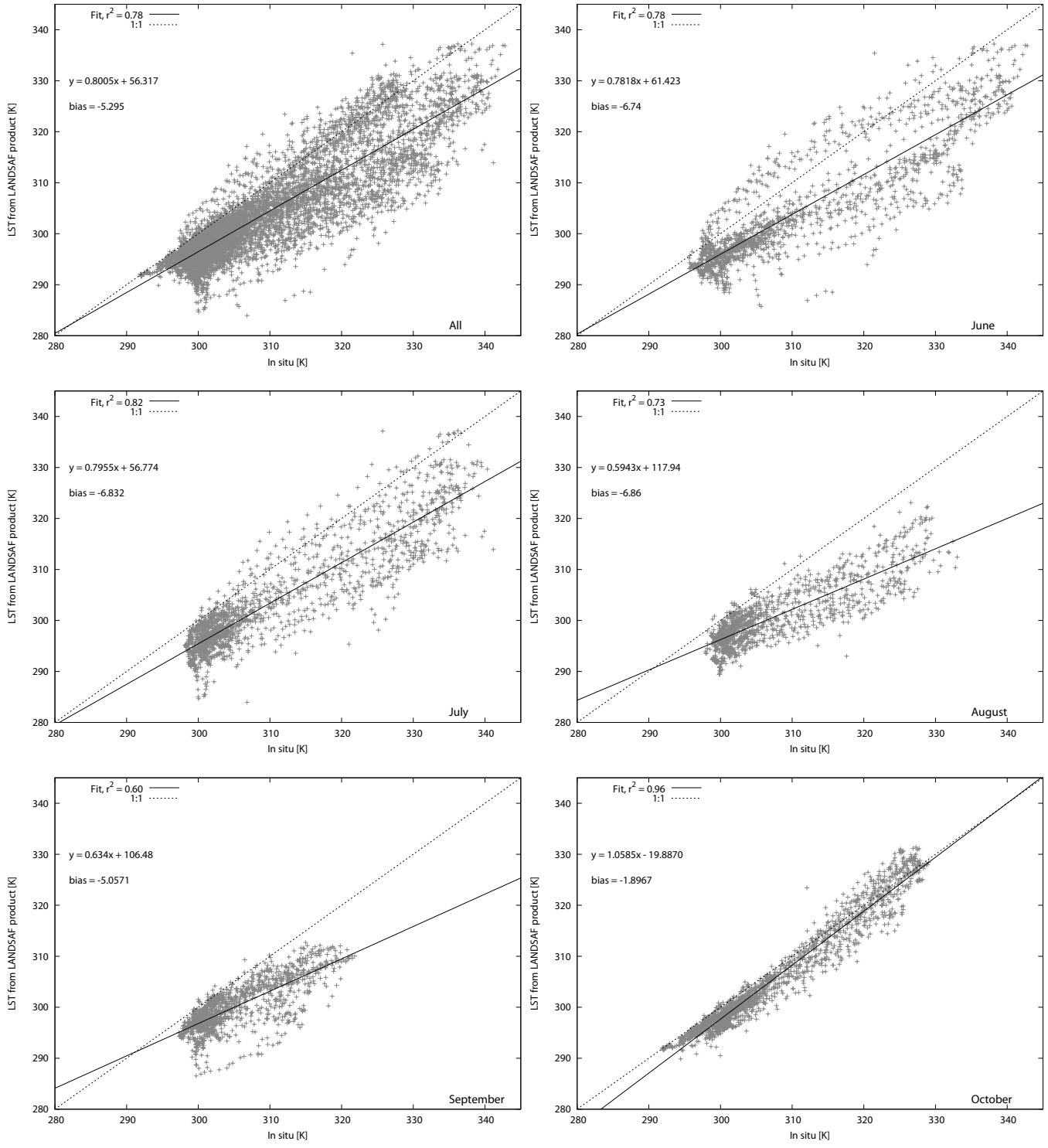

Figure 3: Scatterplot of LSA-SAF LST against in situ measurements for the Dahra, Senegal site. The top left plot shows the data for the entire study period, whereas the other plots show the data for the 5 separate months.

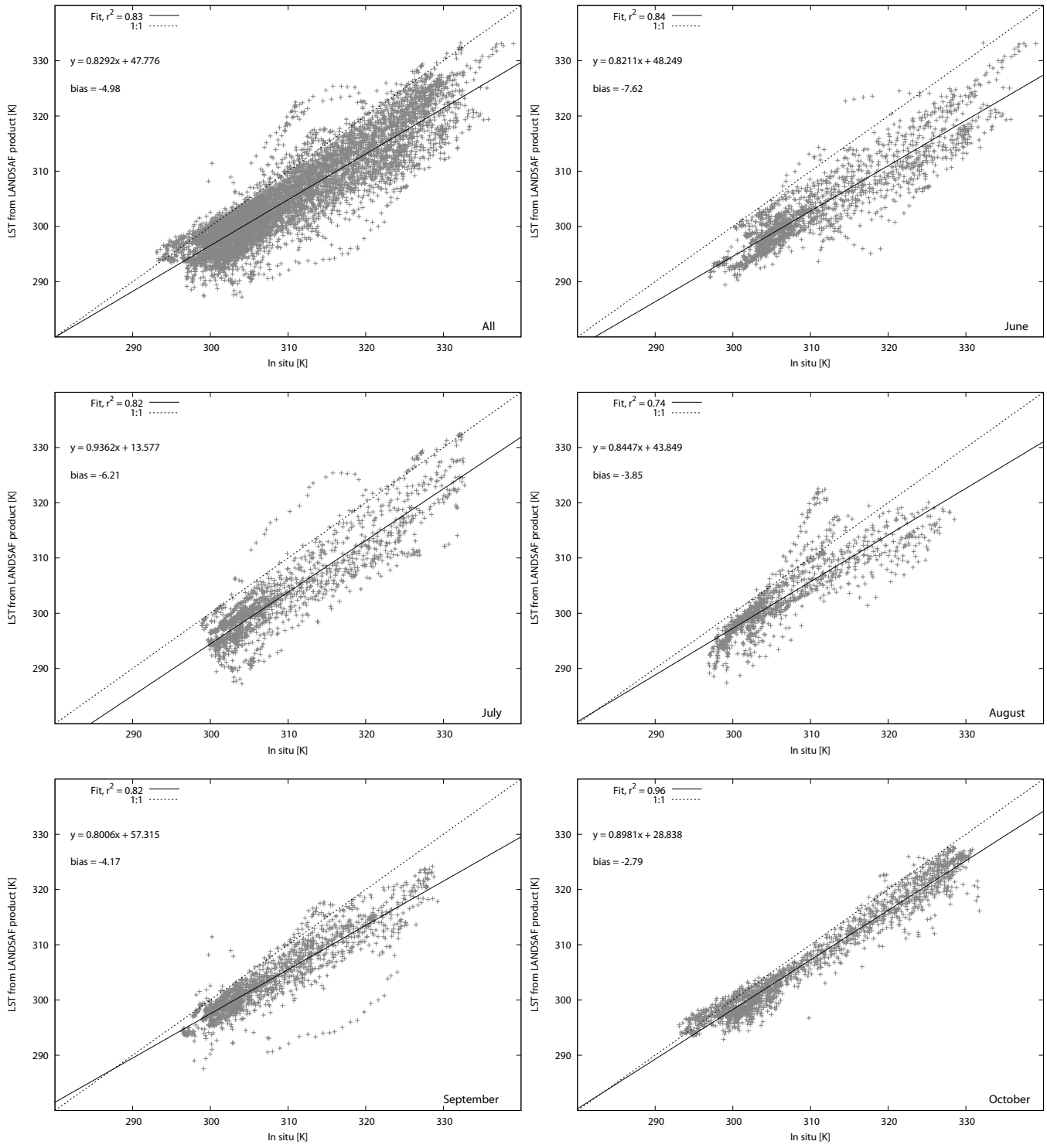

Figure 4: As fig. 3 but for the Agoufou, Mali site.

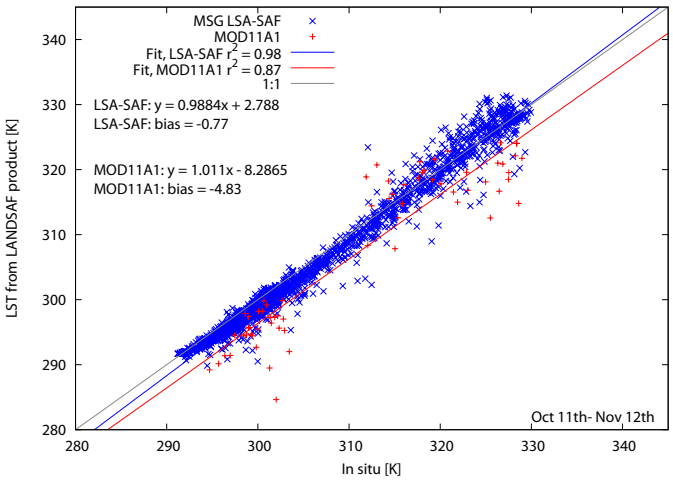

Figure 5: Dahra. Similar to the plots in fig. 3 but only including data between 11-10-2009 and 12-11-2009.

ferences are small. For Dahra, there is almost no difference for the datasets using the MPEF CLMK-mask, while Munoz perform slightly better for the datasets using the SAF CLMK mask. Therefore, based on this analysis, there is a slight preference for the Munoz algorithm.

In terms of the cloud mask, the statistics are generally better for the MPEF CLMK data than for the data masked with the SAF CLMK cloud mask. The bias is lower and r^2-values are better or equal in all cases. Only for the slope, the SAF CLMK out-performs the MPEF CLMK for a few cases of the Munoz and Roma LST-products. The main reason for the better performance of the MPEF CLMK could be that it masks out significantly more pixels than the SAF CLMK. For the entire 5 months analysed here, on average 46.44% of the land pixels in the LSA-SAF product are marked cloud-free, while for the MPEF CLMK-mask only 35.44% are classified as cloud-free. An example of this is given in fig. 1 bottom panel where the difference between the two cloud masks is shown. Several large areas are present where the MPEF CLMK mask indicates clouds, while the SAF CLMK marks the same areas cloud-free. The opposite case, where SAF CLMK masks out pixels that are clear according to the MPEF CMLK-product, usually occurs along cloud-edges where the LSA-SAF is generally more conservative. This is seen as a seam of pixels (in blue) around many of the big cloud-areas in fig. 1, bottom. Differences between the two cloud masks can also be seen on the western-most part of Africa along the Senegalese coast. As can be seen from the LSA-SAF temperatures, the area has relatively low temperatures compared to the area just a little further inland. This area is identified as cloud in the MPEF CLMK, while the SAF CLMK classified it as clear. Other examples occur in the southern part of the subset, just north of a larger area identified as cloud by both products. Here, smaller areas with significantly lower temperatures are identified as clouds in the MPEF CLMK-product, while SAF CLMK identifies them as clear.

It is striking how similar the monthly correlation patterns for the two sites are when comparing fig. 3 and fig. 4. Almost month by month, the slope and the shape of the point-clouds for the Dahra and Agoufou sites match. Overall, the scatter is larger for Dahra and for August and September the range of temperatures is smaller. Despite these differences, the main features are very similar for the two sites, indicating that the correlations are controlled by similar factors. This can be explained by the fact that the two sites are located at approximately the same latitude and, therefore, the onset of the African monsoon is also similar. The monsoon is the main factor controlling the content of atmospheric water vapour, but aerosol optical depth generally does not increase during this period (Ogunjobi et al., 2008). The low correlations for both sites coincide with the monsoon season and indicate problems of the LST retrieval algorithms.

Fig. 6 shows two examples of the diurnal variation in the in situ LST as well as the satellite-based estimates from the MSG LSA-SAF product and the MOD11A1-product representative of a monsoon-case (top) and dry-season case (bottom). The first part of October shows an almost consistent underestimation by the LSA-SAF product compared to the in situ data, although one day (October 2nd) shows the opposite case. The observed offset is similar in magnitude to the bias found in the comparison of the two products. In several cases, e.g. on October 4th and 5th and on October 8th, LSA-SAF underestimates LST dramatically: this could be explained by undetected clouds. The in situ data on the 8th also indicate some cloud cover during the afternoon with a small dip followed by a spike. This underestimation leads to large temperature differences between in situ and LSA-SAF LST (in blue, right scale) and in some cases exceeds 15 K. For the second period shown in fig. 6 bottom, the match between in situ data and LSA-SAF LST is significantly better, with some almost perfectly matching days near the end of the period. However, the first day (Oct. 22nd) and a few other days also show signs of undetected clouds in the LSA-SAF data, which causes larger discrepancies between the two LST estimates.

For both sites, there are some days for which the LST in the plots (fig. 3 and 4) are distinctive lines or trajectories. One of the most obvious examples occurs in July at the Agoufou site, where a series of points is clearly visible above the main point-cloud. These indicate a large overestimation of LST in the LSA-SAF product or an underestimation in the in situ LST. Other such events can be identified during most months for Agoufou, while for Dahra these occur mostly during the two first months. The trajectories could at least be partly caused by local phenomena that do not effect larger parts of the total 9 x 9 km^2 area, e.g. local precipitation events, which have a pronounced effect on the in situ measurements, but not on the satellite data.

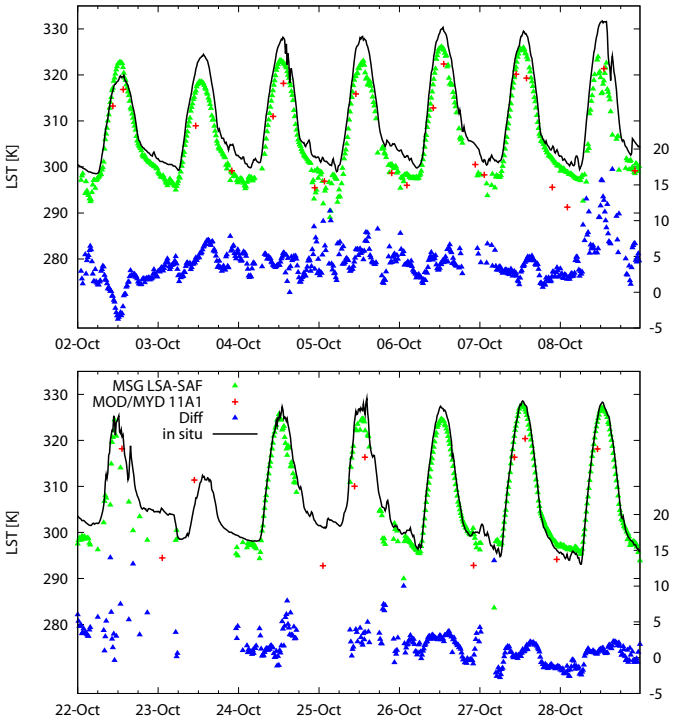

Figure 6: The diurnal variation in the in situ data, the LSA-SAF LST, the MOD11A1 LST, and the difference between in situ and LSA-SAF (in blue, right hand scale) for two periods in October for the Agoufou site. The two cases are representative of the monsoon-season (top) and the dry-season (bottom), respectively.

3.2.2. MODIS LST products

We compared the LST-estimates from MODIS MOD11A1 (1 km) and MOD11B1 (5/6 km) products with in situ measurements. MODIS LST products are currently the best operationally available alternative to MSG-data and provide up to four daily estimates of LST (for most areas) at moderate or coarse resolution. However, with four LST values per day the retrieval of diurnal LST variation is incomplete and, due to the fixed timing of the satellite overpasses, there is no guarantee that the full temperature range is monitored. The two MODIS products are considered here because they use algorithms that are based on different assumptions and, thus, provide to different LST-estimates that can be assessed.

If all cases with simultaneously available in situ and MODIS LST are considered, correlation coefficients between 0.6 and 0.8 are obtained. However, the correlation mainly reflects the similar temperature ranges of the MODIS observations and the in situ data, but individual estimates do not match well. In fig. 7 and 8 the correlations are shown by platform (Terra/Aqua) and by overpass (day/night) for the MOD11A1 (top) and the MOD11B1 (bottom) product.

Performance of the MOD11A1 and MOD11B1 is similar for both sites. When considering the data for each sensor overpass separately, in most cases there is hardly any correlation between in situ data and MODIS estimates.

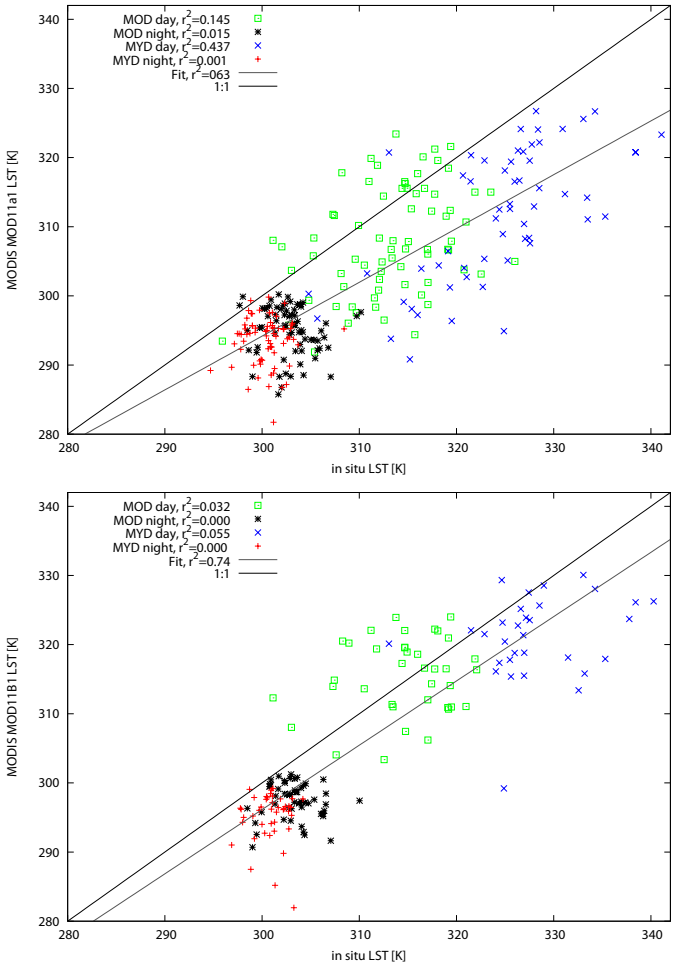

Figure 7: Scatterplot of in situ versus the MODIS MOD11A1 (top) and MOD11B1 (bottom) products for the Dahra-site. MOD represents data from the MODIS Terra sensor and MYD data from the MODIS Aqua sensor.

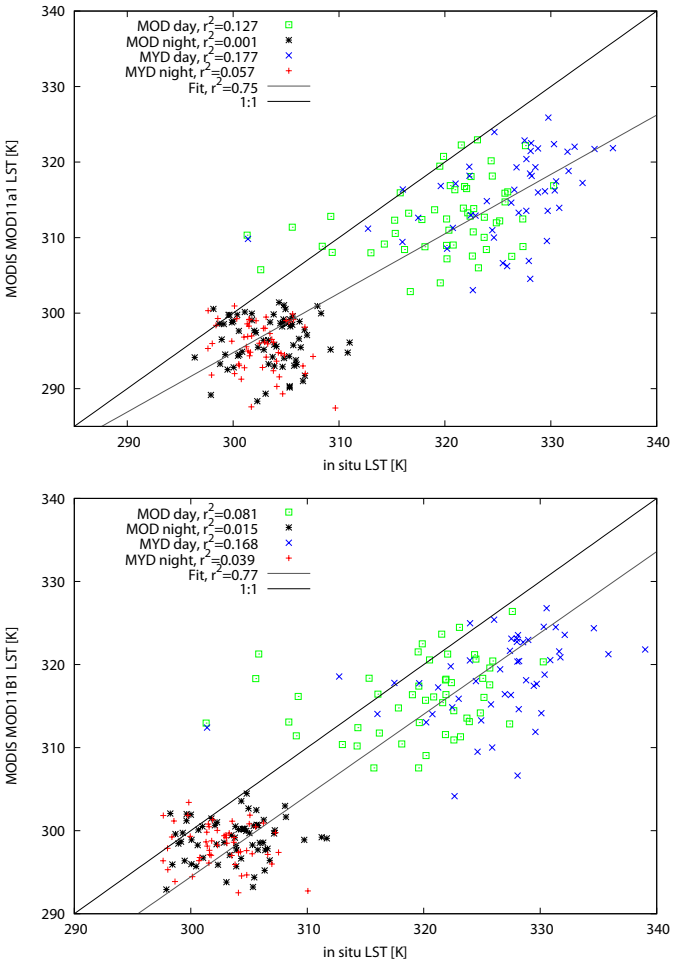

Figure 8: Scatterplot of in situ versus MODIS MOD11A1 (top) and MOD11B1 (bottom) products for the Agoufou-site.

Despite that, the r^2-values are similar for the MOD11A1 and the MOD11B1 product, while slopes and offsets are closer to their ideal values (1.0 and 0.0, respectively) for the coarser MOD11B1 product. The slopes are very close to unity for MOD11B1, but still with a significant bias while the slopes for MOD11A1 are lower at around 0.7. Only the day overpass of the MODIS Aqua sensor shows a slight tendency for a consistent positive correlation. The Aqua sensor day pass takes place around 2:00 pm which is usually close to the time of maximum temperature due to the solar heating of the surface. This can be seen in figures 7 and 8 where the Aqua day overpass generally show the highest temperatures. As for SEVIRI, the match between in situ data and satellite measurements improves towards the end of the study period. Therefore, we extended the time series "after the monsoon" for the Dahra-site from October 11th to November 12th and plotted the MODIS data against the respective in situ LST (see fig. 5). When comparing the results to those for the June to October data shown in fig. 7 top, the fit has improved notably, the regression is now close to the 1:1 line, and the coefficient of determination increased to 0.87.

In order to investigate if there is a dependence on the view zenith angle (VZA), which was observed in previous studies Trigo et al. (2008c), we plotted the differences between in situ LST and MOD11B1 LST against MODIS VZA (see fig. 9). Although fig. 9 is dominated by scatter, there is a slight tendency towards larger differences with increasing VZA, which is highlighted by the fitted second order polynomials. It is also noticeable that the differences between in situ data and MOD11B1-values are largest for Aqua afternoon overpasses. This can be explained by the fact that the highest temperatures are found during the afternoon hours when the different surface components (e.g. bare soil and vegetation) have the largest differences in temperature; combined with the high range of MODIS VZA this leads to the directional effects identified by Trigo et al. (2008b); Pinheiro et al. (2004, 2006). These effects occur as the illumination and viewing geometries change with overpass, which exposes different fractions of sunlit and shaded parts of the surface components to the sensor. As the sunlit parts are generally warmer than the shaded parts, the geometry of the overpass influences the temperature estimates.

One of the most noticeable features is the difference in the number of good observations between MOD11A1 and MOD11B1 in the favour of the former. Interestingly, there is also a difference in data availability for MOD11A1 product version 5 (currently the latest version) and version 4.1: for Agoufou, 271 matches between in situ data and version 5 data were found, but only 188 matches for version 4.1 (and the in situ data series is almost complete). Compared to a potential number of matches which just exceeds 600, this difference is significant. For the coarser MOD11B1 product 164 values were available (version 4.1) for the same period, which is only slightly more than a quarter of the potential values and on average just above

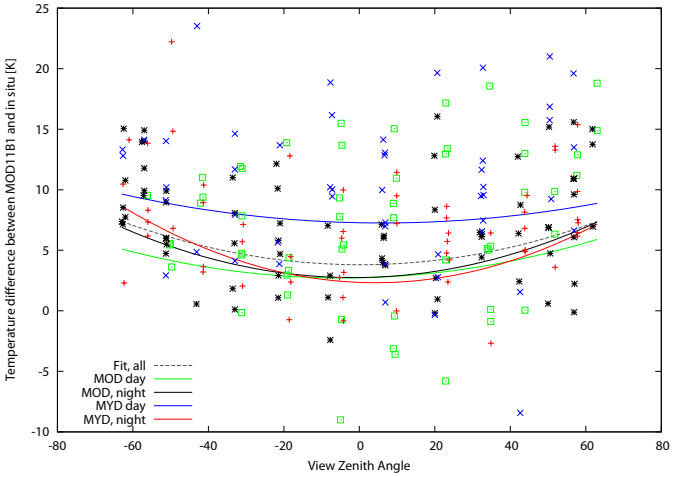

Figure 9: Temperature differences (calculated as in situ minus MOD11B1) against MODIS view zenith angle. The shown lines are fitted second order polynomials. The markers for the different overpasses are the same as for fig. 7 and 8.

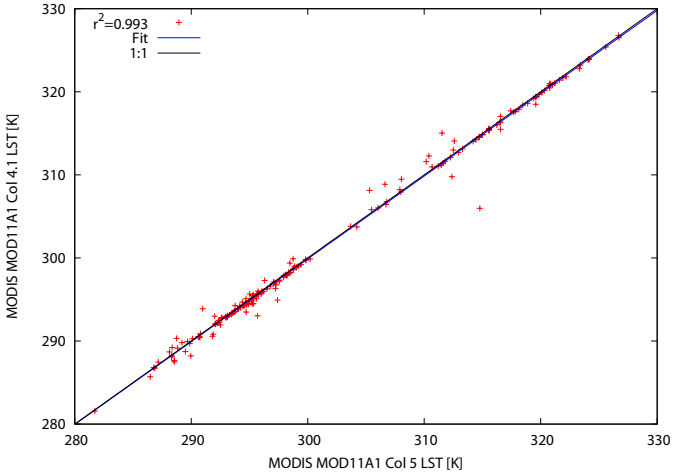

Figure 10: Comparison between MOD11A1 version 5 and version 4.1 data for the Dahra site.

one per day. The pattern is similar for the Dahra site. This difference in the data availability is likely to be the result of the refinements in the V5 algorithm, e.g. the confidence level for the cloud masking has been lowered from 99% to 95% for areas below 2000 m a.s.l., which means that more pixels are processed (Wan, 2008).

Earlier studies reported problems with the MOD11A1 version 5 product over arid and semiarid areas (Hulley and Hook, 2009). We compared the two product versions over both sites, and found no significant differences between the two product versions in terms of LST values. A scatterplot for the Dahra site is shown in fig. 10, which shows an almost perfect correlation. If one also removes cases for which less than half of the 81 pixels within the averaging window are available, the largest outliers are removed, the coefficient of determination increases to 0.998. This only leaves four cases where the LST difference between the versions exceeds two degrees and none exceeds three degrees. For neither of the two test sites the retrieved LST seem to be affected by algorithmic differences between versions 5 and 4.1. However, despite the previously reported problems, the large difference in available data for the two versions makes version 5 preferable for applications in the investigated geographic region.

4. Concluding remarks and perspectives

We tested the performance of several SEVIRI-based LST algorithms over two sites in semi-arid West Africa. The results show that none of the algorithms performs well during the monsoon-season and the retrieved LST have large biases and relatively low r^2-values. This may be due to problems with the algorithms themselves or with the estimated total column water vapour, which is a key input to the algorithms. The tested algorithms yield similar results for the two field sites, which indicates that the problems are not caused by issues arising from comparing small scale in situ measurements with medium or coarse scale satellite data. All algorithms perform much better towards the end of the monsoon season, with considerably lower biases and with r^2 values above 0.9: this indicates that the poor performance is limited to the monsoon season.

Among the different SEVIRI algorithms tested, the Munoz algorithm generally out-performed the Romaguera/Atitar algorithms. Comparing LST from the Munoz algorithm to the LSA-SAF product yielded mixed results: the Munoz LST generally had higher r^2-values and lower biases, but the LSA-SAF product had slopes closer to unity and smaller offsets.

One key finding is that the LSA-SAF product performs better with the MPEF CLMK cloud mask applied than with the SAF CLMK cloud mask. This is surprising as the SAF CLMK was specifically developed for use with LSA-SAF products. The main reason for this difference in performance is thought to be the large difference in the number of "cloud-free" pixels: on average, the MPEF CLMK mask marks approximately 30% more pixels as cloudy than the SAF CLMK mask. The better relative performance is gained at the cost of less data. Both cloud masks suffer from problems with undetected clouds within and outside the monsoon-season, which leads to large underestimations in the satellite derived LST's and weaker correlations.

The MODIS products investigated showed relative poor agreement with the in situ data, with slightly better performance of the coarser MOD11B1 product compared to the 1 km MOD11A1-product, although the latter provided more data. No significant difference was found between the V5 and V4.1 data in terms of LST-estimates; since the V5 data contain more cloud-free data, it is recommended to use V5 data.

5. Acknowledgements

The authors would like to thank the LSA-SAF-team and MODIS LST-team for providing the LST products used in this study. This work was performed partly within the framework of the AMMA project. Based on a French initiative, AMMA has been constructed by an international group and is currently funded by large number of agencies, especially from France, the UK, the US and Africa. It has been the beneficiary of a major financial contribution from the European Community's Sixth Framework Research Programme. Detailed information on the scientific coordination and funding is available on the AMMA international web site (http://www.amma-eu.org/).

References

Agam, N., Kustas, W. P., Anderson, M. C., Li, F., Neale, C. M., 2007. A vegetation index based technique for spatial sharpening of thermal imagery. Remote Sensing of Environment 107 (4), 545 – 558.

Atitar, M., Sobrino, J. A., 2009. A Split-Window Algorithm for Estimating LST from Meteosat 9 Data: Test and Comparison With *In Situ* Data and MODIS LSTs. IEEE Transactions on Geoscience and Remote Sensing Letters 6 (1), 122–126.

Batjes, N. H., 2001. Options for increasing carbon sequestration in West African soils: an exploratory study with special focus on Senegal. Land Degradation & Development 12 (2), 131–142.

Becker, F., Li, Z.-L., 1990. Towards a local split window method over land surfaces. International Journal of Remote Sensing 11, 369 – 393.

Carlson, T. N., Ripley, D. A., 1997. On the relation between NDVI, fractional vegetation cover, and leaf area index. Remote Sensing of Environment 62 (3), 241 – 252.

Choudhury, B. J., Dorman, T. J., Hsu, A. Y., 1995. Modeled and Observed Relations between the AVHRR Split Window Temperature Difference and Atmospheric Precipitable Water over Land Surfaces. Remote Sensing of Environment 51, 281–290.

Coudert, B., Ottle, C., Boudevillain, B., Demarty, J., Guillevic, P., 2006. Contribution of Thermal Infrared Remote Sensing Data in Multiobjective Calibration of a Dual-Source SVAT Model. Journal of Hydrometeorology 7 (3), 404–420.

Coudert, B., Ottle, C., Briottet, X., 2008. Monitoring land surface processes with thermal infrared data: Calibration of SVAT parameters based on the optimisation of diurnal surface temperature cycling features. Remote Sensing of Environment 112 (3), 872 – 887.

Dash, P., Göttsche, F.-M., Olesen, F.-S., Fischer, H., 2002. Land surface temperature and emissivity estimation from passive sensor data: theory and practice-current trends. International Journal of Remote Sensing 23, 2563–2594.

Derrien, M., Gleau, H. L., 2005. MSG/SEVIRI cloud mask and type from SAFNWC. International Journal of Remote Sensing 26 (21), 4707–4732.

Eumetsat, 2007. EUM/OPS/TEN/07/0313. Typical Geometrical Accuracy for MSG-1/2. Tech. rep., Eumetsat.

EUMETSAT, Trigo, I., Freitas, S., Bioucas-Dias, J., Barroso, C., Monteiro, I., Viterbo, P., 2009. Algorithm Theoretical Basis Document for Land Surface Temperature (LST) (SAF/LAND/IM/ATBD_LST/1.0). Tech. rep., Eumetsat.

Fensholt, R., Sandholt, I., 2005. Evaluation of MODIS and NOAA AVHRR vegetation indices with in situ measurements in a semi-arid environment. International Journal of Remote Sensing 26 (12), 2561–2594.

Freitas, S. C., Trigo, I. F., Bioucas-Dias, J. M., Göttsche, F.-M., 2010. Quantifying the Uncertainty of Land Surface Temperature Retrievals From SEVIRI/Meteosat. IEEE Transactions on Geoscience and Remote Sensing 48 (1), 523–534.

Hiernaux, P., Diarra, L., Trichon, V., Mougin, E., Soumaguel, N., Baup, F., 2009. Woody plant population dynamics in response to climate changes from 1984 to 2006 in Sahel (Gourma, Mali). Journal of Hydrology 375 (1-2), 103 – 113, surface processes and water cycle in West Africa, studied from the AMMA-CATCH observing system.

Hulley, G. C., Hook, S. J., 2009. Intercomparison of versions 4, 4.1 and 5 of the MODIS Land Surface Temperature and Emissivity products and validation with laboratory measurements of sand samples from the Namib desert, Namibia. Remote Sensing of Environment 113 (6), 1313 – 1318.

Jiang, G.-M., Li, Z., 2008. Split-window algorithm for land surface temperature estimation from MSG1-SEVIRI data. International Journal of Remote Sensing 29, 6067–6074.

Jiménez-Muñoz, J.-C., Sobrino, J. A., 2008. Split-Window Coefficients for Land Surface Temperature Retrieval From Low-Resolution Thermal Infrared Sensors. IEEE Geoscience and Remote Sensing Letters 5, 806–809.

Kondratyev, K. Y., 1969. Radiation in the atmosphere. Academic Press, New York.

Madeira, C., 2002. Generalized split-window algorithm for retrieving land surface temperature from MSG/SEVIRI data. In: Proceedings of Land Surface Analysis SAF Training Workshop, Lisbon, 810 July. Eumetsat, p. 42 47.

Mougin, E., Hiernaux, P., Kergoat, L., Grippa, M., de Rosnay, P., Timouk, F., Dantec, V. L., Demarez, V., Lavenu, F., Arjounin, M., Lebel, T., Soumaguel, N., Ceschia, E., Mougenot, B., Baup, F., Frappart, F., Frison, P., Gardelle, J., Gruhier, C., Jarlan, L., Mangiarotti, S., Sanou, B., Tracol, Y., Guichard, F., Trichon, V., Diarra, L., Soumar, A., Koit, M., Dembl, F., Lloyd, C., Hanan, N., Damesin, C., Delon, C., Sera, D., Galy-Lacaux, C., Seghieri, J., Becerra, S., Dia, H., Gangneron, F., Mazzega, P., 2009. The AMMA-CATCH Gourma observatory site in Mali: Relating climatic variations to changes in vegetation, surface hydrology, fluxes and natural resources. Journal of Hydrology 375 (1-2), 14 – 33.

Nishida, K., Nemani, R. R., Running, S. W., Glassy, J. M., 2003. An operational remote sensing algorithm of land surface evaporation. Journal of Geophysical Research 108 (D9).

Norman, J. M., Divakarla, M., Goel, N. S., 1995. Algorithms for Extracting Information from Remote Thermal-IR Observations of the Earth's Surface. Remote Sensing of Environment 51, 157–168.

Ogunjobi, K., He, Z., Simmer, C., 2008. Spectral aerosol optical properties from aeronet sun-photometric measurements over west africa. Atmospheric Research 88 (2), 89 – 107.

Peres, L. F., DaCamara, C. C., 2005. Emissivity Maps to Retrieve Land-Surface Temperature From MSG/SEVIRI. IEEE Transactions on Geoscience and Remote Sensing 43 (8), 1834–1844.

Pinheiro, A. C., Privette, J. L., Guillevic, P., 2006. Modeling the observed angular anisotropy of land surface temperature in a Savanna. IEEE Transactions on Geoscience and Remote Sensing 44 (4), 1036–1047.

Pinheiro, A. C., Privette, J. L., Mahoney, R., Tucker, C. J., 2004. Directional effects in a daily AVHRR land surface temperature dataset over Africa. IEEE Transactions on Geoscience and Remote Sensing 42 (9), 1941–1954.

Price, J. C., 1984. Land Surface Temperature Measurements From the Split Window Channels of the NOAA 7 Advanced Very High Resolution Radiometer. Journal of Geophysical Research 89, 7231–7237.

Rasmussen, M. O., Göttsche, F.-M., Diop, D., Mbow, C., Olesen, F.-S., Fensholt, R., Sandholt, I., 2010a. Tree survey and allometric models for tiger bush in northern Senegal and comparison with tree parameters derived from high resolution satellite data (Submitted). International Journal of Applied Earth Observation and Geoinformation.

Rasmussen, M. O., Göttsche, F.-M., Olesen, F.-S., Sandholt, I., 2010b. Directional Effects on Land Surface Temperature Estimation from Meteosat Second Generation for Savanna Landscapes (Submitted). IEEE Transactions on Geoscience and Remote Sensing.

Rasmussen, M. O., Pinheiro, A. C., Proud, S. R., Sandholt, I., 2010c.

Modeling Angular Dependences in Land Surface Temperatures From the SEVIRI Instrument Onboard the Geostationary Meteosat Second Generation Satellites. IEEE Transactions on Geoscience and Remote Sensing 48, 3123–3133.

Sandholt, I., Rasmussen, K., Andersen, J., 2002. A simple interpretation of the surface temperature/vegetation index space for assessment of surface moisture status. Remote Sensing of Environment 79 (2-3), 213 – 224.

Schädlich, S., Göttsche, F.-M., Olesen, F.-S., 2001. Influence of land surface parameters and atmosphere on meteosat brightness temperatures and generation of land surface temperature maps by temporally and spatially interpolating atmospheric correction. Remote Sensing of Environment 75 (1), 39 – 46.

Schmetz, J., Pili, P., Tjemkes, S., Just, D., Kerkmann, J., Rota, S., Ratier, A., 2002. An Introduction to Meteosat Second Generation (MSG). Bulletin of the American Meteorological Society 83, 977–992.

Schroedter-Homscheidt, M., Drews, A., Heise, S., 2008. Total water vapor column retrieval from MSG-SEVIRI split window measurements exploiting the daily cycle of land surface temperatures. Remote Sensing of Environment 112 (1), 249 – 258.

Smith, J. A., Chauhan, N. S., Schmugge, T. J., Jr., J. R. B., 1997. Remote Sensing of Land Surface Temperature: The Directional Viewing Effect. IEEE Transactions on Geoscience and Remote Sensing 35, 4.

Sobrino, J. A., Jimenez-Munoz, J. C., Soria, G., Romaguera, M., Guanter, L., Moreno, J., Plaza, A., Martinez, P., 2008. Land Surface Emissivity Retrieval From Different VNIR and TIR Sensors. IEEE Transactions on Geoscience and Remote Sensing 46, 316–327.

Sobrino, J. A., Romaguera, M., 2004. Land surface temperature retrieval from MSG1-SEVIRI data. Remote Sensing of Environment 92, 247–254.

Sobrino, J. A., Romaguera, M., 2008. Water-vapour retrieval from Meteosat 8/SEVIRI observations. International Journal of Remote Sensing 29, 741–754.

Stisen, S., Jensen, K. H., Sandholt, I., Grimes, D. I., 2008a. A remote sensing driven distributed hydrological model of the senegal river basin. Journal of Hydrology 354 (1-4), 131 – 148.

Stisen, S., Sandholt, I., Noergaard, A., Fensholt, R., Eklundh, L., 2007. Estimation of diurnal air temperature using MSG SEVIRI data in West Africa. Remote Sensing of Environment 110 (2), 262 – 274.

Stisen, S., Sandholt, I., Noergaard, A., Fensholt, R., Jensen, K. H., 2008b. Combining the triangle method with thermal inertia to estimate regional evapotranspiration – Applied to MSG-SEVIRI data in the Senegal River basin. Remote Sensing of Environment 112 (3), 1242 – 1255.

Sun, D., Pinker, R. T., 2007. Retrieval of surface temperature from the msg-seviri observations: Part i. methodology. International Journal of Remote Sensing 28, 5255–5272.

Trigo, I., Madeira, C., Monteiro, I., Coelho, S., Barroso, C., Olesen, F.-S., Göttsche, F.-M., Peres, L., 2008a. Product User Manual, Land Surface Temperature. Tech. rep., EumetSat Land SAF, version 2.2.

Trigo, I., Peres, L., DaCamara, C., Freitas, S., Feb. 2008b. Thermal Land Surface Emissivity Retrieved From SEVIRI/Meteosat. Geoscience and Remote Sensing, IEEE Transactions on 46 (2), 307–315.

Trigo, I. F., Monteiro, I. T., Olesen, F., Kabsch, E., 2008c. An assessment of remotely sensed land surface temperature. Journal of Geophysical Research 113, 1–12.

Tucker, C. J., 1979. Red and photographic infrared linear combinations for monitoring vegetation. Remote Sensing of Environment 8 (2), 127 – 150.

Verstraeten, W. W., Veroustraete, F., van der Sande, C. J., Grootaers, I., Feyen, J., 2006. Soil moisture retrieval using thermal inertia, determined with visible and thermal spaceborne data, validated for european forests. Remote Sensing of Environment 101 (3), 299 – 314.

Wan, Z., 2008. New refinements and validation of the MODIS Land-Surface Temperature/Emissivity products. Remote Sensing of Environment 112 (1), 59 – 74.

Wan, Z., Dozier, J., 1996. A generalized split-window algorithm for retrieving land-surface temperature from space. IEEE Transactions on Geoscience and Remote Sensing 34, 892–905.

Wan, Z., Li, Z.-L., 1997. A physics-based algorithm for retrieving land-surface emissivity and temperature from EOS/MODIS data. IEEE Transactions on Geoscience and Remote Sensing 35 (4), 960–996.

Yu, Y., Privette, J., Pinheiro, A., 2008. Evaluation of Split-Window Land Surface Temperature Algorithms for Generating Climate Data Records. IEEE Transactions on Geoscience and Remote Sensing 46, 179–192.